

Advanced Digital Control of Resonant MEMS Mirrors for AR Displays

DIPLOMARBEIT

Ausgeführt zum Zwecke der Erlangung des akademischen Grades eines
Diplom-Ingenieurs (Dipl.-Ing.)

unter der Leitung von
Univ.-Prof. Dr.sc.techn. Georg Schitter
Dr. Han Woong Yoo

eingereicht an der
Technischen Universität Wien
Fakultät für Elektrotechnik und Informationstechnik
Institut für Automatisierungs- und Regelungstechnik

von
Fabian Reier
Matrikelnummer: 11929816
Schäffergasse 2/507
1040 Wien, Österreich

Wien, im Jänner 2024

Acknowledgement

This thesis marks the end of my master studies in Embedded Systems at the Technical University of Vienna. As I reflect on my academic journey, I would like to express my sincere gratitude to those who have been instrumental in my success throughout the course of this work and in my education.

First, I would like to thank Univ.-Prof. Dipl.-Ing. Dr.sc.techn. Georg Schitter, head of the Advanced Mechatronic Systems (AMS) group at the Automation and Control Institute (ACIN). His support and the opportunity to contribute to the institute played a pivotal role in shaping my academic experience. I am grateful for his guidance, insightful critiques, and encouragement, all of which were important for the successful completion of this work.

Furthermore, I would like to express my gratitude to my supervisor Dr. Han Woong Yoo for his unwavering support and boundless patience and constructive criticism during the preparation of this thesis. His mentorship, along with valuable suggestions and the fact that he was always available for questions, significantly contributed to my progress. He was always available for questions, which played a pivotal role in the successful completion of this work. I am particularly grateful for his provision of essential equipment and the establishment of experimental setups, which were indispensable to the success of this project.

A special acknowledgment is extended to Dr. David Brunner for engaging discussions and support throughout the research process. His insights have been invaluable in shaping the trajectory of this work.

In conclusion, I want to express my appreciation to my friends and family for their encouragement and support over the past years. I am truly thankful for the educational opportunity provided by my parents to attend university and for their financial assistance. Thank you

Abstract

Augmented reality (AR) represents a transformative technology that promises the dynamic intersection of the physical and virtual world and reshapes the way we perceive and interact with our environment. Use cases range from entertainment and education to industrial and automotive applications. One of the most promising devices that enable this innovation are micro electromechanical mirrors (MEMS mirrors). These tiny, yet highly precise mirrors enable a wide range of applications that require precise control of light beams, such as light detection and ranging (LIDAR) systems and AR devices.

In this thesis, MEMS mirror controllers are investigated regarding their performance to suppress the influence of external vibration, following an extended automotive standard. Initially, a 1D resonant MEMS mirror is identified through measurements, and three distinct phase locked loop (PLL) controllers are developed. The designed LQG controller and the H_∞ controller both reach a optical pointing uncertainty of 11 millidegree, which is an improvement by a factor of 2 compared to a simple PI controller.

Additionally, controllers for the synchronization of two individual MEMS mirrors are developed. The direct correction PLL (DCPLL) is proposed as an alternative to the conventional synchronization controller implemented on top of the PLL, resolving the competition between the synchronization controller and PLL. The DCPLL not only allows for a much simpler controller design but also reduces the synchronization error under vibration influence, thereby improving the uniformity of the Lissajous pattern. The PID-based DCPLL reduces the synchronization error by 29 %. By using model-based design approaches such as LQG and H_∞ the synchronization error is reduced by 42 % and 35 %, respectively.

Finally, the developed synchronization techniques are also tested on a 2D MEMS mirror. The 2D MEMS mirror contains additional challenges due to the coupling and crosstalk between its two axes. With these challenges addressed, the synchronization controllers are applied to the 2D MEMS mirror. The PID-based DCPLL reduces the synchronization error by 31 %, and the LQG-based DCPLL achieves a reduction by 46 %.

This thesis demonstrates that innovative synchronization structures and model-based design approaches can improve the robustness against external vibrations. This allows the utilization of MEMS mirrors under harsh environmental conditions, enabling reliable MEMS-based optical scanning for both LIDAR applications and AR devices.

Zusammenfassung

Erweiterte Realität (AR) repräsentiert eine Technologie an der Schnittstelle zwischen der physischen und virtuellen Welt, die die Art und Weise, wie wir unsere Umgebung wahrnehmen und damit interagieren, neu gestaltet. Die Anwendungsfälle reichen von Unterhaltung und Bildung bis hin zu industriellen und automobilen Anwendungen. Eines der vielversprechendsten Geräte, die diese Innovation ermöglichen, sind mikroelektro-mechanische Spiegel. Diese winzigen, hochpräzisen MEMS-Spiegel ermöglichen eine Vielzahl von Anwendungen, die eine präzise Steuerung von Lichtstrahlen erfordern, wie zum Beispiel LIDAR-Systeme und AR-Geräte.

In dieser Arbeit werden MEMS-Spiegelregler in Bezug auf ihre Fähigkeit zur Unterdrückung von externen Vibrationseinflüssen auf Projektionssysteme untersucht. Angefangen mit der Identifikation eines resonanten 1D MEMS-Spiegels werden drei verschiedene Phasenregelschleifen entworfen. Ein modellbasierter LQG-Entwurf und ein H_∞ -basierter Regler erreichen beide eine Auflösung von 12 Milligrad in einer Vibrationsumgebung entsprechend einer Erweiterung eines Automobilstandards, was einer Verbesserung um 50 % gegenüber einem einfachen PI Reglers entspricht.

Anschließend werden Regler zur Synchronisation von zwei individuellen MEMS-Spiegeln entwickelt. Die Direct Correction PLL (DCPLL) wird als Alternative zur herkömmlichen Reglerstruktur vorgeschlagen, die den gegenseitigen Einfluss beider Regler entfernt. Das erlaubt nicht nur einen einfachere Reglerentwurf, sondern verbessert auch die Gleichförmigkeit der Lissajous-Figuren. Eine PID-basierte Version reduziert den Synchronisationsfehler um 29 % und modellbasierte Methoden, wie LQG oder H_∞ Regelungen, erreichen eine Verbesserung um 42 % bzw. 35 %.

Schließlich werden die entwickelten Synchronisationstechniken auch auf einen 2D-MEMS-Spiegel getestet. Der 2D-MEMS-Spiegel birgt zusätzliche Herausforderungen aufgrund der Kopplung und des Übersprechens zwischen den beiden Achsen des MEMS-Spiegels. Nach deren Lösen werden die Synchronisationscontroller auch auf den 2D-MEMS-Spiegel angewendet. Die PID-basierte Version reduziert den Synchronisationsfehler um 31 % und eine LQG-basierte DCPLL erreicht eine Verbesserung um 46 %.

Diese Arbeit zeigt, dass innovative Synchronisationsstrukturen und modellbasierte Entwurfsansätze die Robustheit gegenüber externen Vibrationen verbessern können, was ein zuverlässiges optisches Scannen für LIDAR-Anwendungen und AR-Geräte ermöglicht.

Contents

Acronyms	x
Symbols	xi
1 Introduction	1
1.1 Laser Beam Scanning (LBS)	2
1.2 MEMS Mirrors	3
1.3 Goal of the Thesis	5
2 State of the Art	7
2.1 Driving of Comb Drive Actuated MEMS Mirrors	7
2.2 Self-Sensing of Resonant MEMS Mirrors	7
2.3 MEMS Mirror Modeling and Dynamic Behavior	9
2.4 Closed-Loop Control of Resonant MEMS Mirrors	10
2.4.1 Single Axis Control by Phase Locked Loops	10
2.4.2 Synchronization of Multiple Mirrors	11
2.5 Scope of the Thesis	13
3 Single Axis MEMS Mirror Control	15
3.1 Identification of the Local Dynamics	15
3.2 Controller Design	21
3.2.1 PI Control	21
3.2.2 LQG Control	21
3.2.3 H_{∞} Control	25
3.3 Implementation	27
3.3.1 DCO and Scheduler	28
3.3.2 Digital Controller	29
3.3.3 Phase Detector	30
3.4 Evaluation	31
3.5 Summary	34

4	Synchronization of two 1D MEMS Mirrors	35
4.1	Synchronization control for PLL-operated MEMS mirrors	41
4.1.1	Model Extension	41
4.1.2	PID-based Synchronization Controller Design	43
4.1.3	Analysis of Synchronization Controller	45
4.2	Direct Correction PLL	46
4.2.1	General Idea	46
4.2.2	Controller Design	47
4.3	Extension of the Implementation	50
4.3.1	Configurable MIMO Controller	50
4.3.2	Reference Frequency Generator	53
4.4	Experimental Evaluation	54
4.5	Summary	58
5	Synchronization of a 2D Mirror	59
5.1	Dynamic Behavior	59
5.2	Local Dynamic Behavior and Modeling	59
5.3	Vibration Influence	63
5.4	Mechanical Coupling	64
5.4.1	Mechanical Coupling Effects on the Global Dynamics	64
5.4.2	Mechanical Coupling Effects on the Local Dynamics	66
5.5	Electrical Crosstalk	69
5.6	Controller Design for the Outer Axis	69
5.6.1	PLL and Conventional Synchronization Controller Design	69
5.6.2	PID-based DCPLL	71
5.6.3	LQG-based DCPLL	73
5.6.4	Evaluation	73
5.7	Controller Design for the Inner Axis	76
5.7.1	PLL Design	78
5.7.2	DCPLL for Amplitude Control	78
5.7.3	Conventional Amplitude Control Design	79
5.7.4	Evaluation	80
5.8	Summary	82
6	Conclusion	83
6.1	Outlook	85
	Appendix A	92

List of Figures

1.1	Applications of AR	2
1.2	Scanner principles	2
1.3	MEMS mirrors used for 2D projection	3
1.4	Lissajous pattern	4
1.5	MEMS mirror driving principles	5
2.1	Square wave driving of the MEMS mirror	8
2.2	MEMS mirror comb drive	8
2.3	Global and local dynamics	9
2.4	Phase Locked Loop for MEMS mirror driving	10
2.5	Closed-loop driving of the MEMS mirror	12
2.6	Synchronization structure proposed by Stelzer et.al.	13
3.1	MEMS mirror response curve	16
3.2	Identification of local dynamics	17
3.3	Illustration for the relation between the identified transfer functions	19
3.4	Block diagram of the PLL for MEMS mirror control	21
3.5	Single axis PI controller frequency response	22
3.6	Single axis LQG controller frequency response	25
3.7	General and MEMS mirror-specific H_∞ framework	26
3.8	Single axis H_∞ weighting functions	27
3.9	Frequency response for H_∞ controller design	27
3.10	Schematic of the DCO	29
3.11	Block diagrams of the transfer function implementations	29
3.12	Comparison of the frequency responses of the controllers	31
3.13	Vibration profile for single axis vibration	32
3.14	Setup of the pointing stability experiment	32
3.15	Sum of video to evaluate pointing error	33
3.16	Distribution of the laser pointing error under vibration influence	34
4.1	Experimental setup for a projection system	36
4.2	Photograph of the experimental setup	36

List of Figures

4.3	Block diagram of master-slave synchronization	37
4.4	Driving and sensing definitions for the slave axis	38
4.5	Impact of the synchronization error on the Lissajous pattern	39
4.6	Impact of the phase error on the Lissajous pattern	40
4.7	Slave axis MEMS mirror controller	42
4.8	Model extension for synchronization	42
4.9	Closed-loop transfer function for synchronization and phase error	43
4.10	Synchronization controller closed-loop verification by emulated disturbance	44
4.11	Load disturbance sensitivity for different gains	45
4.12	Disturbance measurements for different gains	46
4.13	Direct Correction PLL	47
4.14	DCPLL PID controller design frequency responses	47
4.15	DCPLL LQG Controller Design frequency responses	48
4.16	Block diagram of the DCPLL in H_∞ framework	49
4.17	DCPLL H_∞ controller design	50
4.18	Schematic of the configurable controller and MEMS mirror	51
4.19	Configurable MIMO Controller	52
4.20	Reference frequency generator	53
4.21	Synchronization controlllers comparison by frequency response	55
4.22	Synchronization controller performance evaluation	56
4.23	Lissajous pattern evaluation by sum of video frames	57
4.24	Brighness distribution of the video sum images	58
5.1	Response curve of the 2D MEMS mirror	60
5.2	Local dynamics of the 2D MEMS mirror	61
5.3	Relation between comb drive and capacitance	62
5.4	Tuning of the transfer function P_s	62
5.5	Influence of external vibration on the 2D MEMS mirror	63
5.6	Vibration profile used to evaluate the controller for the 2D MEMS mirror	64
5.7	Response curve of the outer axis of the 2D MEMS mirror	65
5.8	Response curve of the inner axis of the 2D MEMS mirror	65
5.9	Coupling influence on the local dynamics	67
5.10	Identification of the local cross coupling dynamics	68
5.11	Invalid measurement regions during MEMS mirror period	70
5.12	Invalid measurements regions in a Lissajous frame	70
5.13	Experimental evaluation of invalid zero-crossings	71
5.14	PLL design for the outer axis of the 2D MEMS mirror	71
5.15	PID-based synchronization controller design for the outer axis	72
5.16	DCPLL design for 2D MEMS mirror	72
5.17	DCPLL LQR design for 2D MEMS mirror	73
5.18	Experimental setup for evaluation of the 2D MEMS mirror controller . .	74
5.19	Photograph of the lab setup for the 2D MEMS mirror	74
5.20	Evaluation results of the controllers for 2D MEMS mirror	75
5.21	Lissajous pattern evaluation by sum of video frames for 2D MEMS mirror	76
5.22	Evaluation results of the controllers by intensity along line	77
5.23	PLL design for the inner axis of the 2D MEMS mirror	77

List of Figures

5.24	DCPLL design for 2D MEMS mirror	78
5.25	Sensing signals for the inner axis	79
5.26	Amplitude control for the inner axis	79
5.27	Boxplots for the amplitude control evaluation	80
5.28	Amplitude control evaluation by sum of video frames	81
5.29	Evaluation results of the amplitude controllers by intensity along line .	81

List of Tables

3.1	DCO counting process example	28
4.1	Example for the reference generation unit counting process, generating a ratio of $\frac{27}{10}$ by full period counting and interpolation.	54
4.2	Standard deviation of different controllers with or without external vibration	56
5.1	Standard deviation of different controllers with or without external vibration	75
5.2	Standard deviation of the amplitude error Δta of different controllers .	80

Acronyms

ACIN	Automation and Control Institute
ADPLL	all digital PLL
AMS	Advanced Mechatronic Systems Group
AR	augmented reality
DCO	digitally controlled oscillator
DCPLL	direct correction phase locked loop
FPGA	field programmable gate array
LBS	laser beam scanning
LIDAR	light detection and ranging
LQG	linear quadratic Gaussian
LQR	linear quadratic regulator
MEMS	micro electromechanical system
MIMO	multiple input multiple output
MIMO	single input single output
PI	proportional-integral
PID	proportional-integral-derivative
PLL	phase locked loop
RMS	root mean square

Symbols

Δt	phase error of the PLL
Δtr	synchronization error of the two axes
Δta	amplitude error of the MEMS mirror
\hat{T}	driving period of the DCO
\hat{s}_{off}	switch-off timing of the scheduler
\hat{s}_{on}	switch-on timing of the scheduler
T_{lin}	driving period of the DCO, operating point
$s_{\text{off,lin}}$	switch-off timing of the scheduler, operating point
$s_{\text{on,lin}}$	switch-on timing of the scheduler, operating point
T	driving period of the DCO, deviation from the operating point
s_{off}	switch-off timing of the scheduler, deviation from the operating point
s_{on}	switch-on timing of the scheduler, deviation from the operating point
P_{son}	transfer function of P from s_{on} to Δt
P_{soff}	transfer function of P from s_{off} to Δt
P_s	transfer function $P_{\text{son}} + P_{\text{soff}}$
A_P, B_P, C_P	matrices of the system P , the single axis MEMS mirror
A_G, B_G, C_G	matrices of the extended system G
P_T	transfer function of P from T to Δt
Q	state weighting matrix for LQR design
R	controller output weighting matrix for LQR design
Q_n	covariance matrix of the state for Kalman filter
R_n	covariance matrix of the measurement noise for Kalman filter
K	gain of the state feedback controller
M_x	innovation gain of the Kalman estimator
T_{ref}	reference period generated by the master axis
T_m	actual MEMS mirror period
$b_{T1}, b_{T0}, b_{S1}, b_{S0}$	numerator coefficients of P_T and P_s
$a_{T1}, a_{T0}, a_{S1}, a_{S0}$	denominator coefficients of P_T and P_s
d	disturbance caused by vibrations
n	sensor noise
$\frac{M}{N}$	Lissajous ratio, $M, N \in \mathbb{N}$

CHAPTER 1

Introduction

Augmented reality (AR) technology has rapidly gained popularity in recent years, spanning various industries and applications, from entertainment to education, health-care, automotive, and beyond. AR is a cutting-edge technology that superimposes digital information, such as images, videos, 3D models, or text, onto the real world, enhancing our perception and interaction with the environment. It has the potential to revolutionize how we engage with information and interact with the world around us. Figure 1.1 depicts example use cases of AR. Head-up displays have been extensively used in airplanes [2] to project important information directly into the field of view of the pilot, letting them focus on the environment while still showing important data. In recent years, head-up displays have shown a growing appearance in cars. Furthermore, AR Glasses represent a promising innovation in the world of wearable technology. They blend the physical surroundings with digital information, offering great potential for increased entertainment but also promising to increase productivity and performance in various professional fields.

MEMS Mirrors are one of the most promising technologies for the realization of AR devices, especially because of their small form factor and their outstanding contrast compared to other technologies such as digital micromirror devices [3], switchable polarized modulation layers [4] or types of LED displays [5].

Additionally, MEMS mirrors have been investigated extensively as a beam steering device for automotive LIDAR. In contrast to other beam steering techniques such as spinning scanners, polygon mirrors, or optical phase arrays, MEMS mirrors promise a smaller form factor due to the decreased complexity of the required mechanical setup and lower production cost. The main challenge for MEMS mirrors is the high frequency of the system, caused by the required resolution and framerate. Furthermore, to operate the system in harsh environmental conditions as they occur in automotive or industrial environments, the robustness to external vibrations and shocks, as well as temperature changes is important. Last but not least for extensive commercial use a low unit price is indispensable.

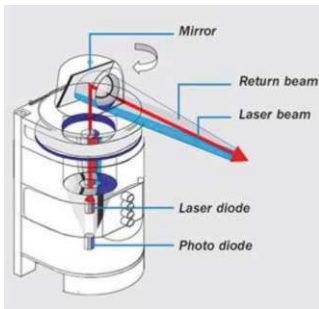


(a)

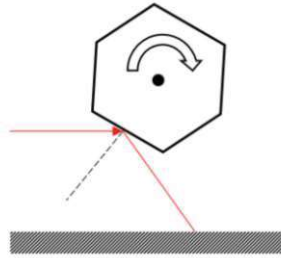


(b)

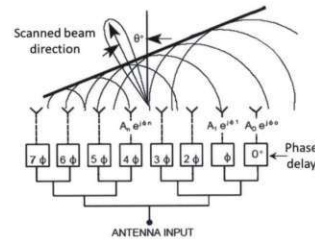
Figure 1.1: Augmented Reality applications [1] (a) Automotive Head-Up Display (b) AR glasses [1]



(a)



(b)



(c)

Figure 1.2: Three different scanner principles: (a) rotating scanner [6], (b) polygon mirror based scanning [7], (c) optical phased array [6, 8].

1.1 Laser Beam Scanning (LBS)

Laser beam scanning systems use moveable mirrors to steer the laser beam. The applications of laser beam scanning can be categorized into LSB displays and LIDAR applications. LBS displays create images by steering multicolor lasers with moving mirrors and modulating the laser intensity, creating an image due to the persistence of vision. LBS-based projection systems are not only used for displays but also for manufacturing applications such as laser printers and laser engraving. LIDAR applications include a feedback path to the LBS-based projection system. By using a pulsed laser source and measuring the time of flight of the light beam a 2D or 3D scanning becomes possible.

The requirements for LBS systems are versatile. Therefore, there exist multiple common approaches for LBS systems. Spinning scanners consist of a receiver and a transmitter attached to a rotating frame, which allows a 360° field of view at a single vertical height. They are commonly used for automotive LIDAR. Figure 1.2 (a) shows a spinning scanner with a transmitter and a receiver mounted to the static frame [6]. Polygon Mirror-based scanners also use a continuous rotational motion similar to spinning scanners. However, due to the polygon mirror, the field of view is not 360° , but smaller. Therefore, they are not only suitable for scanning applications but also for projection applications such

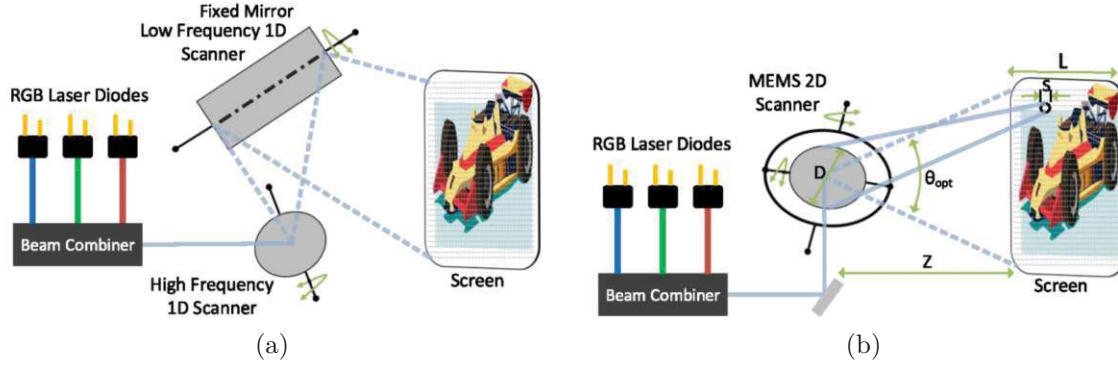


Figure 1.3: Schematic of a 2D projection setup consisting of (a) 2 individual 1D mirrors and (b) a single 2D mirror

as 2D or 3D printing or laser manufacturing [7]. Figure 1.2 (b) shows the basic principle of polygon mirror scanning. Optical phased arrays have received much attention in recent development because of their major advantage of not containing any moving parts. Figure 1.2 (c) shows a schematic of a phased array. The light beam is split into multiple emitting paths and precise delay shifters on each path, allowing a beam steering of the emitted path [9, 6, 10].

1.2 MEMS Mirrors

MEMS is a promising technology incorporating both electronic and mechanical parts. The fabrication of MEMS uses technologies very similar to the semiconductor industry. Therefore, The base material for MEMS is silicon, offering not only astonishing electronic properties but also excellent mechanical properties [11]. It is harder than most metals, surprisingly highly resistant to mechanical stress, and even more resistant to tension and compression than steel [12].

The MEMS technology allows to manufacture small-scale mirrors. The key component of these MEMS mirrors is a tiny reflective surface that can be moved or tilted using micro-scale mechanical structures. MEMS mirrors find application in scanning and projection systems. 1D MEMS mirrors have a single oscillating axis, which can be used for two-dimensional scans. To project a 2D image two separate 1D MEMS mirrors are required, as illustrated in Figure 1.3 (a) [13, 14] or a single 2D MEMS mirror with two resonant axes can be used [15, 16], as shown in Figure 1.3 (b). MEMS mirrors are divided into quasistatic MEMS mirrors and resonant MEMS mirrors. As LBS projection systems require high refresh rates, high MEMS mirror oscillation frequencies are required, which means that the use of resonant MEMS mirrors is beneficial. Both MEMS mirrors of the system operate at their resonance and therefore follow a close-to-sinusoidal trajectory. The x and y position of the laser spot is given by

$$\begin{aligned} x(t) &= \sin(2\pi f_x t) \\ y(t) &= \sin(2\pi f_y t), \end{aligned} \tag{1.1}$$

1 Introduction

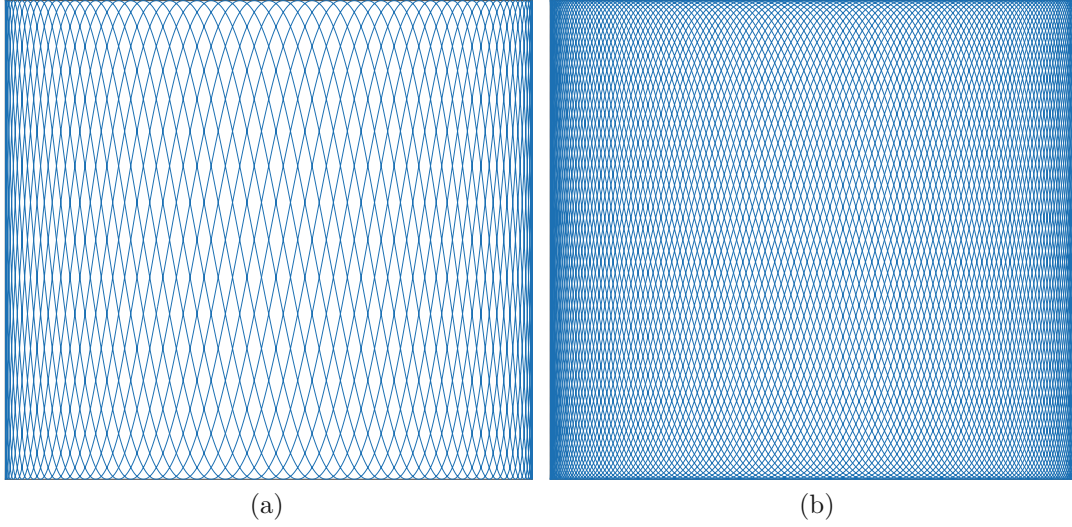


Figure 1.4: Lissajous pattern with a ratio of (a) $\frac{57}{10}$ and (b) $\frac{137}{24}$.

where f_x and f_y are the oscillating frequencies of the x and y MEMS mirror. Without loss of generality $f_y > f_x$ can be assumed and the ratio between the two frequencies is given by

$$\frac{M}{N} = \frac{f_y}{f_x}, \quad (1.2)$$

where M and N are coprime numbers. M and N define the Lissajous pattern. Figure 1.4 (a) shows a Lissajous pattern with $\frac{M}{N} = \frac{57}{10}$. In Figure 1.4 the density of the lines is increased by selecting a ratio of $\frac{137}{24}$. Since the frequencies of the MEMS mirrors are nearly constant at their mechanical resonance, but the path that the laser covers in Figure 1.4 (b) is much longer, the period of the Lissajous pattern with ratio $\frac{137}{24}$ is higher. The Lissajous period $T_{\text{Lissajous}}$ can be calculated with

$$T_{\text{Lissajous}} = \frac{N}{f_x} = \frac{M}{f_y} \quad (1.3)$$

and the framerate is given by

$$\text{fps} = \frac{1}{T_{\text{Lissajous}}} = \frac{f_x}{N} = \frac{f_y}{M}. \quad (1.4)$$

Thus, increasing the resolution of the Lissajous pattern reduces the framerate, or requires MEMS mirrors with higher oscillation frequencies.

There are three main actuation principles for MEMS mirrors: electromagnetic, electrostatic and piezoelectric actuation. Electromagnetic actuation uses the Lorentz force generated by current-carrying coils to move the MEMS mirror and achieves a high linearity over a large displacement [17, 18]. Figure 1.5 (a) illustrates the scheme. Electrostatic actuation comprises the majority of published literature. The working principle relies on the attraction of two oppositely charged plates. Since the force between two plates is very small, multiple plates are used and form so-called comb drives to agitate the

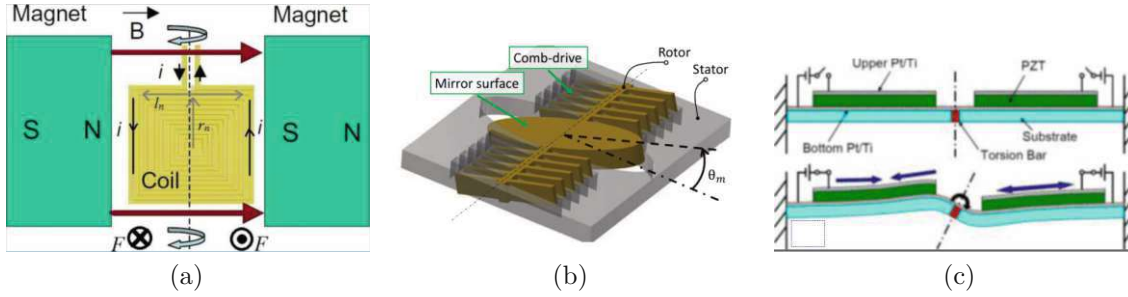


Figure 1.5: Three different MEMS mirror driving principles [6]: (a) electromagnetic actuation [17, 18], (b) electrostatic actuation by comb drives [19], (c) piezoelectric actuation [20].

MEMS mirror [17, 21, 19] as shown in Figure 1.5 (b). Piezoelectric actuation is based on the mechanical stress originating from the expansion of lead-zirconium-titanium oxide films in the x-direction when a voltage is applied in the z-direction. Figure 1.5 (c) shows how these films can be used to create a torque on the torsion bar of the MEMS mirror [17, 20].

The various environmental conditions require a closed-loop control of the MEMS mirror. Therefore, the position of the MEMS mirror needs to be measured. Three different sensing principles can be categorized: piezoresistive sensing, optical sensing and capacitive sensing. Piezoresistive Sensing measures the voltage changes induced by mechanical stress on the structure. It provides a continuous analog angle feedback of the MEMS mirror [22, 23]. Optical Sensing uses additional lasers and photodetectors to detect the position of the MEMS mirror. Both continuous angle feedback as well as discrete pulses at certain angles can be realized. However, such sensing requires additional photodetectors and lasers and thus increases the size of the system. Capacitive sensing uses the variation of the comb drive capacitance to detect the MEMS mirror position. Capacitive sensing methods can be further subdivided into self-sensing and modulation approaches. Self-sensing uses the driving currents to detect the MEMS mirror zero angle [24], and modulation-based approaches use the superposition of a high-frequency signal on top of the low-frequency driving signal to reconstruct the MEMS mirror position [25, 26].

1.3 Goal of the Thesis

To enable the successful deployment of MEMS mirrors in consumer products and industrial environments, the system must be designed for high performance and robustness. This thesis focuses on the controller design for MEMS mirrors with the goal of achieving robust scanning trajectories, even under the influence of external vibration. The main goals of this thesis are as follows:

- Identify the dynamics of the MEMS mirrors and develop model-based PLL controllers to minimize the pixel pointing uncertainty.
- Extend the controller to synchronize two individual MEMS mirrors, achieving a

1 Introduction

Lissajous pattern.

- Determine the influence of external vibration on the MEMS mirror trajectory and develop model-based controllers to diminish the uniformity of the Lissajous pattern.
- Investigate the dynamics of a 2D MEMS mirror, and apply the developed concepts to the 2D MEMS mirror.

CHAPTER 2

State of the Art

This chapter provides a brief literature overview on the current state of the art on resonant MEMS mirrors and their control. Since this work only uses comb drive-actuated electrostatic MEMS mirrors, the actuation and sensing of electrostatic MEMS mirrors are described in great detail. Additionally, the PLL is introduced as the de facto standard for driving resonant MEMS mirrors. The last section introduces a synchronization structure to achieve a uniform Lissajous pattern in a projection system with two individual MEMS mirrors.

2.1 Driving of Comb Drive Actuated MEMS Mirrors

Comb drive actuated MEMS mirrors can be driven by a digital driving voltage, proving simple circuit design and control by switching times. Considering that only pulling forces are applied by the comb drive, the driving voltage is switched on at the maximum amplitude and switched off when the angle of the MEMS mirror equals 0° . The MEMS mirror keeps moving, because of its moment of inertia. When it reaches the maximum deflection again, it is pulled to the center by the comb drive again. The driving scheme is depicted in Figure 2.1. The frequency of the driving signal is twice the MEMS mirror's oscillating frequency. If the driving signal is switched on at the maximum amplitude, and off at the zero-crossing of the MEMS mirror, i.e. has a duty cycle of 50 %, the injected energy is maximized because the MEMS mirror is not slowed down due to the driving voltage being on when the MEMS mirror is moving away from the center.

2.2 Self-Sensing of Resonant MEMS Mirrors

The MEMS mirrors used in this thesis use capacitive self-sensing via comb drives to obtain the position of the MEMS mirror [24]. Figure 2.2 (a) shows an illustration of the comb drives. The oscillating movement of the MEMS mirror causes the overlapping

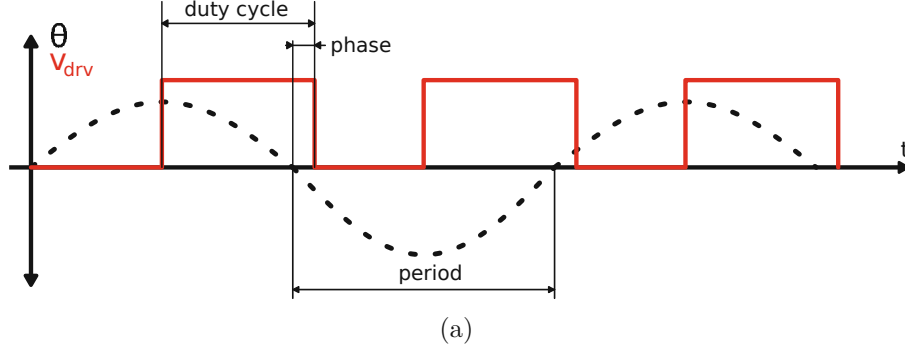


Figure 2.1: MEMS mirror angle θ and open-loop driving signal v_{drv} of the MEMS mirror defined by period and duty cycle, defining a steady state phase between driving and MEMS mirror angle.

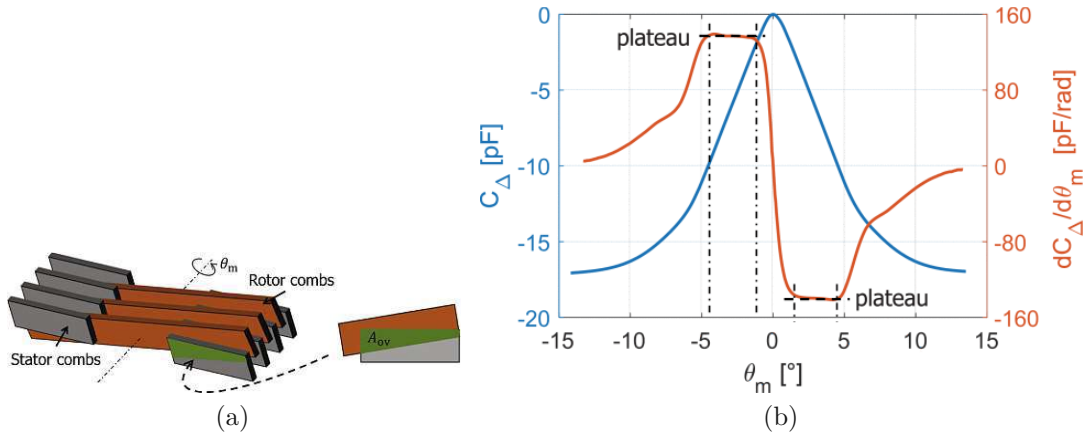


Figure 2.2: (a) Illustration of the comb drive fingers [27] (b) Nonlinear relation between the comb drive capacitance and angle of the MEMS mirror and the resulting actuation current [28, 24].

area of the comb drive fingers to vary, causing an increase or decrease in comb drive capacity. The maximum area is reached at 0° . The comb drives disengage at an angle of around 5° , and fully disengage at an angle of 12° . Therefore, the relation between capacity and angle is highly nonlinear, as shown in Figure 2.2 (b). The comb drive current is given by

$$I = \frac{d}{dt}VC = V\frac{dC}{dt} = V\frac{dC}{d\theta}\frac{d\theta}{dt}, \quad (2.1)$$

where the input voltage V is assumed to be constant and C is the comb drive capacitance. Due to the slope change at 0° the current shows a sharp edge when the MEMS mirror travels through 0° . This sharp current edge, as depicted in Figure 2.2 (b) can be detected by a comparator and used to reveal the 0° position of the MEMS mirror. The torque of the comb drive can be calculated with

$$\tau(t) = \frac{1}{2} \frac{dC}{d\theta} V^2(t), \quad (2.2)$$

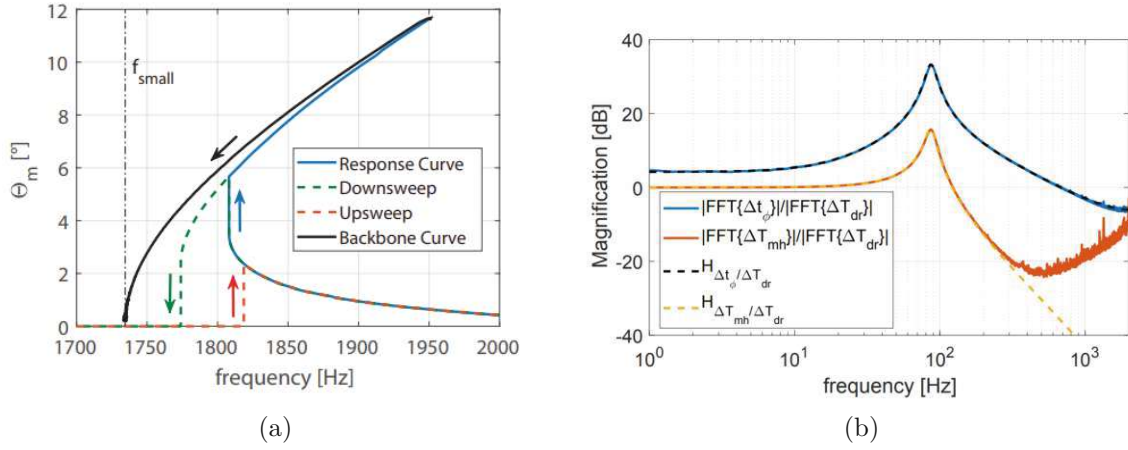


Figure 2.3: (a) Measured steady-state frequency response of the MEMS mirror. The arrows indicate bifurcations, where the amplitude jumps occur [24, 30]. (b) Local dynamics from input period T_{dr} to phase Δt and actual period T_{mh} of the MEMS mirror at a predefined operating point showing 2nd order behavior [31].

where $\frac{dC}{d\theta}$ is shown in Figure 2.2 (a) and $V(t)$ is the input voltage.

A self-sensing for comb drives, meaning that the driving comb is also used for sensing, is proposed in [28, 24]. The sensing is only possible if the driving voltage is turned on, therefore the switch-off timing in Figure 2.1 needs to be after the zero-crossing of the MEMS mirror. At around 5° the comb drives disengage, which is also reflected by a sharp current edge. This can be detected with a comparator with positive offset voltage and reveals an absolute measure of MEMS mirror amplitude, which can be used to implement an amplitude control.

2.3 MEMS Mirror Modeling and Dynamic Behavior

Due to the nonlinear stiffness of the MEMS mirror's torsion bars, the equation of movement of the MEMS mirror can be approximated by a duffing equation given by

$$I\ddot{\theta} + c(\Theta)\dot{\theta} + k(\theta)\theta = \tau(t), \quad (2.3)$$

where θ is the MEMS mirror angle, $\tau(t)$ is the external torque from the comb drive given by (2.2), $c(\Theta)$ is the nonlinear damping function, depending on the amplitude Θ and $k(\theta)$ is the nonlinear stiffness. An accurate modelling of the nonlinear behavior of the spring and comb drive torque can be found in [29]. Figure 2.3 (a) shows the response curve of the MEMS mirror, clearly showing the bending of the resonance frequency typical for the duffing oscillator with increasing stiffness of the torsion bars. Even though the system is highly nonlinear, for controller design it is sufficient to consider the local dynamics around a certain steady-state operating point given by a point on the response curve shown in Figure 2.3 (b). Locally, the system behaves similarly to a linear 2nd-order system. The local dynamics can be modeled directly via

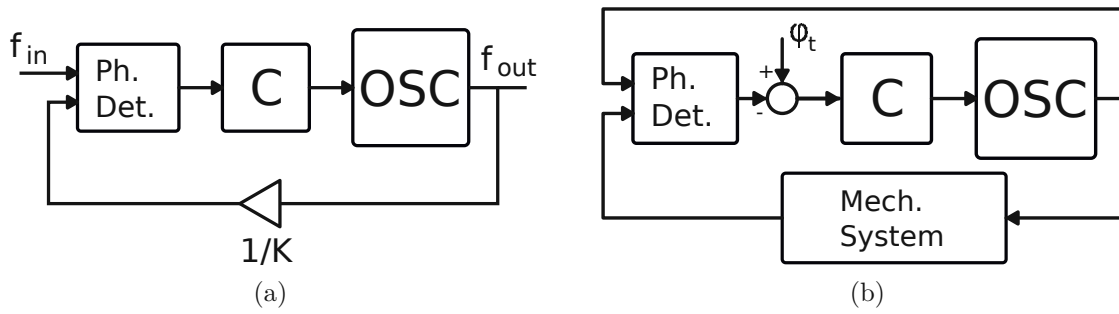


Figure 2.4: (a) Typical PLL used in digital circuits, consisting of a phase detector, a controller C, an oscillator, and a frequency divider or multiplier on the feedback path (b) PLL used to drive the mechanical systems. Instead of the frequency divider the mechanical system is placed on the feedback path. Furthermore, no reference frequency is connected, but the oscillator output frequency is used as a reference frequency

a period-to-period-based approach [31] or derived from the global parameters via perturbation theory [29]. Furthermore, the local resonance at around 100 Hz is much lower than the MEMS mirror oscillating frequency. The relation between the oscillating frequency and the local resonance frequency is highly nonlinear and depends on the comb drive capacitance curve depicted in Figure 2.2 as well as the spring stiffness [29].

2.4 Closed-Loop Control of Resonant MEMS Mirrors

The motion of the MEMS mirror is influenced by any errors in oscillation or environmental disturbances, such as temperature fluctuation or external vibration. External vibration couples into the MEMS mirror dynamics because of the misalignment of the center of mass and the rotational axis [32]. To compensate for these disturbances, a closed-loop controller can be applied to stabilize the MEMS mirror.

2.4.1 Single Axis Control by Phase Locked Loops

One common way to control the MEMS mirror is a phase locked loop (PLL). First, the typical PLL structure is explained and then extended to allow the control of MEMS mirrors. PLLs represent a basic component of all digital circuits. They are used to generate arbitrary frequencies out of a given reference frequency. Figure 2.4 (a) shows the typical PLL consisting of a phase detector, a loop filter, and an oscillator. PLLs are typically implemented with analog components. They are commonly used in microcontrollers and FPGAs to generate different clock domains for the components but are also applied extensively to control mechanical systems [33]. The phase detector measures the phase difference between the input and the output signal. In the analog domain, the phase detector outputs two signals representing a phase lead and a phase lag, which control a charge pump. The output voltage of the charge pump is then filtered and applied as the control voltage to the voltage-controlled oscillator, which

generates a frequency according to the analog voltage input. Recently, the all digital PLL (ADPLL) has emerged as an alternative to traditional analog PLL [34, 35, 36]. All-digital PLLs replace the components with digital implementations, which allows for an implementation in digital circuits without the need for external analog components. ADPLLs operate in a much wider range of frequencies and also support low-frequency applications. Furthermore, advanced loop filters can be easily implemented. In the digital case, the phase detector calculates the phase difference and outputs a digital value and the loop filter is a discrete-time system. The digitally controlled oscillator (DCO) is a circuit that generates an output signal with a frequency determined by its input. If analog output voltages are required, the DCO contains analog to digital converters.

Figure 2.4 (b) shows the PLL used to control a mechanical system [33, 37, 38]. Contrary to the typical application, where the PLL synchronizes to a reference frequency, the PLL synchronizes to the current oscillation period of the system. The phase detector compares the phase of the driving signal to the phase of the system response. Assuming a simple second-order system, which has a phase lag of 90° at resonance, the target phase of the phase detector needs to be set to -90° to stabilize the system with the PLL at the resonance frequency. Such an approach can be used to control the MEMS mirror [39, 40, 41].

Figure 2.5 (a) shows the open-loop driving signal for the MEMS mirror, and Figure 2.5 shows the driving signal generated by the PLL in closed-loop mode. The DCO period start represents the expected zero-crossings $z_{c,exp}$ at times $t_{zc,exp}$. The driving voltage is switched off \hat{s}_{off} clock cycles after the DCO period start and on \hat{s}_{on} clock cycles after the DCO period start. \hat{s}_{on} and \hat{s}_{off} therefore also define the duty cycle. The difference between the expected zero-crossing and the actual zero-crossings detected by observing the comb drive current is defined to be the phase error Δt . The PLL aims to reduce Δt to 0 by adjusting the driving period \hat{T} [27, 42].

2.4.2 Synchronization of Multiple Mirrors

When two resonant MEMS mirrors are used in a scanning scenario as shown in Figure 1.3 the trajectory of the laser spot follows a Lissajous pattern. However, the PLL adjusts the driving frequency of the MEMS mirror to achieve the predefined target phase. This means that due to external disturbances such as vibration the frequency of the MEMS mirror can vary slightly. These slight frequency variations cause the relative phase between the two MEMS mirrors to augment, which results in a nonuniform Lissajous pattern. To stabilize the frequency ratio and the relative phase between two MEMS mirrors additional control concepts are required.

One master-slave synchronization concept proposed in [43] synchronizes the slave MEMS mirror to the master mirror, by setting the PLL feedback signal of the slave MEMS mirror to the zero-crossing of the master MEMS mirror. This synchronizes the MEMS mirrors but disregards the zero-crossing signal of the slave MEMS mirror, which means that the slave axis is operated without closed-loop control.

An improvement can be achieved if also the slave axis is operated in closed-loop

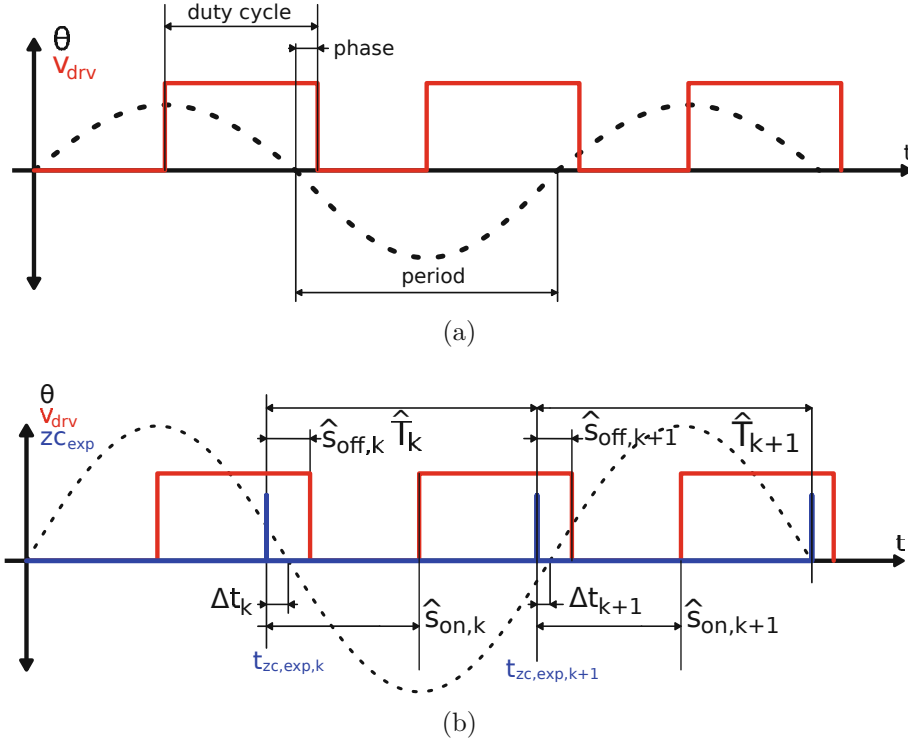


Figure 2.5: (a) open-loop driving signal of the MEMS mirror defined by period and duty cycle, defining steady state phase between driving and MEMS mirror angle. (b) Necessary definitions for the closed-loop driving of the MEMS mirror: The DCO period starts at the expected zero-crossings $t_{zc,exp}$ and the driving voltage is switched off \hat{s}_{off} clock cycles after the DCO period start and on \hat{s}_{on} clock cycles after the start of the DCO period. The difference between the expected zero-crossings, i.e. the start of the DCO period, and the actual measured zero-crossings is the phase error Δt .

mode. Figure 2.6 shows the synchronization concept for multiple MEMS mirrors, where each MEMS mirror is operated at their resonance with a PLL [44]. Furthermore, an additional feedback loop consisting of a phase detector and a loop filter is implemented to achieve synchronization between the two MEMS mirrors by synchronizing one MEMS mirror to the reference frequency determined by the other MEMS mirror. This master-slave synchronization structure provides a simple but effective closed-loop control of two MEMS mirrors. [45] uses a similar master-slave architecture for the control of piezoelectric MEMS mirror

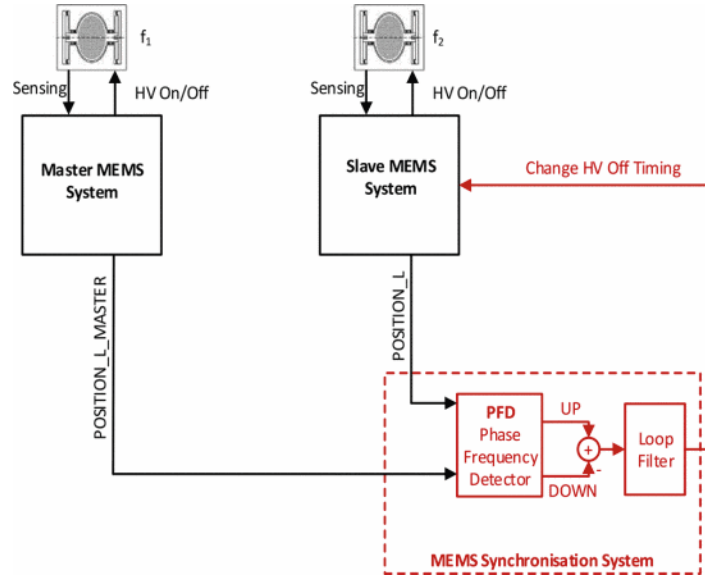


Figure 2.6: Controller structure used to synchronize two MEMS mirrors that are both operated by a PLL [44]

2.5 Scope of the Thesis

The MEMS mirror has been studied extensively in the literature for various potential applications. To allow a successful use in a commercial environment and especially in the automotive environment robustness against strong external vibration is required. The harsh environmental conditions require an appropriate controller design. PI control represents a widely-used control design approach, because of its simplicity and possibility to design without a model obtained by system identification. However, model-based control designs such as LQG control and H_∞ , which can outperform PI controllers, have not been investigated much yet. Therefore, the first research question that arises is:

Research Question 1 Can model-based control and systematic incorporation of the disturbance improve the closed-loop performance of the PLL for resonant MEMS mirrors?

For a synchronization scenario, a single PLL is not sufficient and an additional synchronization controller is necessary. In the state of the art, a synchronization concept with an additional PI controller on top of the PLL is proposed [43]. Such a synchronization concept can cause conflicts between controllers leading to a degraded performance. This synchronization concept leads to the second research question as follows:

Research Question 2 Does the synchronization concept with a synchronization controller on top of the PLL-operated MEMS mirror cause performance competition? And if so, how can this issue be avoided?

The synchronized movement of two MEMS mirrors projects a Lissajous pattern to the screen. The strong external vibration of an automotive environment disturbs the

trajectories of the MEMS mirror, causing severe deformations of the Lissajous pattern. The controller design significantly influences the uniformity of the Lissajous pattern. This leads to the third research question as follows:

Research Question 3 Can model-based control methods improve the performance of the synchronization controller under external vibration influence to achieve a more uniform Lissajous pattern?

A 2D MEMS mirror is especially interesting for commercial products, because of the reduced size and the minimal complexity of the optical system apart from the MEMS mirror itself. However, 2D MEMS mirrors suffer from additional control challenges such as crosstalk and coupling between the MEMS mirror axes. Therefore, the fourth research question that arises is:

Research Question 4 Can the developed control concepts also be applied to a 2D MEMS mirror?

The rest of the thesis is organized as follows. Chapter 3 designs three different PLL controllers, a PI-based PLL, an LQG-based PLL, and an H_∞ -based PLL. Then, the controllers are compared by their performance to reject external vibration applied to the mirror via a piezo-actuated shaker. Chapter 4 introduces the problem of synchronization of two individual 1D MEMS mirrors, and describes two possible solutions. First, a synchronization controller is implemented on top of the PLL-driven MEMS mirrors, and second the novel direct correction PLL is introduced. The research is also extended to a 2D MEMS mirror in Chapter 5. Finally Chapter 6 sums up the work done in this thesis by providing answers to the research questions and gives an outlook on topics that require further investigation.

CHAPTER 3

Single Axis MEMS Mirror Control

The typical PLL to drive the MEMS mirror changes the driving period of the MEMS mirror such that a desired phase is achieved, which corresponds to a specific frequency. Achieving a small phase error Δt means that the PLL and the MEMS mirror are in sync, i.e. actual and expected zero-crossings line up. In this case, the laser can be triggered based on the interpolation of the PLL period to project an image on the screen. This section introduces and compares several controller design approaches for the PLL's controller to achieve a small phase error Δt even under the influence of a external vibration of an extended automotive standard.

3.1 Identification of the Local Dynamics

Model-based control methods require a model of the dynamic system to be controlled. The MEMS mirror is a nonlinear system with the response curve depicted in Figure 3.1. However, for the controller design, it is not necessary to consider the global nonlinear dynamics, but a linear model around the point is sufficient. The linearization is performed at an operating point is defined by the triple $[T_{\text{lin}} \ s_{\text{on,lin}} \ s_{\text{off,lin}}]$, where T_{lin} is the driving period, $s_{\text{on,lin}}$ and $s_{\text{off,lin}}$ are the switching points of the driving voltage, which also define the duty cycle. Splitting into the operating point and small variation around it gives

$$\begin{aligned}\hat{s}_{\text{off}} &= s_{\text{off,lin}} + s_{\text{off}}, \\ \hat{s}_{\text{on}} &= s_{\text{on,lin}} + s_{\text{on}}, \\ \hat{T} &= T_{\text{lin}} + T,\end{aligned}\tag{3.1}$$

where \hat{s}_{off} , \hat{s}_{on} , \hat{T} are the signal applied to the system and s_{off} , s_{on} , T are small deviations from the operating point. The duty cycle can be calculated by

$$D = 1 - \frac{\hat{s}_{\text{on}} - \hat{s}_{\text{off}}}{\hat{T}}.\tag{3.2}$$

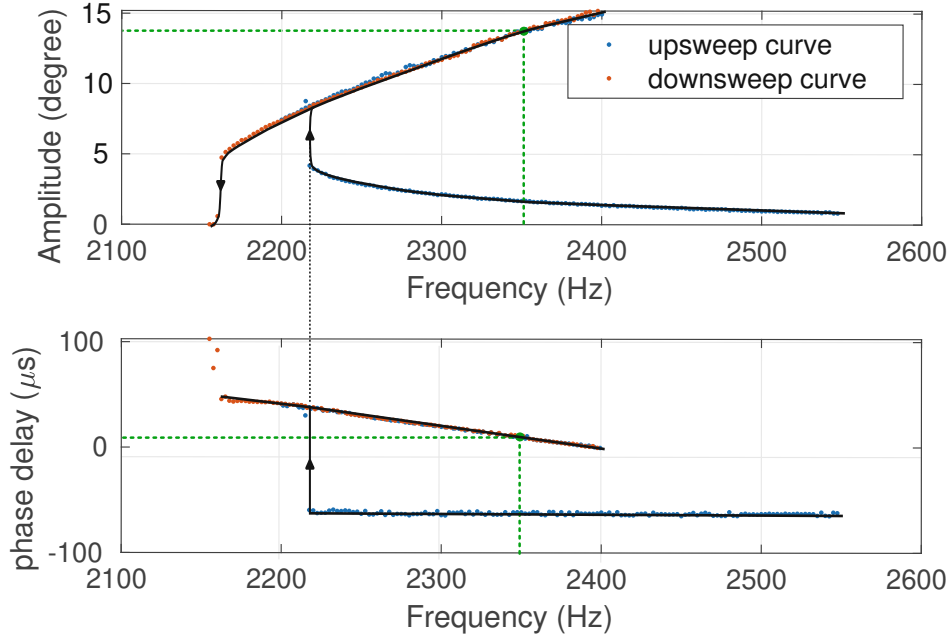


Figure 3.1: MEMS mirror response curve. The blue dots show data points measured during startup of the mirror, and the blue dots show data points measured during shutdown. The black line is an interpolation, showing the typical characteristic of a Duffing oscillator with increasing nonlinear stiffness. The green dots mark the operating point.

A constant duty cycle can be achieved by setting $s_{\text{off}} = s_{\text{on}}$. The duty cycle is then given solely by the values at the operating point $s_{\text{off,lin}}$ and $s_{\text{on,lin}}$ as

$$D = 1 - \frac{s_{\text{on,lin}} - s_{\text{off,lin}}}{\hat{T}}. \quad (3.3)$$

Figure 3.1 shows the nonlinear response curve of the MEMS mirror for a duty cycle of 57 %. Any point on the curve corresponds to a certain operating point consisting of period and phase.

Let P_{soff} denote the transfer function from s_{off} to Δt , and P_{son} denote the transfer function from s_{on} to Δt . If the duty cycle is constant, i.e. $s_{\text{on}} = s_{\text{off}}$, then $P_s = P_{\text{son}} + P_{\text{soff}}$ is used to denote the effect of an input on $s_{\text{on}} = s_{\text{off}}$.

The torque of the comb drive is given by

$$\tau = \frac{1}{2} \frac{dC}{d\theta} V^2(t), \quad (3.4)$$

where $\frac{dC}{d\theta}$ is the angular derivative of the nonlinear comb drive capacitance shown in Figure 2.2. As the the MEMS mirror is switched on at the maximum angle, s_{on} hardly influences the produced torque, since $\frac{dC}{d\theta}$ is small compared to $\frac{dC}{d\theta}$ at the switch-off timing \hat{s}_{off} [31] and the approximation $P_s \approx P_{\text{soff}}$ holds. Therefore, \hat{s}_{on} is kept constant, and only \hat{s}_{off} is used to control the MEMS mirror.

3 Single Axis MEMS Mirror Control

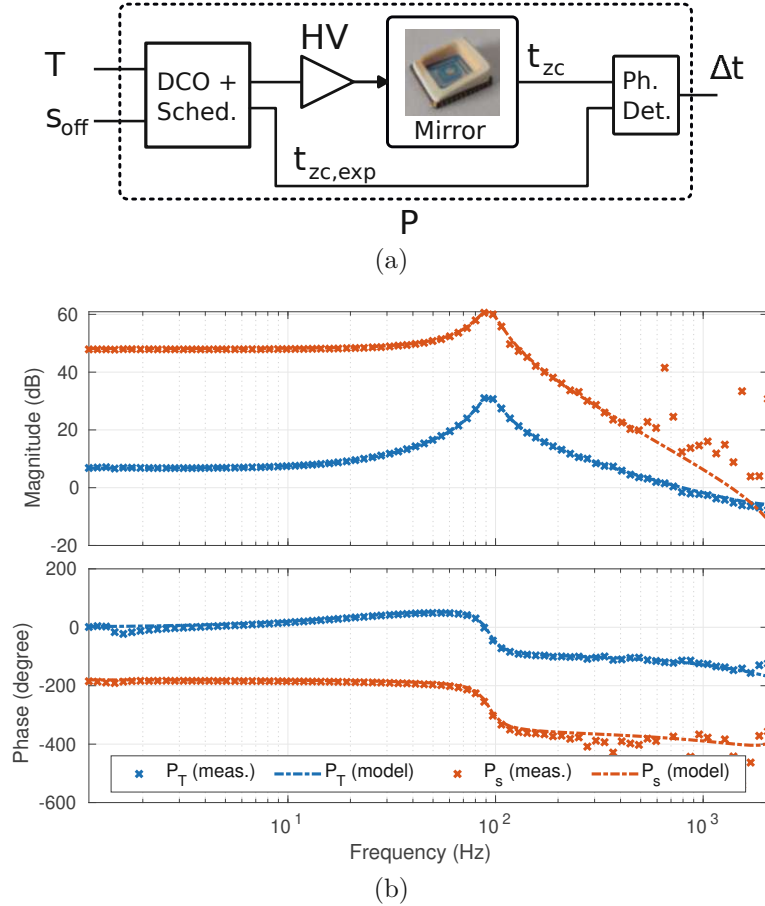


Figure 3.2: (a) Components identified together to obtain the local dynamics of the MEMS mirror: DCO and scheduler, MEMS mirror and phase detector. (b) Local dynamics of the MEMS mirror identified by applying a sine-sweep on the DCO period input T and on the switch-off timing s_{off} of the driving voltage s_{off}

The local model defined by transfer functions P_s and P_T can be derived mathematically from the global dynamics by perturbation theory [46] which has been done many times [29, 42, 47]. However, instead of identifying the global dynamics and deriving the local dynamics from it, it is also possible to identify the local dynamics directly by measurements. The model of the local dynamics includes the DCO, the MEMS mirror, and the phase detector to measure the error between zero-crossings and the expected zero-crossing of the controller, as depicted in Figure 3.2 (a). Figure 3.2 (b) shows the two identified transfer functions P_s and P_T and the fitted 2nd order model. Even though both transfer functions have been identified separately, they are not independent. In [31] a derivation of the local model by a period-to-period approach is provided. Another way to find the relation between the two transfer functions is to consider the driving signal which is applied to the MEMS mirror. Since the MEMS mirror only experiences a single driving signal, the actual DCO period and switch-on and switch-off times are only known to the controller. More intuitively speaking, from a MEMS mirror perspective it is not possible to distinguish between changes in $s_{\text{on}} = s_{\text{off}}$ or changes in T . Performing

3 Single Axis MEMS Mirror Control

all the calculation in clock cycles and assuming a driving period \hat{T}_k and a phase offset of \hat{s}_{off} , the driving signal of the k -th period is switched on at

$$t_{\text{on},k} = \sum_{i=0}^{k-1} \hat{T}_i + \hat{s}_{\text{on},k}, \quad (3.5)$$

and switched off at

$$t_{\text{off},k} = \sum_{i=0}^{k-1} \hat{T}_i + \hat{s}_{\text{off},k}. \quad (3.6)$$

Now consider \hat{s}_{off} to be a step by a constant value Δx at period $k = 1$

$$\hat{s}_{\text{off},k} = \begin{cases} s_{\text{off},\text{lin}}, & k \leq 0, \\ s_{\text{off},\text{lin}} + \Delta x, & k > 0. \end{cases} \quad (3.7)$$

With this input step and constant period $\hat{T}_k = T_{\text{lin}}$ the switch-off times given in (3.6) calculate to

$$t_{1,\text{off},k} = \begin{cases} kT_{\text{lin}} + s_{\text{off},\text{lin}}, & k \leq 0, \\ kT_{\text{lin}} + s_{\text{off},\text{lin}} + \Delta x, & k > 0, \end{cases} \quad (3.8)$$

A pulse input at timestep $k = 0$ at the period input, i.e.

$$\hat{T}_k = \begin{cases} T_{\text{lin}} + \Delta x, & k = 0, \\ T_{\text{lin}}, & k \neq 0, \end{cases} \quad (3.9)$$

on the period input and constant $s_{\text{off},k} = s_{\text{off},\text{lin}}$ results in the following turn-off times

$$t_{2,\text{off},k} = \begin{cases} kT_{\text{lin}} + s_{\text{off},\text{lin}}, & k \leq 0 \\ kT_{\text{lin}} + s_{\text{off},\text{lin}} + \Delta x, & k > 0. \end{cases} \quad (3.10)$$

A similar calculation can be performed for switch on times $t_{\text{on},k}$. Equation (3.8) and (3.10) show that the driving signal for the MEMS mirror is identical if s_{off} is a step function or T is given by a pulse at $k = 0$. Figure 3.3 illustrates the pulse input on the period and the step input on s_{off} and s_{on} . Both driving signals result in the same MEMS mirror high-voltage signal, therefore the MEMS mirror must show the same behavior. Since local dynamics around the operating point are investigated the local deviation from the operating point $T_k = \hat{T}_k - T_{\text{lin}}$ is given by

$$T_k = \begin{cases} \Delta x, & k = 0, \\ 0 & k \neq 0, \end{cases} \quad (3.11)$$

and the corresponding z-transformation is Δx . Similarly, the z-transformation of the input step at time $k = 1$ on s_{off} and s_{on} is given by $\frac{\Delta x}{z-1}$. Therefore, the phase errors for both signals can be calculated with

$$\Delta t_T = P_T \Delta x \quad (3.12)$$

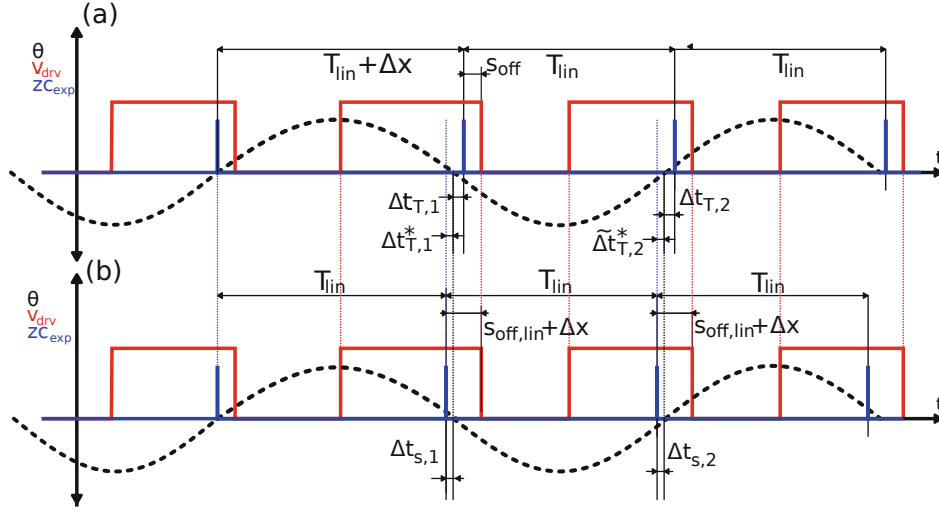


Figure 3.3: Illustration to understand the identity of different driving signals: (a) shows a pulse input on T and (b) shows a step input on s_{off} and s_{on} . Since result in the same driving signals, the mirror response also must be identical.

and

$$\Delta t_s = P_s \frac{\Delta x}{z - 1}. \quad (3.13)$$

The pulse input on the period also changes the expected zero-crossings by shifting them by Δx in all periods $k > 0$, as shown in Figure 3.3. Since the phase error Δt is calculated as the difference between the actual zero-crossing and the expected zero-crossing, the phase error Δt_T and Δt_s will be different even though the zero-crossings happened at the same absolute time. Compensating for the shift by Δx in expected zero-crossings in Δt_T results in

$$\Delta t_T^* = \Delta t_T - \frac{\Delta x}{z - 1}. \quad (3.14)$$

Finally the phase errors Δt_T^* and Δt_s can be compared, and must be identical, because the driving signals are identical. Setting $\Delta t_T^* = \Delta t_s$ gives

$$\begin{aligned} P_s \frac{\Delta x}{z - 1} &= P_T \Delta x - \frac{\Delta x}{z - 1}, \\ P_s &= P_T(z - 1) - 1, \end{aligned} \quad (3.15)$$

or equivalently

$$\frac{P_s + 1}{z - 1} = P_T. \quad (3.16)$$

In the concrete setup the period is implemented in a Q22.8 format, i.e. has 8 fractional bits, while s_{off} and s_{on} are measured in clock cycles. Therefore an additional scaling factor needs to be added to Equation (3.16) to obtain

$$P_s = 256(P_T(z - 1) - 1). \quad (3.17)$$

3 Single Axis MEMS Mirror Control

The transfer function shown in Figure 3.2 (b) obey to this constraint, i.e. only the measurement data from P_T is used and P_s is calculated from it. The measured data for P_s is only used to verify that (3.17) is valid.

A few more mathematical compensations can be used to achieve a more accurate modelling. First, per definition Δt_k is measured at the beginning of the DCO period, therefore T_k and s_k have no influence on Δt_k , but only on Δt_{k+1} . This means that the model has no direct feedthrough and can be written as

$$P_T = \frac{b_{T1}z + b_{T0}}{z^2 + a_{T1}z + a_{T0}}, \quad (3.18)$$

and

$$P_s = \frac{b_{s1}z + b_{s0}}{z^2 + a_{s1}z + a_{s0}}. \quad (3.19)$$

Because of (3.17) the denominators of P_T and P_s have to be identical that means $a_{T0} = a_{s0} = a_0$ and $a_{T1} = a_{s1} = a_1$. This results in equal resonances, which also is visible in Figure 3.2 (b). Furthermore, P_s per definition must not have direct feedthrough, i.e. z^2 does not show up in the numerator. Combining (3.18) and (3.17) gives additional constraints on the numerator coefficients. Using (3.17) the numerator of P_s calculates to

$$\begin{aligned} & 256((b_{T1}z + b_{T0})(z - 1) - (z^2 + a_1z + a_0)) = \\ & 256(b_{T1}z^2 + (b_{T0} - b_{T1})z - b_{T0} - z^2 - a_1z - a_0) \end{aligned} \quad (3.20)$$

From previous considerations it is known that no z^2 term must show up in the numerator, therefore it is possible to conclude that $b_{T1} = 1$. This implies that it is sufficient to identify the three parameters a_1 , a_0 and b_{T0} . Furthermore, (3.20) shows that the coefficients $b_{s1} = 256(b_{T0} - b_{T1} - a_1)$ and $b_{s0} = 256(-b_{T0} - a_0)$. If P_s is measured, Equation (3.16) can be used to calculate P_T , and a similar constraint can be derived, i.e. 3 parameters are sufficient to describe the MISO model.

The linear model derived by a period-to-period energy conservation approach in [31] can also be used to derive (3.16). The detailed calculation steps are given in Appendix 6.1. Since the two transfer functions have the same denominator because of (3.17) they can be written in a single MISO system of the form

$$\begin{aligned} x_{k+1} &= \overbrace{\begin{bmatrix} -a_1 & 1 \\ -a_0 & 0 \end{bmatrix}}^{A_P} x_k + \overbrace{\begin{bmatrix} 1 & b_{s1} \\ b_{T0} & b_{s0} \end{bmatrix}}^{B_P} \begin{bmatrix} T \\ s \end{bmatrix}, \\ y_k &= \overbrace{\begin{bmatrix} 1 & 0 \end{bmatrix}}^{C_P} x_k. \end{aligned} \quad (3.21)$$

Since s_{on} does not significantly contribute to the torque with a duty cycle of 57 %, only s_{off} is modified on the setup. The input of the system given in (3.21) is set to $\begin{bmatrix} T & s_{off} \end{bmatrix}'$ without any modifications to the matrices.

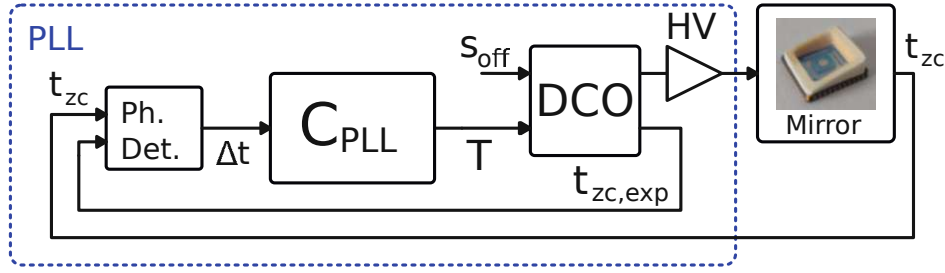


Figure 3.4: Block diagram of the PLL used to control the MEMS mirror.

3.2 Controller Design

This section presents different PLL controller designs based on the identified model and compares them by their performance to reject the external vibration applied to the MEMS mirror.

Figure 3.4 illustrates the control loop consisting of the PLL controller C_{PLL} and the MEMS mirror model P , which includes the DCO, MEMS mirror and the phase detector, as depicted in Figure 3.2 (a). Three different controllers will be discussed in the following: A simple PI controller, a model-based LQG controller and an H_∞ controller.

3.2.1 PI Control

A simple stabilizing controller can be implemented as a discrete PI controller with the form $C_{PLL,PI} = k_p + \frac{k_i}{z-1}$. The identified transfer function P_T allows to the gains k_p and k_i to be chosen by a loop shaping approach [48]. Figure 3.5 shows the transfer function of the plant P_T , the controller transfer function $C_{PLL,PI}$ and the loop transfer function $L = C_{PLL,PI}P_T$. The controller reaches a crossover frequency of 500 Hz and a phase margin of 26.2° . Furthermore, the transfer function $T_{\Delta t,PI} = \frac{P_s}{1+P_TC_{PLL,PI}}$ from s_{off} to Δt is plotted. Its verification, shown by purple markers and performed by applying a sine sweep on the s_{off} input, demonstrates that the implementation has been successful. $T_{\Delta t,PI}$ can be considered to be a load disturbance sensitivity function, and s_{off} can be regarded as external disturbance. Previous research has shown that vibrations strongly influence the system at the local resonance [32], therefore it accurately represents the external vibration.

3.2.2 LQG Control

Linear quadratic Gaussian control is a modern state-space technique for designing optimal controllers [49]. The technique takes into account the process disturbances and measurement noise and allows to trade off regulation performance and control effort. Due to the separation principle [50] it is possible to design a linear quadratic regulator (LQR), which is an optimal state-feedback controller and an optimal state observer in form of a Kalman filter individually and combine them to form the LQG controller.

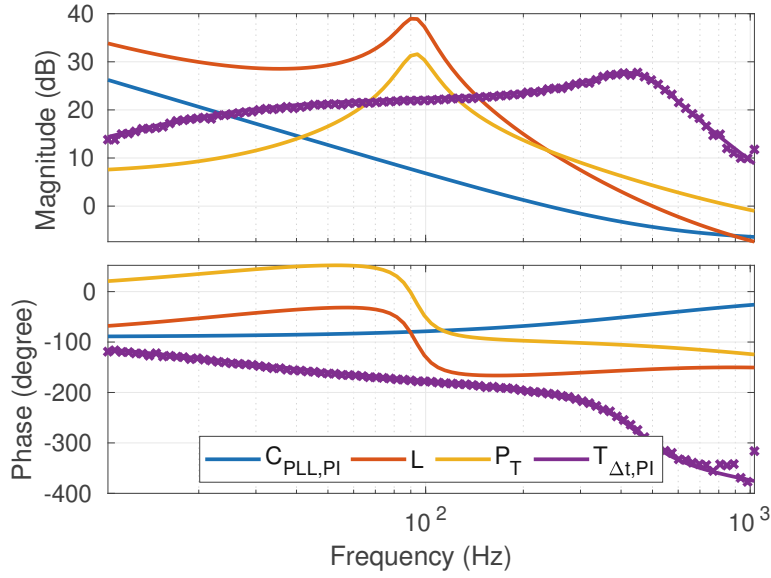


Figure 3.5: Frequency response of the transfer function plant transfer function P_T , the controller transfer function $C_{PLL,PI}$ and the open-loop transfer function L . Furthermore, the load disturbance sensitivity function $T_{\Delta t,PI}$ from s_{off} to Δt shows how well the controller rejects disturbances. The measured verification of $T_{\Delta t,PI}$, showed by the purple markers, shows that the implementation was successful.

Linear Quadratic Regulator (LQR)

The LQR is an optimal state feedback controller that minimizes the value of the cost given by

$$J = \sum_{k=0}^{\infty} (x_k^T Q x_k + u_k^T R u_k), \quad (3.22)$$

to find the optimal control sequence given by

$$u_k^* = -K x_k, \quad (3.23)$$

where Q is the weighting matrix of the states. Higher entries in Q allow the state to converge faster to 0. R is the weighting matrix for the controller input, which limits the controller action. The solution for K for the system

$$\begin{aligned} x_{k+1} &= A x_k + B u_k, \\ y_k &= C x_k \end{aligned} \quad (3.24)$$

is given by [49]

$$K = (R + B^T P B)^{-1} B^T P A, \quad (3.25)$$

where P is the solution to the discrete algebraic Riccati equation

$$P = A^T P A - A^T P B (R + B^T P B)^{-1} B^T P A + Q. \quad (3.26)$$

To ensure zero residual error under constant disturbances and regardless of small modelling errors the common approach of extending the system by an integrator is followed [49, 51]. The extended system is

$$\begin{aligned} A_{P,\text{ext}} &= \begin{bmatrix} A_P & 0 \\ C_P & 1 \end{bmatrix}, \\ B_{P,\text{ext}} &= \begin{bmatrix} B_{P,1} \\ 0 \end{bmatrix}, \end{aligned} \quad (3.27)$$

where $B_{P,1}$ is the first column of the $B_P = \begin{bmatrix} B_{P,1} & B_{P,2} \end{bmatrix}$ matrix i.e. the part responsible for the input T . Since only T is controlled by the PLL, $B_{P,2}$ does not show up in the LQR equations. The LQR problem is solved with MATLAB for the extended system given by $A_{P,\text{ext}}$ and $B_{P,\text{ext}}$ to obtain K , which is often divided into $K = \begin{bmatrix} K_x & K_i \end{bmatrix}$ where K_x is the state-feedback gain and K_i is the gain of the integrating state. The entries of the Q matrix have been chosen to $Q = \text{diag} \begin{bmatrix} 1 & 10^{-5} & 10^{-2} \end{bmatrix}$. This weights the first state much more than the second state, because the system has been transformed previously such that $C_P = \begin{bmatrix} 1 & 0 \end{bmatrix}$ i.e. the phase error Δt equals the first state. The last state is the integrating state. The controller output weighting matrix R equals 1.

Kalman Filter

The LQR requires the system state, which can not be directly measured in the MEMS mirror system. Therefore a state estimator in form of a Kalman filter is designed to complete LQG control. The estimation problem is defined in a stochastic system, i.e. d_k and n_k are zero-mean Gaussian random variables and the state and outputs are defined by random variables as well. The system for which the state estimation has to be performed is given by

$$\begin{aligned} x_{k+1} &= A_P x_k + B_{P,1} T_k + B_{P,2} d_k, \\ \Delta t_k &= C_P x_k + n_k, \end{aligned} \quad (3.28)$$

where $B_{P,1}$ is the first column of B_P and $B_{P,2}$ is the second column of B_P , i.e. $B_P = \begin{bmatrix} B_{P,1} & B_{P,2} \end{bmatrix}$. This choice fixes the process noise d_k to be a disturbance on the s_{off} input of the system, while only the input T is used to control the system. This choice is reasonable because it considers that disturbances on s_{off} do not change the expected zero-crossing time, while a disturbance on T would and does therefore not represent a disturbance scenario that can occur. n_k represents the measurement noise, originating from the phase detector. The discrete time estimator performs an update step and an extrapolation step. During the update step

$$\hat{x}_{k|k} = \hat{x}_{k|k-1} + M_x (y_k - C_P \hat{x}_{k|k-1}) = (I - M_x C_P) \hat{x}_{k|k-1} + M_x y_k, \quad (3.29)$$

the estimated state $\hat{x}_{k|k-1}$ considering $k-1$ measurements is updated by the measurement Δt_k to obtain the state estimation $\hat{x}_{k|k}$ considering k measurements. I is the identity matrix with correct dimensions, and M_x is the innovation gain of the estimator.

3 Single Axis MEMS Mirror Control

The extrapolation step

$$\hat{x}_{k+1|k} = A_P \hat{x}_{k|k} + B_{P,1} T_k, \quad (3.30)$$

updates the estimated state $x_{k|k}$ by running a simulation step of the system with input T_k . M_x is given by the solution to the discrete algebraic Riccati equation [49]

$$P = A_P P A_P^T + B_{P,2} Q_n B_{P,2}^T - A_P^T P C_P^T (C_P P C_P^T + R_n)^{-1} C_P P A_P^T, \quad (3.31)$$

and

$$M_x = P C_P^T (C_P P C_P^T + R)^{-1}. \quad (3.32)$$

The matrices Q_n , R_n are given by the properties of the disturbance and noise signals

$$\begin{aligned} Q_n &= E(d_k d_k^T), \\ R_n &= E(n_k n_k^T). \end{aligned} \quad (3.33)$$

The controller calculation is always started after a zero-crossing measurement is taken. That means that Δt_k is available as measurement, but $\begin{bmatrix} T_k & s_{\text{off},k} \end{bmatrix}$ are not applied to the system yet. This facilitates the use of a *current* Kalman estimator that outputs the state estimation using up to k measurements. So instead of the Kalman estimator output being $\hat{x}_{k|k-1}$ the output is $\hat{x}_{k|k}$, as given by (3.29). To sum up, the 4 system matrices of the Kalman filter are given in (3.34)

$$\begin{aligned} A_{\text{kal}} &= A_P (I - M_x C_P), \\ B_{\text{kal}} &= \begin{bmatrix} B_{P,1} & A_P M_x \end{bmatrix}, \\ C_{\text{kal}} &= I - M_x C_P, \\ D_{\text{kal}} &= \begin{bmatrix} 0 & M_x \end{bmatrix}, \end{aligned} \quad (3.34)$$

and the full system is given by

$$\begin{aligned} \hat{x}_{k+1|k} &= A_{\text{kal}} \hat{x}_{k|k-1} + B_{\text{kal}} \begin{bmatrix} T_k \\ \Delta t_k \end{bmatrix}, \\ \hat{x}_{k|k} &= C_{\text{kal}} \hat{x}_{k|k-1} + D_{\text{kal}} \begin{bmatrix} T_k \\ \Delta t_k \end{bmatrix}. \end{aligned} \quad (3.35)$$

Linear Quadratic Gaussian Control

The separation principle [50] allows the Kalman filter and the LQR to be designed separately. Afterward, they can be simply combined into a single system that outputs T_k given Δt_k . Including the beforementioned integrator this results in the output equation

$$T_k = -K_x \hat{x}_{k|k} - K_i x_{i,k} \quad (3.36)$$

$$= -K_x (C_{\text{kal}} \hat{x}_{k|k-1} + M_x \Delta t_k) - K_i x_{i,k}, \quad (3.37)$$

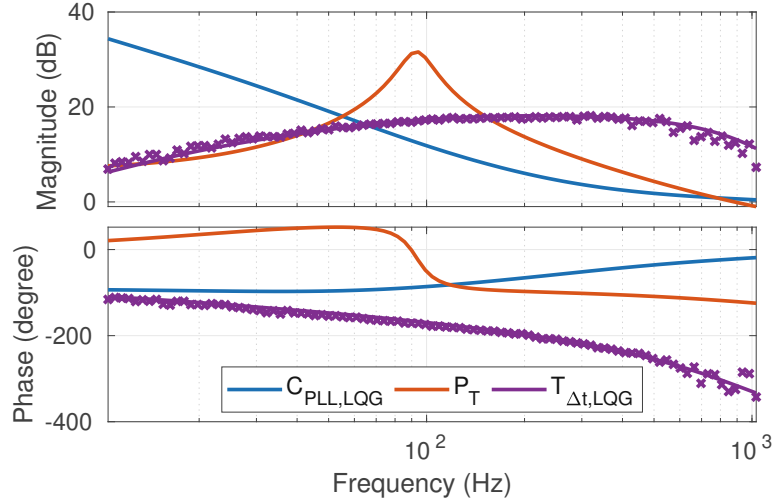


Figure 3.6: Frequency response of the LQG controller $C_{\text{PLL,LQG}}$, the plant P_T and the load disturbance sensitivity function $T_{\Delta t, \text{LQG}}$. The measured verification of $T_{\Delta t, \text{LQG}}$, showed by the purple markers, demonstrates that the implementation was successful.

where $x_{i,k}$ is the integrating state given by the equation $x_{i,k+1} = x_{i,k} + \Delta t$. Substituting Equation (3.37) into Equation (3.35) results in a combined system with input Δt and a single output T given by

$$\begin{aligned} \begin{bmatrix} x_{i,k+1} \\ \hat{x}_{k+1|k} \end{bmatrix} &= \overbrace{\begin{bmatrix} 1 & 0 & 0 \\ -B_{P,1}K_i & A_{\text{kal}} - B_{P,1}K_x C_{\text{kal}} \end{bmatrix}}^{A_{\text{LQG}}} \begin{bmatrix} x_{i,k} \\ \hat{x}_{k|k-1} \end{bmatrix} + \overbrace{\begin{bmatrix} 1 \\ A_P M_x - B_{P,1}K_x M_x \end{bmatrix}}^{B_{\text{LQG}}} \Delta t_k \\ T_k &= \overbrace{\begin{bmatrix} -K_i & -K_x C_{\text{kal}} \end{bmatrix}}^{C_{\text{LQG}}} \begin{bmatrix} x_{i,k} \\ \hat{x}_{k|k-1} \end{bmatrix} + \overbrace{-K_x M_x \Delta t_k}_{D_{\text{LQG}}} \end{aligned} \quad (3.38)$$

Figure 3.6 shows the transfer function of the plant P_T , the controller transfer function $C_{\text{PLL,LQG}}$. Figure 3.6 also shows loop disturbance sensitivity function $T_{\Delta t, \text{LQG}} = \frac{P_s}{1 + P_T C_{\text{PLL,LQG}}}$, and the verification of it, demonstrating that the implementation was successful.

3.2.3 H_∞ Control

Another option to design the controller is to use the H_∞ loop shaping approach. The controller problem is expressed in a general framework and algorithms can be used to minimize the H_∞ norm of the closed-loop system yielding a robust stabilizing controller.

First of all the problem needs to be expressed in the standard configuration as depicted in Figure 3.7 (a). The plant inputs are divided into exogenous inputs w , which include disturbances and reference signals and manipulated inputs u , which can be used by the controller K . The outputs are divided into the controlled outputs z and the measured

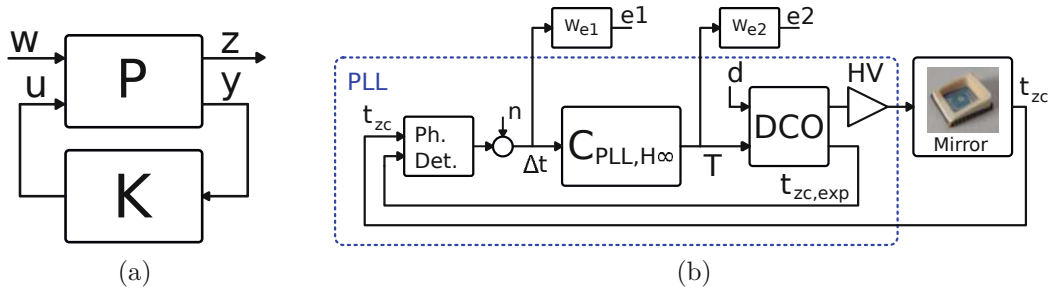


Figure 3.7: (a) General H_∞ controller framework (b) Controller loop with disturbance input d and measurement noise input v , and the two weighting functions W_{e1} and W_{e2} used to tune the controller

outputs z , that are available as input to the controller. The controlled outputs also include virtual error outputs which are introduced to the tune the system but don't exist in the real system.

The H_∞ controller design algorithm minimizes the H_∞ norm from the exogenous input w to the controlled outputs z . Introducing the transfer function matrix $F_l(P, C_{PLL,H_\infty})$, which depends on the plant P and the controller C_{PLL,H_∞} , the controlled outputs can be expressed as $z = F_l(P, C_{PLL,H_\infty})w$. The H_∞ norm of the closed-loop transfer function $F_l(P, C_{PLL,H_\infty})$ is defined as

$$\|F_l(P, C_{PLL,H_\infty})\|_\infty = \sup_{\omega} \bar{\sigma}(F_l(P, C_{PLL,H_\infty})), \quad (3.39)$$

where $\bar{\sigma}(\cdot)$ denotes the largest singular value. In the single-input single-output (SISO) case, the largest singular value corresponds to the worst-case amplification of the disturbance w to the performance output z , which means that the H_∞ optimization minimizes the worst-case amplification of the disturbance. The MATLAB command `hinfsyn` was used for the H_∞ controller design.

Figure 3.7 (b) shows the PLL and MEMS mirror with the disturbance and noise input d and n . The only measured output of the MEMS mirror system is the phase error Δt , and the only controlled input is the DCO period T . The way to influence the controller design is by adding weighting functions, that define the desired behavior of the controlled outputs. Although arbitrarily many weighting functions can be added, the common approach of adding two weighing functions [52] has been followed. W_{e1} is the sensitivity weighting function, and W_{e2} is the weighing function that limits the controller actions. The sensitivity function should show high-pass behavior i.e. low frequencies should be rejected very well. Therefore, the sensitivity weighting function must show low-pass behavior. The controller weighting function should be a high-pass function. This punishes high-frequency controller actions and therefore minimizes the energy consumption of the system.

Figure 3.8 shows the selected weighting functions. Figure 3.9 shows the transfer function of the H_∞ controller C_{PLL} , the plant transfer function P_T , and the load disturbance sensitivity function $T_{\Delta t, H_\infty}$. The weighting functions define the shape of the sensitivity functions. Therefore, the shape of the inverse of the sensitivity weighting function

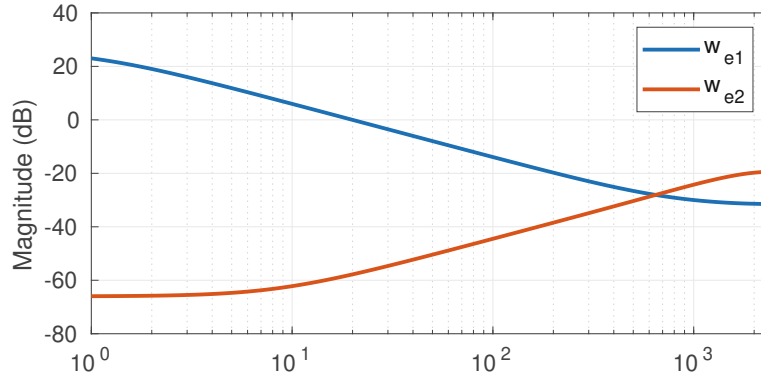


Figure 3.8: Weighting functions selected for the H_∞ controller. W_{e1} is the sensitivity weighting function, which shows a low pass characteristic, forcing the closed-loop system to a high pass behavior. W_{e2} is the controller output weighting function, which limits the controller action. A high pass behavior restricts high frequency controller actions.

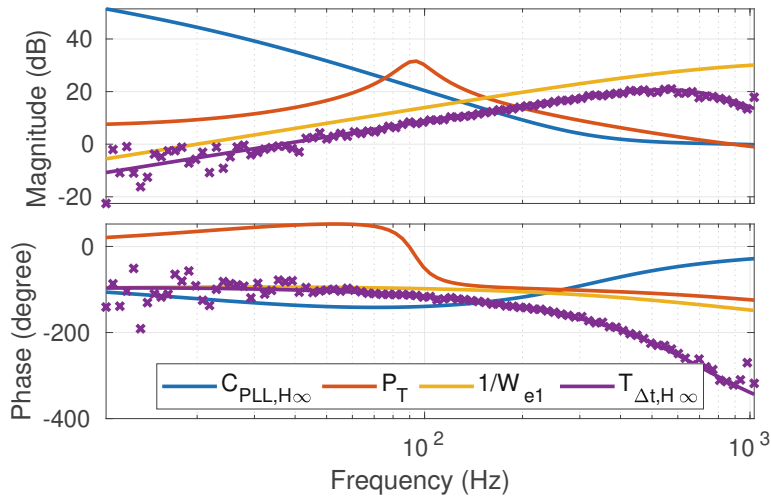


Figure 3.9: Frequency response for the H_∞ controller design: controller transfer function C_{PLL,H_∞} , plant transfer function P_T and the load disturbance sensitivity function T

W_{e1} determines the shape of the load disturbance sensitivity function, which is visible in Figure 3.9. Similar to the other controller designs Figure 3.9 shows the measured data to verify that the implementation was successful.

3.3 Implementation

This section discusses the implementation details of the digital controller and its hardware implementation. For this research, a custom board built upon the Xilinx Zynq 7000 system-on-chip series is used, which includes an FPGA and a powerful dual-core ARM Cortex-A9 processor. Field programmable gate arrays (FPGAs) provide a great development tool for research compared to ASIC, because of their performance and flexibility, enabling quick prototyping of digital designs. The combination of programmable

Table 3.1: Example for the DCO counting process for a slice time of 2.5 clock cycles

c_{ts}	c_s	next c_{ts}	change slice
0.00	0	1.00	no
1.00	0	2.00	no
2.00	0	3.00	yes
0.50	1	1.50	no
1.50	1	2.50	yes
0.00	2	1.00	no
1.00	2	2.00	no
2.00	2	3.00	yes
0.50	3	1.50	no
1.50	3	2.50	yes
0.00	0	1.00	no
...

logic with a microcontroller allows the implementation of time-critical parts in hardware, while less time-critical parts can be implemented on the microcontroller, maximizing the performance versus development effort tradeoff.

3.3.1 DCO and Scheduler

The DCO is responsible for the MEMS mirror driving, the starting of the controller calculations, and the laser triggering. The DCO splits the input period into $2^{N_{\text{slices}}}$ equal slices. The slice computation is based on fixed point counters. The input period \hat{T} is given in clock cycles in fixed point Qn.m format, where n represents the number of integer bits of the period, and m is the number of fractional bits. The fractional part allows to set the period more accurately than one clock cycle, which is necessary for some MEMS mirrors with a high Q factor. Needless to say, a temporal resolution of less than a clock period cannot be achieved by an output of any synchronous design. However, the fractional part is used in a manner that the input period is reached on average.

Before the counting process starts, the period \hat{T} is divided by the number of slices, and the clock cycles per slice T_{slice} is obtained. Normally, the division is very complex in hardware but since the number of slices is a power of two, the division can be implemented by bit-shift. To avoid losing any precision only the interpretation of the fixed point format is changed from Qn.m to Qa.b, where $a = n - N_{\text{slices}}$ and $b = m + N_{\text{slices}}$. Then, at each clock cycle, 1 is added to the current time stamp c_{ts} . If the timestamp is greater or equal to the slice duration T_{slice} , then T_{slice} is subtracted from the timestamp, and the current slice counter c_s is incremented by one. For better understanding a simple example with $N_{\text{slice}} = 2$, $\hat{T} = 10$ is shown in the Table 3.1 ($m = 4$, $n = 0$, $a = 2$, $b = 2$, all numbers are denoted as floating point). \hat{T} interpreted in Qa.b format is equivalent to 2.5, so the slice counter is changed every time the timestamp is greater than or equal to 2.5. Table 3.1 shows that the total period is 10 clock cycles, and the slice duration varies from 2 to 3 clock cycles, averaging

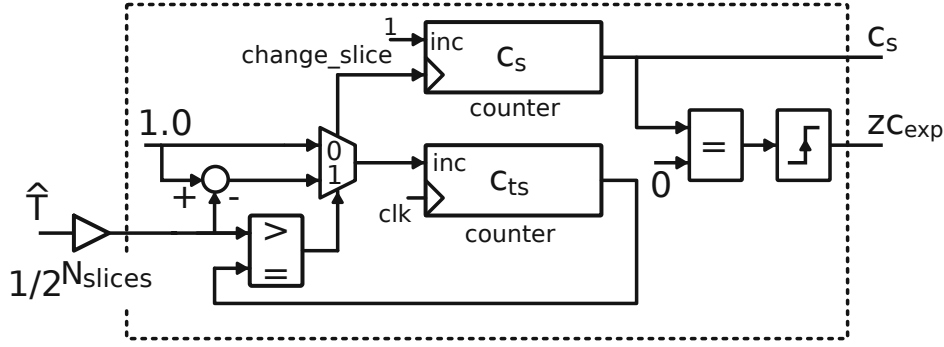


Figure 3.10: Schematic of the DCO based on the averaging principle. The DCO only contains two registers: one slice register and the counter value. The DCO receives the DCO period $T_{\text{slice}} = \frac{T}{2^{N_{\text{slices}}}}$ and outputs the slice as well as a flag when slice 0 is reached representing the expected zero-crossing.

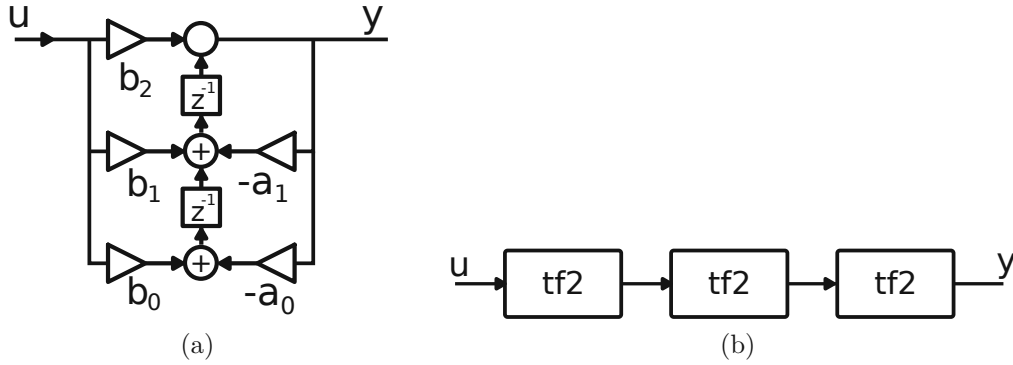


Figure 3.11: (a) Transposed-direct-form-II implementation for a 2nd order system (b) 6th order transfer function by 3 2nd order sections chained together.

out to 2.5 clock cycles. The high Q-factor of the MEMS mirror allows this without disturbing the MEMS mirror's motion. This averaging principle is the optimum that can be achieved with a synchronous design, more accurate driving signals can only be achieved with asynchronous designs [19]. Figure 3.10 shows a block diagram of the DCO implementation, consisting of the counter and slice registers. Furthermore, the DCO outputs the rising edge at the beginning of slice 0, which represents the beginning of the new DCO period and is used as the expected zero-crossing signal z_{cexp} .

The scheduler is very simple. The driving voltage is defined by the two switching points \hat{s}_{on} and \hat{s}_{off} . The scheduler consists of a counter, which is reset at every expected zero-crossing given by the DCO. Then the scheduler switches on the driving voltage if the counter value reaches \hat{s}_{on} , and off if the counter value reaches \hat{s}_{off} .

3.3.2 Digital Controller

The controller is implemented with a discrete transfer in transposed-direct-form-II, operating with a fixed point number format [48]. Figure 3.11 (a) shows the block diagram of the 2nd-order discrete-time system in transposed-direct-form-II. A general

2nd-order system in z-domain is given by

$$G(z) = \frac{y(z)}{u(z)} = \frac{b_2 z^2 + b_1 z + b_0}{z^2 + a_1 z + a_0}, \quad (3.40)$$

where $u(z)$ is the input in z-domain, $y(z)$ is the output in z-domain and b_2 , b_1 and b_0 , a_1 and a_0 are constant real parameters given in Q8.24 format. The inverse z-transformation results in

$$\begin{aligned} (z^2 + a_1 z + a_0)y(z) &= (b_2 z^2 + b_1 z + b_0)u(z) \\ y_{n+2} + a_1 y_{n+1} + a_0 y_n &= b_2 u_{n+2} + b_1 u_{n+1} + b_0 u_n \\ y_{n+2} &= -a_1 y_{n+1} - a_0 y_n + b_2 u_{n+2} + b_1 u_{n+1} + b_0 u_n \end{aligned} \quad (3.41)$$

Note that Figure 3.11 (a) implements Equation (3.41). A 6th-order transfer function could be implemented by extending the structure in Figure 3.11 but research has shown that it is numerically more stable to implement it by chaining three 2nd-order sections, as illustrated in Figure 3.11 (b) [53].

A new controller output value does not need to be calculated every clock cycle, but only once per MEMS mirror half-period. Therefore, implementing the transfer function as shown in Figure 3.11 (a) is not resource-efficient, because it uses 5 multipliers. Each 2nd order transfer function block is implemented with only one multiplier and multiplexed inputs to save FPGA resources. The instructions are then

- 1: $y = b_2 u + r_0$
- 2: $r_0 = b_1 u + r_1$
- 3: $r_0 = -a_1 y + r_0$
- 4: $r_1 = b_0 u$
- 5: $r_1 = -a_0 y + r_1$

The result is already valid after the first instruction, and instructions 2 to 4 only update the values of the two internal registers. In the case of the chained 6th-order transfer function the start signals need to be passed from one 2nd-order section to the succeeding one. The total delay will be 3 clock cycles, which is still sufficiently low.

3.3.3 Phase Detector

The phase detector measures the time difference in clock cycles between two signal edges A and B. If the rising edge on input A happens before the rising edge on input B, then the result is negative, and otherwise, the result is positive.

The phase detector consists of two simple counters c_{A2B} and c_{B2A} , counting the time difference from A to B, and from B to A, respectively. The output of the phase detector is the absolute minimum between these two values, given by

$$\Delta t = \begin{cases} -c_{A2B}, & c_{A2B} < c_{B2A} \\ c_{B2A}, & c_{A2B} \geq c_{B2A} \end{cases} \quad (3.42)$$

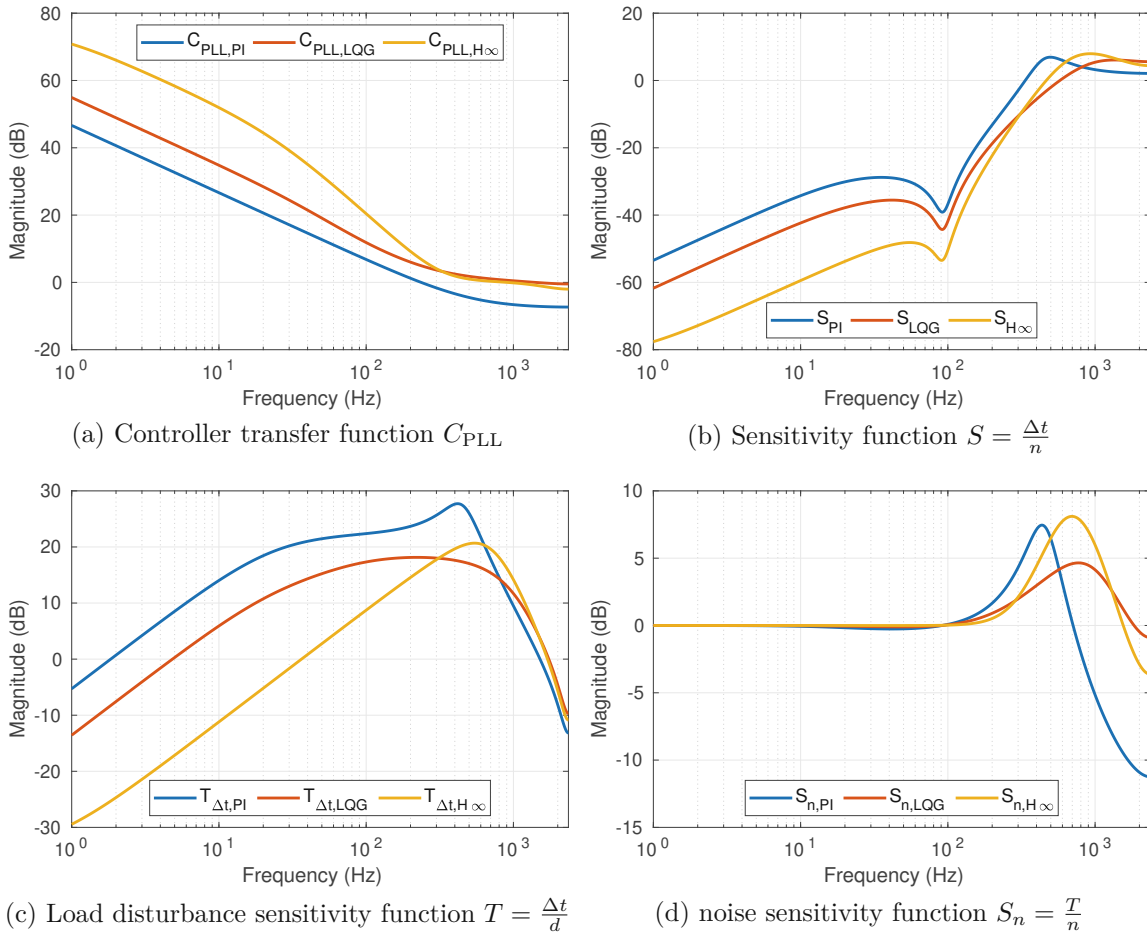


Figure 3.12: Comparison of the controllers by (a) controller transfer function, (b) sensitivity function (c) load disturbance sensitivity function and (d) noise sensitivity function.

3.4 Evaluation

The controller can be compared by their capability to reject the external disturbance and the measurement noise. Figure 3.12 shows the frequency responses of all controllers. The H_∞ controller shows the highest gain in the low-frequency range, therefore achieves the best rejection of disturbances in the low-frequency range, as shown in Figure 3.12 (a+c). However, to avoid the amplification of high-frequency noise, the controller gain at high frequencies is slightly lower than the gain of the LQG controller. In a direct comparison therefore the LQG controller rejects the disturbance above 300 Hz better than the H_∞ controller. The PI controller has the lowest gains, therefore its load disturbance sensitivity function has the highest gains, meaning the disturbances are not rejected well. At the same time, the sensitivity function already shows that noise has more influence on the output than for LQG control of H_∞ control. Figure 3.12 (d) shows the noise sensitivity functions $S_n = \frac{T}{n} = \frac{C_{PLL}}{1+C_{PLL}P_T}$. The PI controller shows the lowest influence of high-frequency noise on the controller output.

To evaluate if the model-based controllers improve the performance the laser pointing

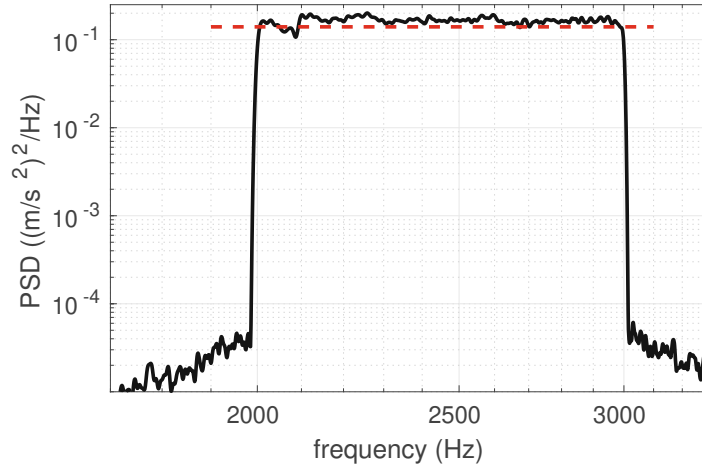


Figure 3.13: Vibration profile used to evaluate the pointing uncertainty of the PLL. The shaker applies a broadband vibration between 2-3 kHz of $0.14 \frac{(m/s^2)^2}{Hz}$ to the mirror.

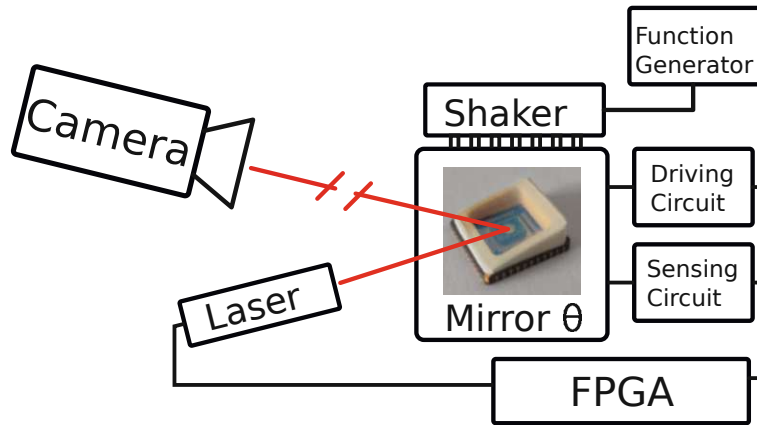


Figure 3.14: Experimental setup of the pointing stability measurement

uncertainty under vibration each controller was measured. The FPGA switches the laser on at a certain slice and projects a single pixel to the screen. A camera is placed where the pixel is generated. The MEMS mirror is mounted to a shaker that applies a broadband vibration from 2-3 kHz and a PSD of $0.14 \frac{(m/s^2)^2}{Hz}$ to the MEMS mirror, which corresponds to the extended automotive standard [54]. Figure 3.13 shows the measured power spectral density of the vibration profile that the shaker applies to the mirror. The measurement is taken with a vibrometer and used to verify a flat power spectral density.

Figure 3.14 shows an overview of the experimental setup consisting of the pulsed laser, the MEMS mirror and controller and the camera used to evaluate the pointing error. Figure 3.15 shows the sum of 750 frames of a 25-second video of the laser spot during vibration influence. Due to the vibration applied to the MEMS mirror, its movement is disturbed, which results in a position error of the laser spot. The camera is placed 65 cm from the camera. Figure 3.16 shows the distribution of the pointing errors evaluated from the video by calculating the center of the laser point by the weighted average over

3 Single Axis MEMS Mirror Control

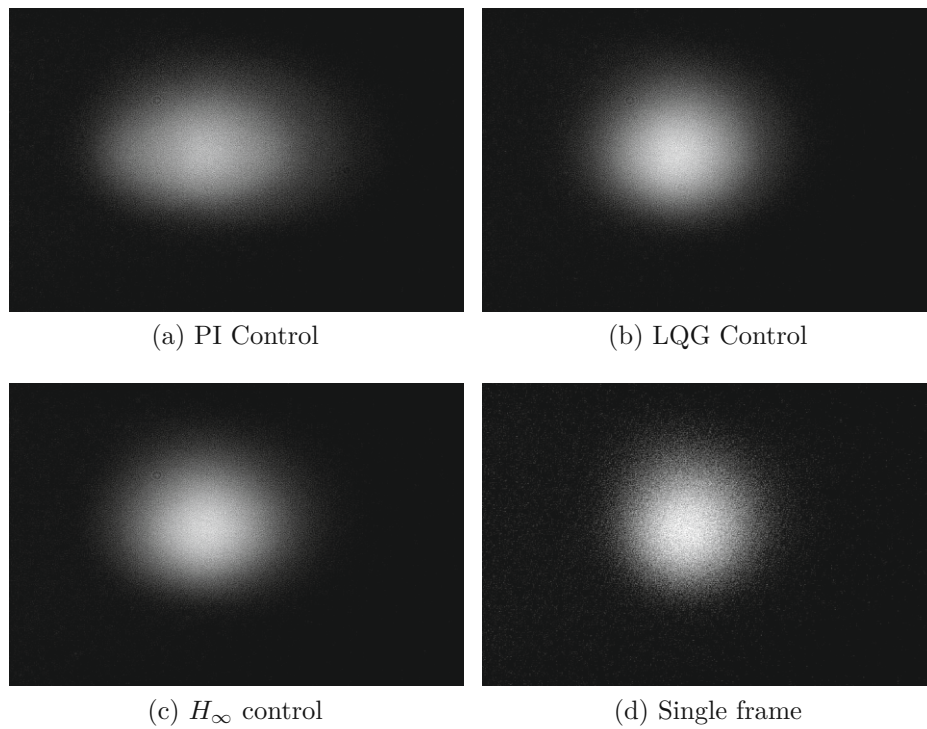


Figure 3.15: Sum of all frames of the video to evaluate the pointing error under vibration influence for (a) PI control, (b) LQG control, and (c) H_∞ control. (d) A single image of the laser spot, for comparison.

all pixel coordinates. The exposure time of the camera was set to $\frac{1}{2T}$ to capture a single pixel inside each frame. The LQG and H_∞ clearly outperform the PI controller and show an optical pointing uncertainty of around 11.8 millidegree and 12.0 millidegree, respectively, compared to the 23.1 millidegree of the PI controller.

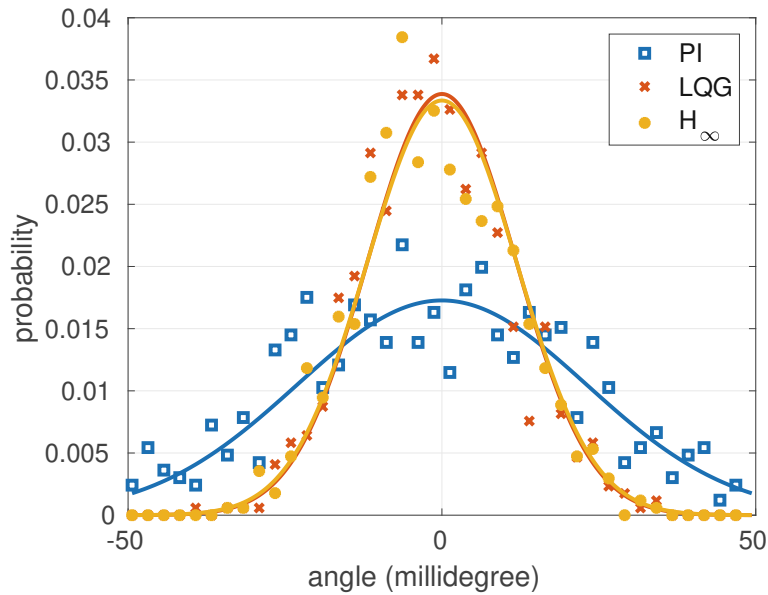


Figure 3.16: Distribution of the laser pointing error under vibration influence for different controllers. The LQG and H_∞ controller clearly outperform the PI controller. The diagram shows data point sampled from the obtained distribution, as well as a gaussian fit for each controller.

3.5 Summary

The PLL does not only control the MEMS mirror but also generates the interpolation for the laser triggering. Therefore the PLL must track the movement of the MEMS mirror as accurately as possible to achieve sharp images in a projection scenario. This chapter showed that model-based design approaches such as LQG control and H_∞ control can be used to improve the optical pointing uncertainty of the PLL by a factor of 2 compared to simple PI control. The PI controller achieved a rms deviation of the pointing error of 23.1 millidegree, the LQG controller 11.0 millidegree and the H_∞ controller 12.0 millidegree.

CHAPTER 4

Synchronization of two 1D MEMS Mirrors

Two-dimensional scanning systems use two MEMS mirrors to steer the light beam in two independent directions. This chapter describes synchronization concepts to achieve a stable Lissajous pattern in a projection system consisting of two 1D MEMS mirrors.

Figure 4.1 shows a block diagram of the experimental setup used in this section, and Figure 4.2 shows a photograph of the real lab setup. The light beam is reflected from the first MEMS mirror and travels through a system of lenses, which focus the beam onto the second MEMS mirror. The second MEMS mirror reflects the beam to the projection screen. The second MEMS mirror is mounted on a piezo shaker to emulate the disturbances that are faced in real-world applications.

Since both MEMS mirrors follow a close-to-sinusoidal trajectory, they project a Lissajous pattern to the screen. The density of the Lissajous pattern is determined by the frequency ratio between the two MEMS mirrors. To achieve a uniform Lissajous pattern, the frequency ratio has to be constant. Even short-term deviations from the frequency ratio cause permanent phase differences between the two oscillations and distortions in the Lissajous pattern. A simple Lissajous pattern can be achieved by an open-loop driving at constant frequency for both MEMS mirrors. However, for reliable operation under external vibration, a feedback control system is required.

The PLL used to control the MEMS mirror tracks the MEMS mirror oscillation period and adjusts the driving frequency to match the current oscillation period. Therefore, the frequency of the PLL-operated MEMS mirror can vary slightly, resulting in a nonuniform Lissajous pattern. Therefore, the PLL itself is not suitable for synchronizing two MEMS mirrors. The PLL controls the period T of the DCO, and s_{off} is left unconnected in Chapter 3. The s_{off} input can be used to control the frequency of the MEMS mirror to achieve a uniform Lissajous pattern.

Figure 4.3 shows the block diagram for the synchronization of two MEMS mirror. One MEMS mirror is operated as a master axis, utilizing the PLL, and the s_{off} input is left unconnected or can be used to control the amplitude. The master axis generates the necessary synchronization signals for the slave axis. The slave axis is equipped with a synchronization controller. Figure 4.4 illustrates the driving scheme of the MEMS

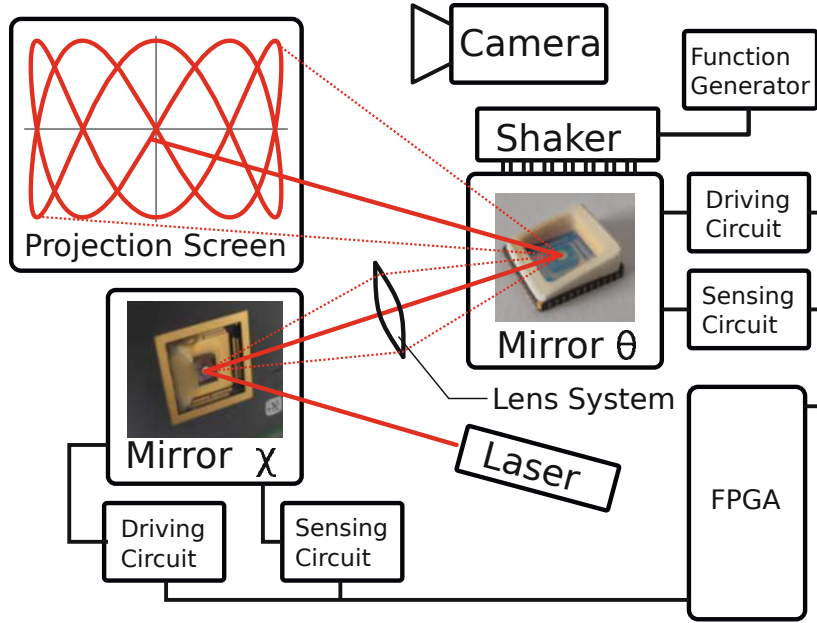


Figure 4.1: Evaluation setup, consisting of two separate MEMS mirrors, an FPGA to drive both MEMS mirrors, a shaker attached to the slave MEMS mirror, and a laser and camera to evaluate the projected Lissajous pattern.

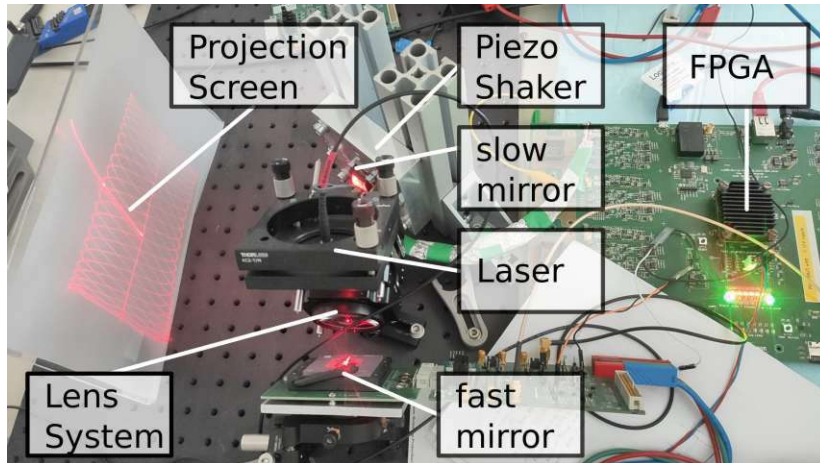


Figure 4.2: Photograph of the experimental setup. The laser beam is reflected from the fast MEMS mirror, focused by a lens system to the slow mirror, and then reflected to the projection screen, a white sheet of cardboard

mirrors. The master axis generates reference zero-crossings at time t_{ref} . These signals are produced by the reference frequency generator described in Section 4.3.2 with the correct ratio $\frac{M}{N}$ for the Lissajous pattern, which is correct if the actual zero-crossings of the slave axis occur at t_{ref} . The slave MEMS mirror synchronizes to these reference signals by adjusting the s_{off} value of the DCO, driving the MEMS mirror to a different operating point on the response curve shown in Figure 3.1. The difference between the actual zero-crossings and the reference crossings is called the synchronization error Δtr . The definition of the phase error Δt , as described in Section 3 is unchanged, i.e.

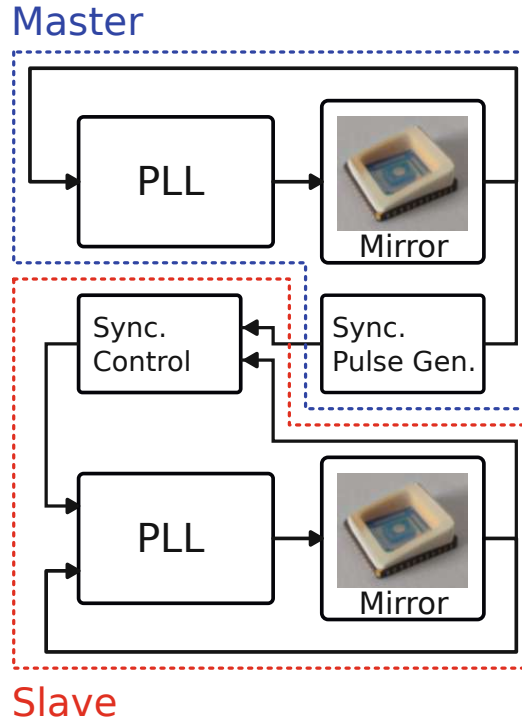


Figure 4.3: Block diagram of the master-slave synchronization concepts. The master axis generates the reference pulses for the slave. The slave axis consists of a MEMS mirror, operated by the PLL and is extended by a synchronization controller.

the phase error is the time difference between expected zero-crossing and the actual zero-crossings.

Figure 4.4 depicts the master axis having a much higher frequency than the slave axis. Utilizing the faster MEMS mirror on the master axis has several benefits. Firstly, the reference frequency for the slave axis can be generated by counting the periods of the fast axis and interpolating as required in between. Additionally, the fast MEMS mirror, having less control margin, allows for only slight frequency adjustments and exhibits slower local dynamics compared to the slow MEMS mirror, owing to its higher Q-factor. This renders the fast MEMS mirror more robust to vibration in the 2-3 kHz range, as MEMS mirrors are primarily influenced by vibrations close to their resonance frequency [32].

The master-slave structure proves advantageous in image display scenarios. The phase error of the master can be consistently kept low by adjusting the driving period, as it is arbitrary. The adjustment can be done on the FPGA without the need for energy injection into or removal from the system. A small phase error is sufficient for achieving a low pixel pointing error, as elaborated in Section 3. Conversely, the slave axis must have a small synchronization error Δtr to ensure an accurate Lissajous pattern. The phase error Δt is not critical for the slave axis but must be kept within certain limits to avoid losing the PLL to MEMS mirror lock.

Figure 4.5 visually demonstrates the impact of the synchronization error on the Lissajous

4 Synchronization of two 1D MEMS Mirrors

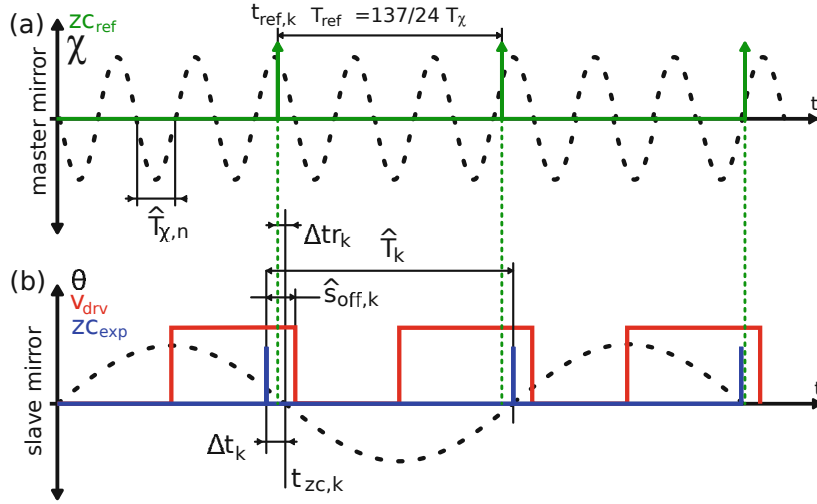


Figure 4.4: Driving and sensing definitions for the slave axis. The master axis generates the reference zero-crossings at times $t_{\text{ref},k}$, to which the slave axis attempts to synchronize. The difference between the actual zero-crossings and the reference zero-crossings is the synchronization error Δtr .

pattern. Substantial synchronization errors lead to pattern shifts that render the image unreadable, and even minor synchronization errors lead to uniformity in the image intensity. For comparison, Figure 4.6 shows the influence of a phase error on the projected image. The laser is activated with the slices, assuming alignment between the expected and actual zero-crossings. When this alignment does not occur, the laser triggering is shifted, leading to less defined transitions at the edges of the image. In other words, the laser is switched on either too late or too early, affecting the sharpness of image edges.

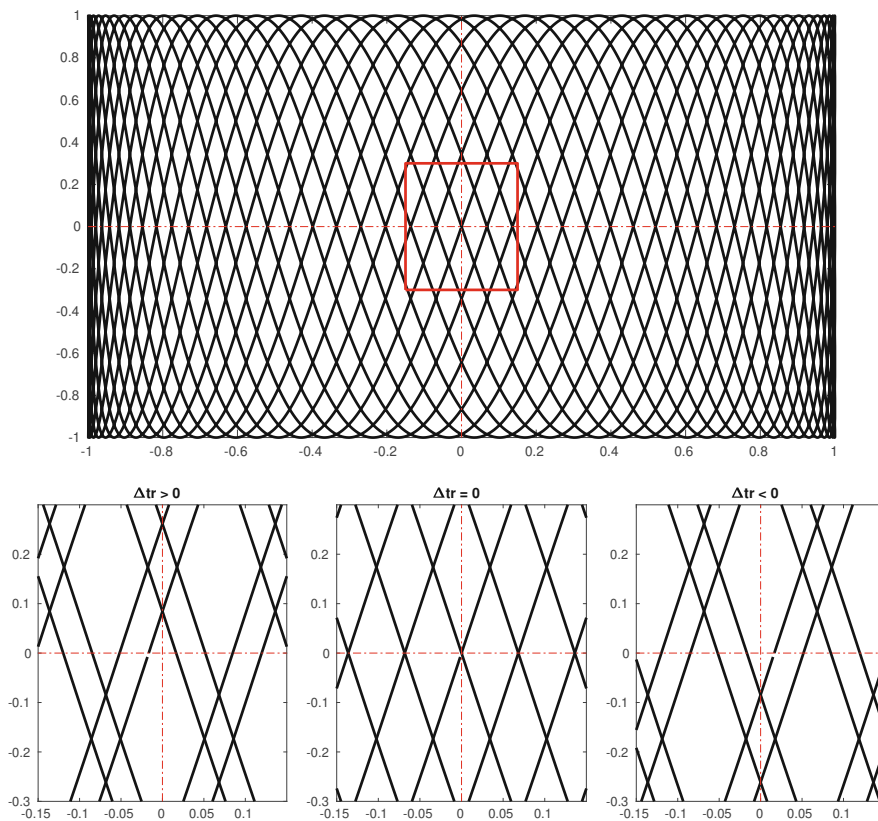


Figure 4.5: Impact of the synchronization error Δtr on the Lissajous pattern. The bottom rows shows a zoomed section of the full Lissajous pattern, with $\Delta tr > 0$ (left), $\Delta tr = 0$ (center), and $\Delta tr < 0$ (right)

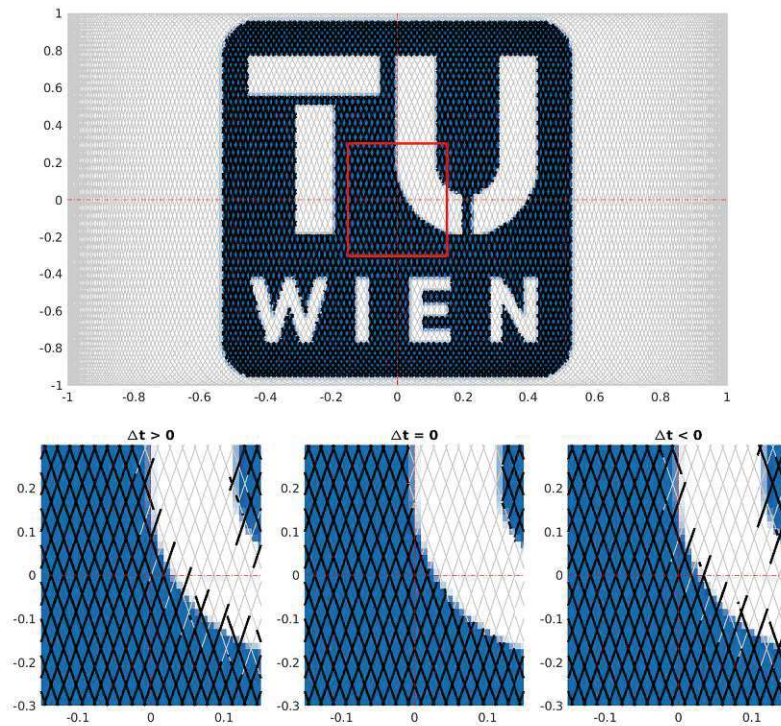


Figure 4.6: The phase error Δt of the master axis on the Lissajous pattern, when projecting an image onto the screen, leads to less defined transitions at the borders of the projected image. It's important to note that, for illustration purposes, the number of scan lines is relatively low; in practice, a much higher number is typically selected. The gray lines represent the trajectory of the MEMS mirror and the thicker black lines indicate segments of the trajectory where the laser is switched on.

4.1 Synchronization control for PLL-operated MEMS mirrors

This section extends on the synchronization concept proposed in [44] that adds an additional phase detector and synchronization controller on top of the PLL-operated MEMS mirror.

Figure 4.7 depicts the controller loop for the slave axis. The additional phase detector measured the synchronization error Δtr , corresponding to the time difference between the reference zero-crossings, obtained from the master axis, and the actual zero-crossing of the MEMS mirror of the slave axis.

4.1.1 Model Extension

Figure 4.8 (a) shows the model of the MEMS mirror system for the PLL design. The model includes the DCO, the MEMS mirror, and the phase detector. Figure 4.8 (b) shows the model used for the slave MEMS mirror. The model is an extension of the single axis MEMS mirror model by an additional phase detector that measures the synchronization error Δtr .

To derive the system matrices A_G , B_G , C_G of the extended model first the actual MEMS mirror half-period $T_{m,k}$ at time step k is given by

$$T_{m,k} = T_k - (\Delta t_{k+1} - \Delta t_k), \quad (4.1)$$

where T_k is the DCO period and Δt_k is the phase error. The negative sign originates from the definition of the phase error $t_{zc,k} - t_{zc,exp,k} = \Delta t_k$. The z-transformation of (4.1) is then

$$T_m = T - (z - 1)\Delta t. \quad (4.2)$$

The phase detector of the synchronization error can be modeled as integrator with input $T - T_{ref}$, formally

$$\Delta tr_{k+1} = \Delta tr_k + T_{m,k} - T_{ref,k}. \quad (4.3)$$

The z-transformation of (4.3) calculates to

$$\Delta tr = \frac{T_m - T_{ref}}{z - 1}. \quad (4.4)$$

Substituting (4.2) into (4.4) gives

$$\Delta tr = \frac{T - T_{ref}}{z - 1} - \Delta t. \quad (4.5)$$

With this knowledge, a discrete model for the extended system can be written in

4 Synchronization of two 1D MEMS Mirrors

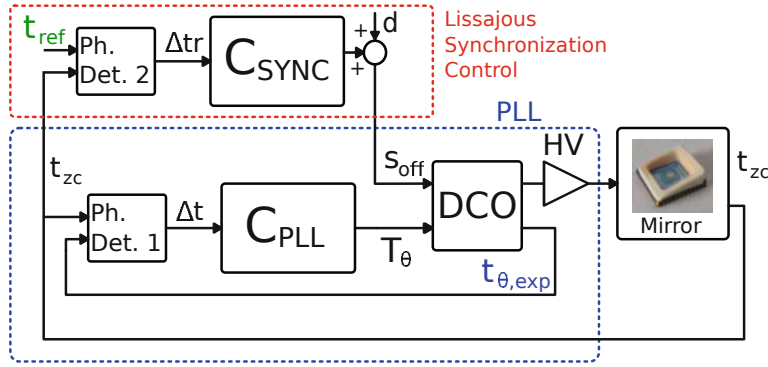


Figure 4.7: Slave axis controller loop with two different controllers to synchronize to the master MEMS mirror. An additional phase detector measures the synchronization error Δtr and uses s_{off} to control it.

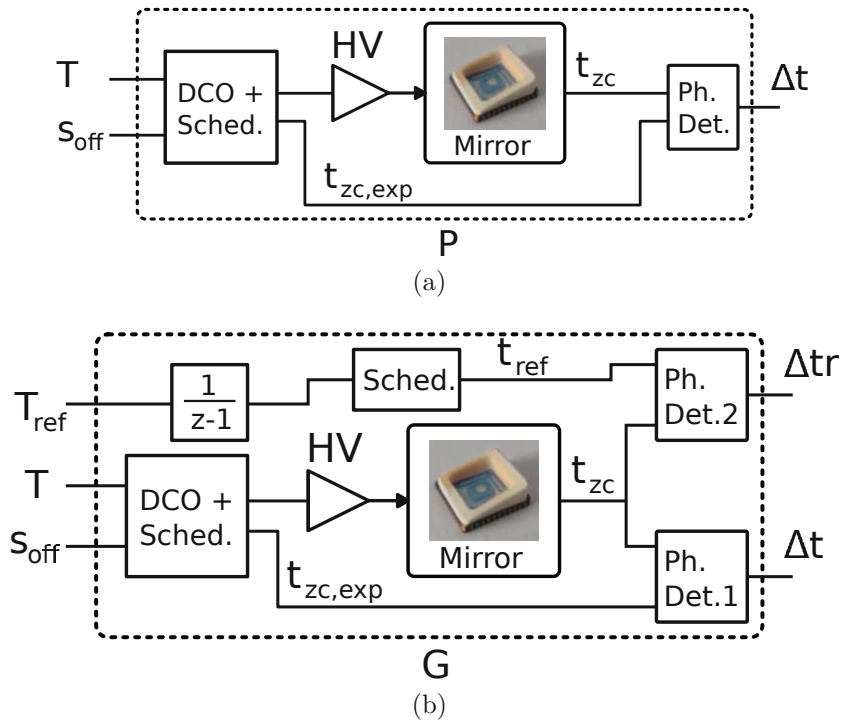


Figure 4.8: (a) The model used for the PLL design includes the DCO, the MEMS mirror and the phase detector (b) The model for the slave axis includes an additional phase detector that measures the difference between reference zero-crossings and actual zero-crossings.

state-space representation as

$$\begin{aligned}
 x_{k+1} &= \overbrace{\begin{bmatrix} A_P & 0 \\ 0 & 0 & 1 \end{bmatrix}}^{A_G} x_k + \overbrace{\begin{bmatrix} B_P & 0 \\ 1 & 0 & -1 \end{bmatrix}}^{B_G} \begin{bmatrix} T_k \\ s_{off,k} \\ T_{ref,k} \end{bmatrix} \\
 \begin{bmatrix} \Delta t \\ \Delta tr \end{bmatrix} &= \overbrace{\begin{bmatrix} C_P & 0 \\ -C_P & 1 \end{bmatrix}}^{C_G} x_k,
 \end{aligned} \tag{4.6}$$

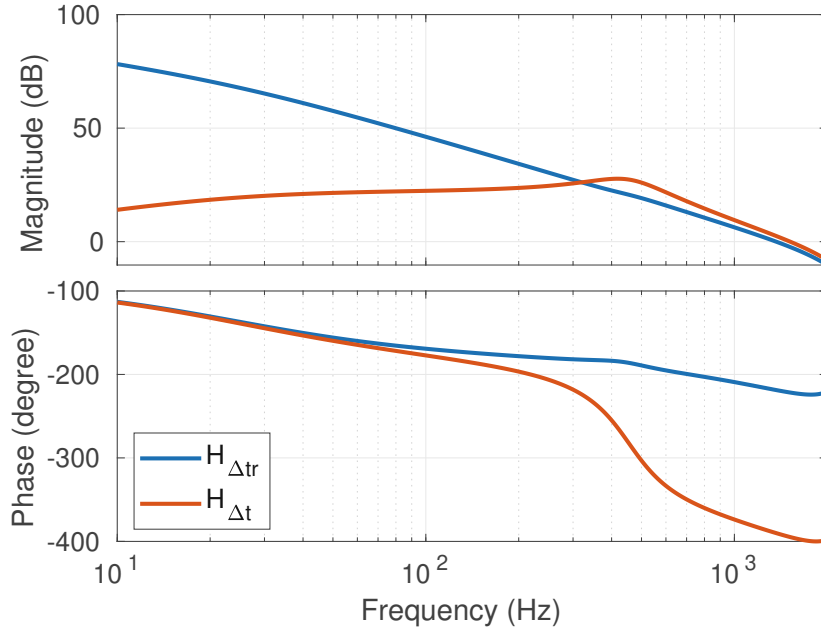


Figure 4.9: closed-loop transfer function $G_{s,\Delta t}$ from s_{off} to the phase error Δt and $G_{s,\Delta tr}$ from s_{off} to the synchronization error Δtr for the system running with the PLL but without synchronization controller. While for constant inputs Δt converges to zero, Δtr shows integrating behavior.

where A_P , B_P , C_P are given in (3.21). Not taking into account the reference period input T_{ref} the system can be written down as a transfer function matrix

$$\begin{bmatrix} \Delta t \\ \Delta tr \end{bmatrix} = \begin{bmatrix} G_{T,\Delta t} & G_{s,\Delta t} \\ G_{T,\Delta tr} & G_{s,\Delta tr} \end{bmatrix} \begin{bmatrix} T \\ s_{\text{off}} \end{bmatrix}. \quad (4.7)$$

4.1.2 PID-based Synchronization Controller Design

Let H denote the PLL-controlled extended system of the MEMS mirror G . By using (4.7) H can be written as a transfer function matrix

$$\begin{bmatrix} \Delta t \\ \Delta tr \end{bmatrix} = \begin{bmatrix} H_{\Delta t} \\ H_{\Delta tr} \end{bmatrix} s_{\text{off}} = \begin{bmatrix} \frac{G_{s,\Delta t}}{1+G_{T,\Delta t}C_{\text{PLL}}} \\ G_{s,\Delta tr} - \frac{G_{s,\Delta t}G_{T,\Delta tr}C_{\text{PLL}}}{1+G_{T,\Delta t}C_{\text{PLL}}} \end{bmatrix} s_{\text{off}}. \quad (4.8)$$

Figure 4.9 illustrates the transfer function $H_{\Delta t}$ and $H_{\Delta tr}$ of the PLL-operated MEMS mirror. The transfer function $H_{\Delta t}$ has a slope of 20 dB at low frequencies, indicating that the phase error Δt converges to 0 for constant inputs. On the other hand, the transfer function $H_{\Delta tr}$ displays integrating behavior. This implies that the PLL alone is not adequate to achieve synchronization, necessitating an additional controller to regulate Δtr . Due to the low phase margin of $H_{\Delta tr}$ in the desired crossover region of more than 100 Hz a PI controller is insufficient, and a PID controller becomes necessary. This PID controller can be designed using the rule of thumb [55] in the continuous domain and then be converted to the discrete domain.

4 Synchronization of two 1D MEMS Mirrors

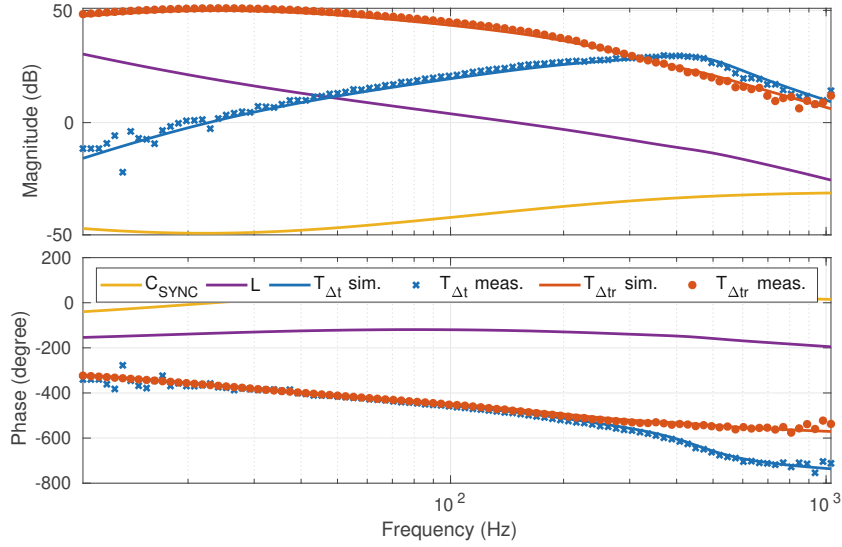


Figure 4.10: Simulated and measured transfer functions from d to Δt and Δtr by applying an emulated disturbance additively to the s_{off} input

The continuous PID controller with crossover frequency ω_c is given by

$$C_{SYNC}(s) = g \frac{(1 + \frac{s}{0.1\omega_c})(1 + \frac{s}{0.3\omega_c})}{s(1 + \frac{s}{3\omega_c})}, \quad (4.9)$$

where ω_c is the desired crossover frequency and g is the controller gain. The gain g can be determined in the second step by choosing g such that $G(s)P(s)|_{s=i\omega_c} = 1$. Figure 4.10 (b) displays the transfer function of a PID controller with a crossover frequency of 127 Hz and the resulting closed-loop transfer functions from disturbance to outputs Δt and Δtr . They are measured by introducing a simulated disturbance to the system. To emulate the disturbance a sine wave generator is synthesized on the FPGA, adding a disturbance to the s_{off} input. The transfer functions $T_{\Delta t}$ and $T_{\Delta tr}$ from disturbance to Δt and Δtr can be calculated to

$$T_{\Delta tr} = \frac{\Delta tr}{d} = \frac{H_{\Delta tr}}{1 + C_{SYNC}H_{\Delta tr}}, \quad (4.10)$$

and

$$\begin{aligned} T_{\Delta t} &= \frac{\Delta t}{d} = H_{\Delta t}(1 - C_{SYNC}(\frac{\Delta tr}{d})) \\ &= H_{\Delta t}(1 - \frac{C_{SYNC}H_{\Delta tr}}{1 + C_{SYNC}H_{\Delta tr}}). \end{aligned} \quad (4.11)$$

The calculation of the transfer functions $T_{\Delta t}$ and $T_{\Delta tr}$ shows good agreement with the measurement data in Figure 4.10 (b), proving that the extended model is correct and the implementation of the PID controller is successful.

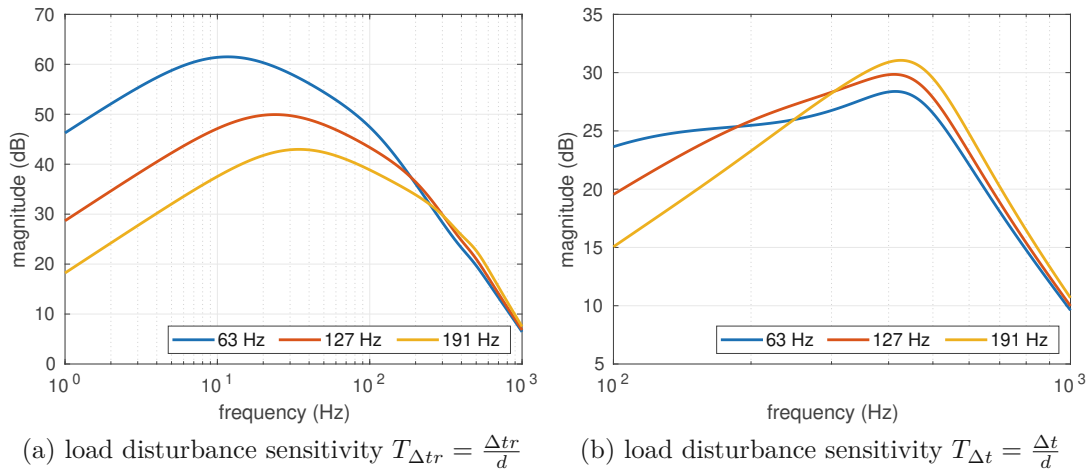


Figure 4.11: Load disturbance sensitivity of the synchronization error Δtr and phase error Δt for three different synchronization controllers with crossover frequencies of 63 Hz, 127 Hz and 191 Hz.

4.1.3 Analysis of Synchronization Controller

The synchronization control of the slave consists of two controllers, which operate with distinct objectives: The PLL adjusts the driving frequency to align with the MEMS mirror's oscillation frequency, while the synchronization controller forces the MEMS mirror to run at the target frequency by adjusting s_{off} . This implies that increasing the gains of the synchronization controller forces the MEMS mirror to run at a specific frequency, thereby compromising the performance of the PLL. Figure 4.11 (a) shows the closed-loop transfer function $T_{\Delta tr}$ from disturbance d to synchronization error Δtr for three PID-based synchronization controllers with crossover frequencies of 63 Hz, 127 Hz and, 191 Hz. A higher crossover frequency results in a lower amplification of the disturbance, indicating that higher crossover frequencies offer better disturbance rejection. Figure 4.11 (b) presents the closed-loop transfer function $T_{\Delta t}$ from d to phase error Δt for the same three synchronization controllers. The worst-case amplification of the disturbance increases with increasing synchronization controller gains. Notably, even though the PLL controller remains unchanged, the synchronization controller influences the performance of the PLL. This demonstrates that the controllers mutually affect each other, and the optimal controller design is always a tradeoff between minimizing Δt or Δtr . The same behavior is evident in the real setup under vibrations. Figure 4.12 depicts the measured RMS value of the synchronization error Δtr and phase error Δt for various synchronization controller crossover frequencies from 63 Hz to 320 Hz. The observation is that elevated synchronization controller gains lead to reduced synchronization errors, but at the same time imply higher phase errors, highlighting the inherent competition between the two controllers.

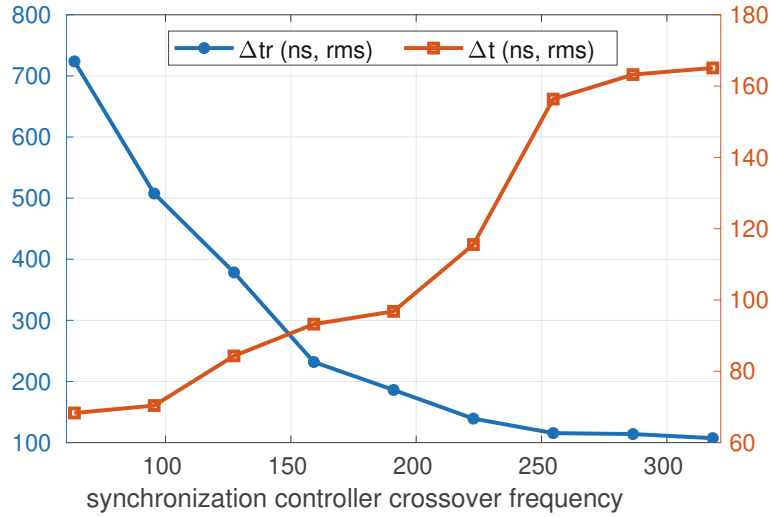


Figure 4.12: Measured synchronization error Δtr and phase error Δt for different synchronization controller crossover frequencies. It can be observed that increased gains lead to lower synchronization errors, but higher phase errors.

4.2 Direct Correction PLL

The Direct Correction PLL (DCPLL) is an adaptation of the typical PLL that enables the PLL to maintain a fixed frequency. This eliminates the need for an additional synchronization controller and thereby also removes the competition that occurs between PLL and synchronization controller, as described in Section 4.1.3.

4.2.1 General Idea

In the master-slave structure, both MEMS mirrors are operated by a PLL, achieving a small phase error Δt . However, a small phase error Δt is insufficient, but a small synchronization error Δtr is also necessary. The PLL cannot regulate the synchronization error Δtr , because it adjusts the driving frequency to match the oscillating frequency of the mirror. Therefore, an additional synchronization controller is typically added to regulate the synchronization error, which is given by the time difference between reference zero-crossings and actual zero-crossings as $\Delta tr = t_{\text{ref}} - t_{\text{zc}}$, to zero.

Ideally, the actual zero-crossings, the expected zero-crossings, and the reference zero-crossings should be the same. The main concept of the DCPLL is to fix the expected zero-crossings to the reference zero-crossing, forcing the mirror to run at the frequency determined by the master Axis. Furthermore, the phase error Δt equals the synchronization error Δtr . This has significant benefits in terms of controller design. Instead of two controllers competing with each other, only a single controller is employed on the slave axis. Additionally, there is only one output that needs regulation. Figure 4.13 illustrates the block diagram for the slave MEMS mirror DCPLL. The controller solely adjusts s_{off} of the scheduler. The DCO period is determined by the direct compensation unit and is fixed to the reference period.

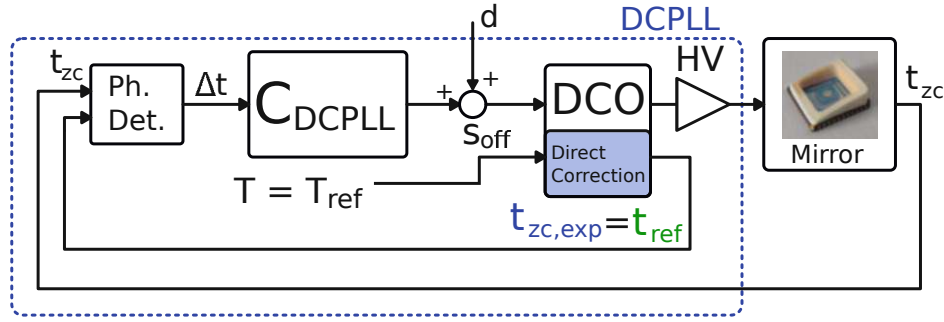


Figure 4.13: Direct Correction PLL. The phase and period is fixed at the target. The s_{off} input is used to compensate for disturbances.

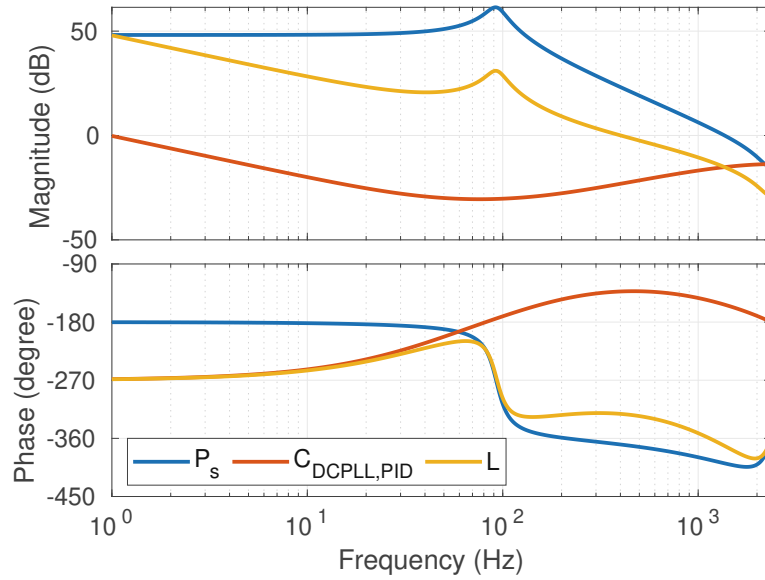


Figure 4.14: DCPLL PID controller frequency responses, showing the controller transfer function $C_{DCPLL,PID}$, the open-loop function L for the PID controller and the plant transfer function P_s .

4.2.2 Controller Design

PI and PID Control

A PID controller can be designed for the DCPLL based on the identified local dynamics of the MEMS mirror, performed in Chapter 3. Figure 4.14 shows the controller transfer functions $C_{DCPLL,PID}$ and the open-loop transfer function $L = C_{DCPLL,PID}P_s$ of the plant P_s . Notably, the phase margin of the plant P_s does not allow bandwidths higher than the resonance at around 100 Hz without a phase lead, therefore PI control does not offer a sufficiently high bandwidth to reject the noise, necessitating the use of a D gain that introduces a phase lead in the crossover region. The continuous PID controller was designed by the rule of thumb [55] as in (4.9). The PID controller achieves a crossover frequency of 400 Hz and a phase margin 52.9°.

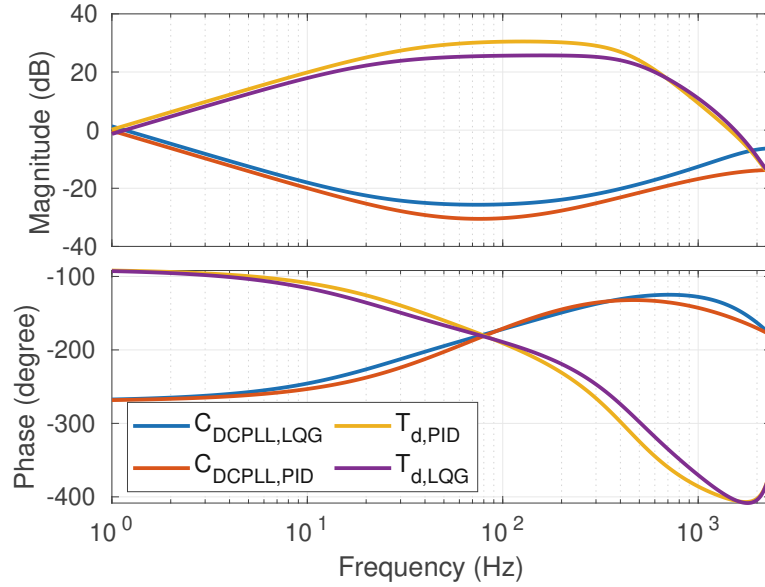


Figure 4.15: Transfer function of the LQG controller C_{LQG} and the closed-loop transfer function $T_{d,LQG}$ from a disturbance on s_{off} to Δt for the LQG controller. For comparison also the PID controller $C_{DCPLL,PID}$ of Section 4.2.2 and its resulting disturbance rejection transfer function $T_{d,PID}$ is drawn.

LQG Control

The LQG controller design approach in Section 3.2.2 is used for the DCPLL. The design approach follows the typical steps: first, the system is extended by an integrator and the LQR is designed. Then, the Kalman filter is designed and finally the Kalman filter and the LQR are combined to the LQG controller.

Linear Quadratic Regulator. After the system is extended by an integrator to ensure convergence at the operating point the state feedback controller is designed. The weighting matrix of the states is selected to $Q = \text{diag} \begin{bmatrix} 1 & 0.1 & 0.001 \end{bmatrix}$ for the system

$$\begin{aligned} A_{P,\text{ext}} &= \begin{bmatrix} A_P & 0 \\ C_P & 1 \end{bmatrix} \\ B_{P,\text{ext}} &= \begin{bmatrix} B_{P,2} \\ 0 \end{bmatrix}, \end{aligned} \quad (4.12)$$

The controller output weighting constant is $R = 1$.

Kalman Filter. The state is estimated by a Kalman Filter. Because the controller is always started after a measurement is taken, the Kalman filter is implemented with the *current* design, as derived in Section 3.2.2 and given in (3.34). The covariance of the state Q_n and covariance of the noise R_n have been chosen experimentally to 1 and 100.

LQG. The Kalman Filter combined with the LQR results in a combined state feedback controller that can be applied to the system. The full controller matrices are derived in (3.38). Figure 4.15 shows the controller transfer function of the LQG controller

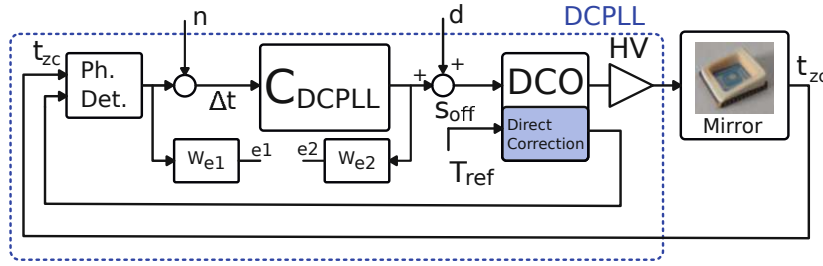


Figure 4.16: Block diagram of the DCPLL with a noise input n and disturbance input d , as well as weighting function W_{e1} and controller output weighting function W_{e2} .

$C_{\text{DCPLL,LQG}}$ compared to the PID controller $C_{\text{DCPLL,PID}}$ and the closed-loop transfer functions $T_{\text{d,LQG}}$ and $T_{\text{d,PID}}$ from disturbance d acting additively on s_{off} to Δt . The gains of the LQG controller are higher and the magnitude of the load disturbance sensitivity is lower. This means, that the LQG controller allows superior vibration rejection.

H_∞ Control

The H_∞ loop shaping approach is also used to design a DCPLL controller. Figure 4.16 illustrates the schematic of the DCPLL extended by a disturbance input n acting on the output Δt , representing the measurement noise of the phase detector, and a disturbance input d acting on s_{off} , representing the external vibration. Additionally, weighting functions W_{e1} and W_{e2} are applied to the phase error Δt and the controller output. Similar to the single axis controller in Section 3.2.3, Figure 4.16 is represented in the H_∞ framework, and a controller that minimizes the H_∞ norm can be computed. Due to the additional noise input, there is no need to penalize high-frequency controller action, allowing for the selection of a constant controller output weighting function. Figure 4.17 (a) shows the sensitivity weighting functions W_{e1} and controller output weighting functions W_{e2} employed in the H_∞ controller design. Figure 4.17 (b) presents the frequency response of the H_∞ controller transfer function $C_{\text{DCPLL},H_\infty}$ and load disturbance sensitivity T_∞ from d to Δt and the inverse of the sensitivity weighting function $\frac{1}{W_{e1}}$ corresponding to the target sensitivity. For comparison, the transfer functions of the PID controller are also shown. The H_∞ controller achieves a lower magnitude of the load disturbance sensitivity function in the lower frequency region of up to around 300 Hz, but a slightly higher magnitude in the high frequency region.

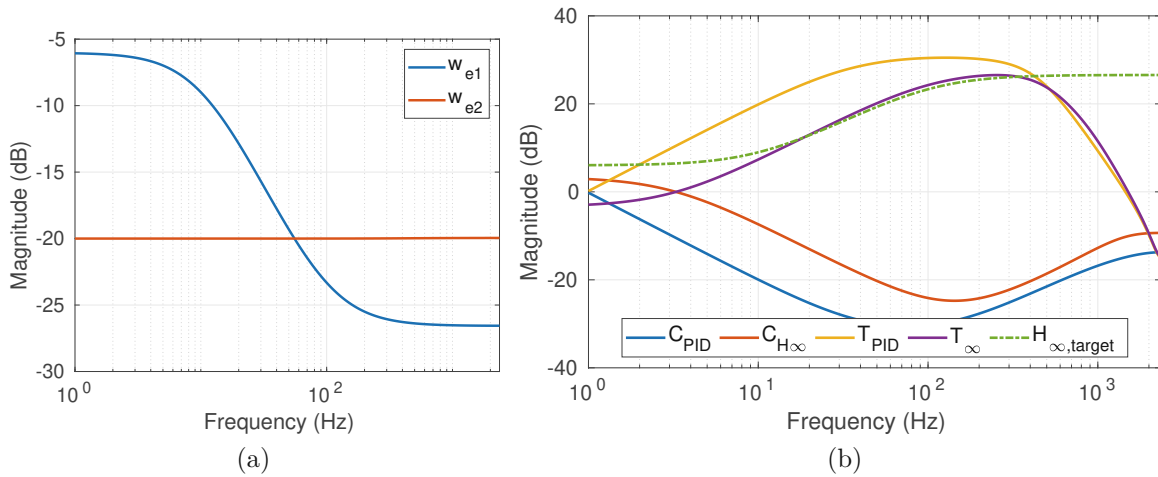


Figure 4.17: (a) Sensitivity weighting functions W_{e1} and controller output weighing functions W_{e2} used for the H_{∞} controller design (b) Frequency responses of the H_{∞} controller transfer function $C_{DCPLL,H\infty}$ and the load disturbance sensitivity function T_{∞} from d to Δt and the inverse of the sensitivity weighting function $\frac{1}{W_{e1}}$ corresponding to the target sensitivity. For comparison, the controller transfer function and the closed-loop disturbance rejection transfer function for the PID controller are also shown.

4.3 Extension of the Implementation

4.3.1 Configurable MIMO Controller

The controllers developed in this chapter are more complex than the single-axis PLL implemented in Chapter 3. Additionally, on the slave axis, there is not a single controller that needs to be implemented, but multiple ones that control different inputs of the MEMS mirror. Therefore, a configurable multiple-input multiple-output (MIMO) controller is designed. This approach enables the expression of different controller structures by modifying configuration bits during operation, providing flexibility and efficiency in the evaluation and experimentation process. Furthermore, this circumvents the time-consuming task of resynthesizing the FPGA bitstream if the structure or parameters need to be modified and allows an on-the-fly switching of the controllers to compare their performance. Figure 4.18 shows a schematic of the controller loop. The configurable MIMO controller is equipped with multiple inputs connected to distinct sensing units. First, the phase error Δt is measured as the difference between zero-crossings and expected zero-crossings. Second, for synchronization of two MEMS mirrors the phase difference between the two MEMS mirrors, i.e. the synchronization error Δtr , is given by the difference between reference zero-crossings and real zero-crossings. The amplitude is sensed by an additional comparator, generating pulses at a precise angle of the MEMS mirror. The amplitude error Δta is derived as the time difference between these pulses and target pulses corresponding to a certain amplitude. To facilitate frequency control and feedforward structure, both the reference period T_{ref} and the actual period T_m are measured and available as input to the configurable

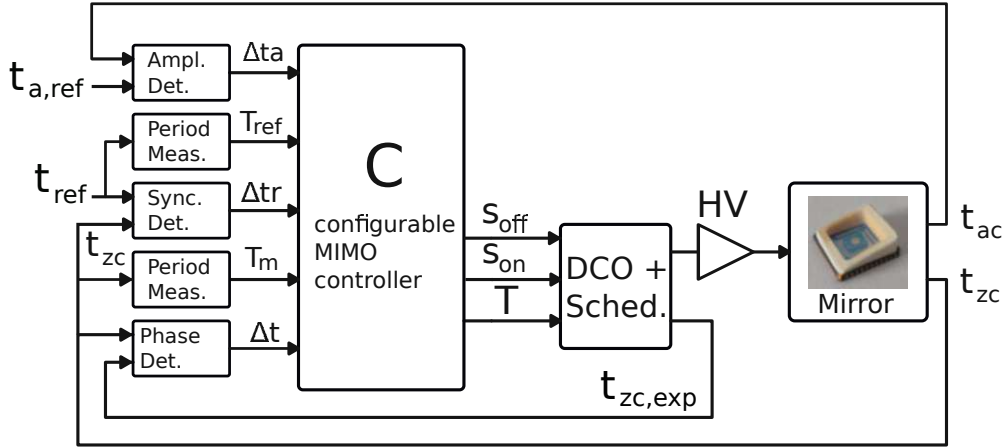


Figure 4.18: Schematic of the control loop consisting of the implemented controller and the MEMS mirror. The MIMO has multiple inputs, which are detected by distinct modules, and multiple outputs that control the DCO and the scheduler.

MIMO controller. The controller outputs the period \hat{T} for the DCO, the switching points \hat{s}_{off} and \hat{s}_{on} for the scheduler.

Figure 4.19 shows an overview of the implemented configurable controller structure. The controller consists of 6 transfer function modules. Four of them are simple 2nd-order systems, and 2 of them are 6th-order systems. The two internal registers `ireg0` and `ireg1` allow the implementation of nested controller structure to further increase the versatility of the design. The implementation of the transfer functions is explained in Section 3.3.2.

Each controller has a configurable input value, switched by the `inmux` modules. The input value can either be the phase error Δt , the synchronization error Δtr , the value of the internal register `ireg0` or `ireg1`, the actual period T_m , the target period T_{ref} , or the amplitude error Δta . The configuration input therefore switches to one of these 7 choices and has therefore 3 bits.

To efficiently realize feed-forward structures additional `outmux` modules are added to the controller structure. It allows the controller output to be modified with an addition or subtraction. The possible choices are 0 i.e. to disable this module, the open-loop period T_{ol} , the open-loop $s_{\text{off,ol}}$, or the target period T_{ref} . T_{ref} is determined by the master period by multiplying with the Lissajous ratio $\frac{M}{N}$, or can be internally generated, for synchronizing to a self-generated reference instead of the master frequency. This self-generated reference frequency allows the evaluation of slave-slave synchronization concepts. Each input value can be subtracted instead of added by changing the sign bit.

Last but not least the outputs of the controllers need to be transferred to the final outputs. This is done by the `addmux` units. The `addmux` units have 4 input bits which enable the addition of the inputs to the output i.e. switch the gain to 0 or 1. To limit the configuration bit number, not all controllers are connected to all outputs, as can be seen in Figure 4.19. During the work, this never imposed any limitations.

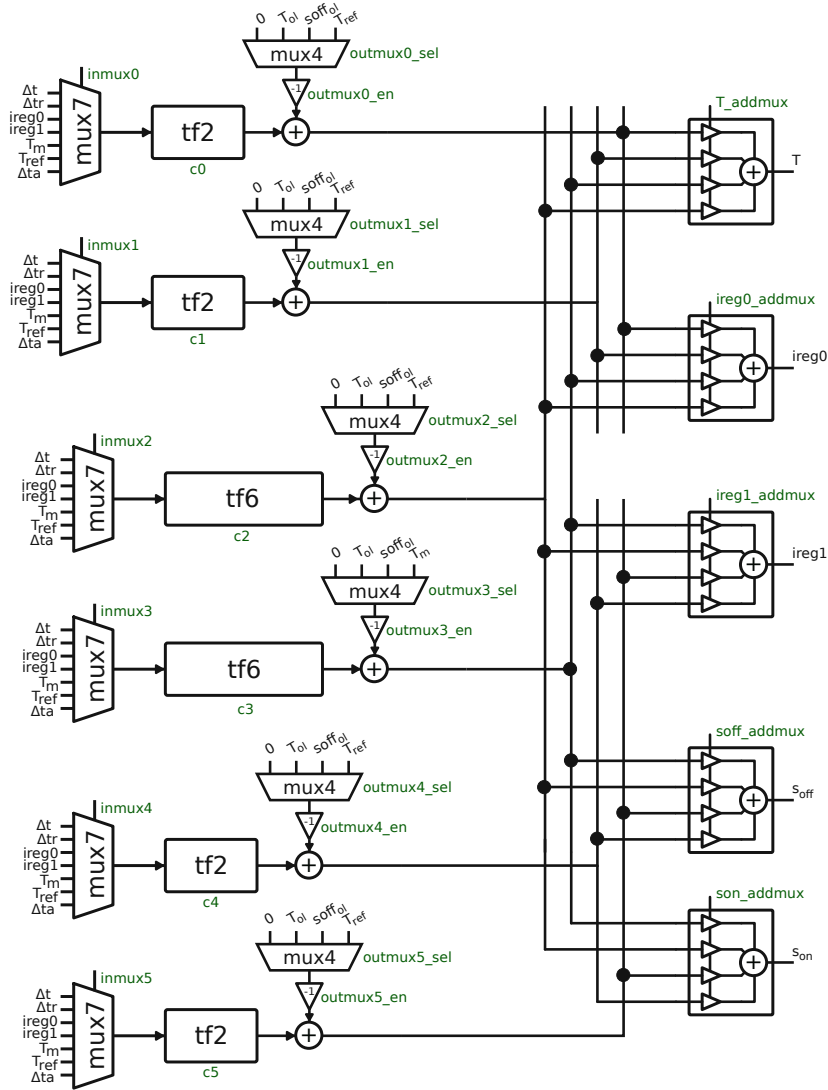


Figure 4.19: Configurable MIMO Controller consisting of four 2nd order transfer functions and 2 6th order transfer functions. The input of each transfer function can be selected from multiple measurements by configuration bits, denoted with a green font color.

To justify the design choices and the flexibility of the structure, three examples of controllers that can be set up are provided. All controllers operate at their localized operating point, so the additional linearization point is added outside of the controller.

- **Example 1: Open-loop mode.** The additional inputs of the outmux units allow to configure the open-loop mode very simply. All controller values are set to 0, outmux2_sel is set to add T_{ol} and T_addmux is set to use the output of c2 only. Similarly, outmux3_sel is set to add $s_{off,ol}$ and the value is then transferred through soff_addmux to the output.
- **Example 2: PLL only.** The controller c2 is used as PLL, the corresponding input is configured to Δt . The s_{off} output is handled just as in example 1.

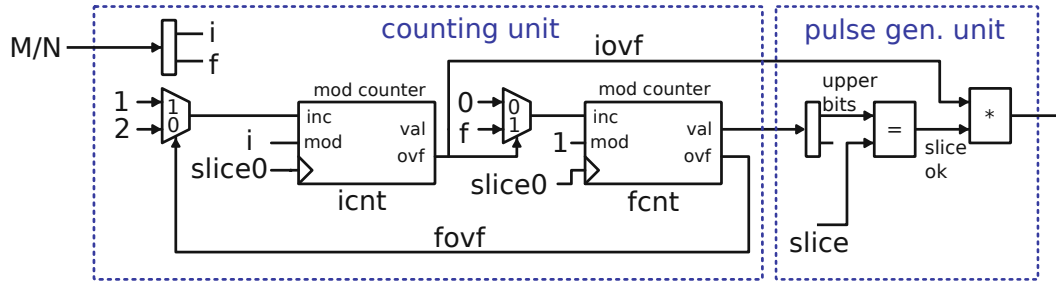


Figure 4.20: Schematic of the reference frequency generator consisting of the counting unit and the reference generation unit. It generates reference zero-crossing pulses for the slave axis out of the driving frequency of the master axis.

- **Example 3: Synchronization controller + PLL.** The T output is handled as in Example 2. The s_{off} output is controlled by a synchronization controller, implemented in `c4`. The input of the synchronization controller is given by Δtr , so `inmux4_sel` is configured to Δtr .

4.3.2 Reference Frequency Generator

The master MEMS mirror generates the reference zero-crossing pulses for the slow MEMS mirror, as shown in Figure 4.3. The reference frequency needs to be generated with ratio $\frac{M}{N}$ to achieve the correct Lissajous pattern. The faster axis is selected to be the master MEMS mirror, which implies that the ratio $\frac{M}{N}$ is ≥ 1 , i.e. more master periods occur while one slave period occurs. The reference frequency is generated from the master driving signal by a counting process. The ratio $\frac{M}{N}$ can be written as integer number $i + \frac{f}{N}$, where $f < N$ is the fractional part and i is the integer part. $\frac{M}{N}$ is handed over to the unit as a fixed point number, so the division in i and f is just a bit-splitting operation. Figure 4.20 shows the reference frequency generator. It consists of a counting unit and a pulse generation unit. The counting unit consists of two modulo counters. A modulo counter is a fixed point counting unit, which increases the value by **inc** in every step. If the counter value exceeds **mod**, then the counter is wrapped around such that the value is less than **mod**, and the overflow output **ovf** is asserted. The counting unit contains two modulo counters, one for the integer part and one for the fractional part. The integer part is increased by 1 in every driving period. If the integer part matches the desired integer part of the ratio given by i , then the overflow output is asserted, which causes the fractional part modulo counter to add f to the counter value. Also, during the time that the overflow output is asserted, the pulse generation unit is enabled. When the slice of the DCO matches the current fractional part modulo counter value, then the reference pulse is generated. If the increment of the fractional part did not cause an overflow, then the integer part is incremented by 2 instead of 1 to skip one full period to generate the correct ratio. The reason for using the upper bits of the fractional part only is that this allows the bit width of the ratio to be independent of the slice width which allows a more accurate representation of the ratio than the slices would allow. This is required for patterns where M and N are large, i.e. have high resolution and low framerate. To avoid rounding errors due to the finite precision

Table 4.1: Example for the reference generation unit counting process, generating a ratio of $\frac{27}{10}$ by full period counting and interpolation.

t	icnt	iovf	fcnt	fovf	pulse at
0.0	0	no	0.7	no	
1.0	1	no	0.7	no	
2.0	2	yes	0.7	yes	2.7
3.0	0	no	0.4	no	
4.0	1	no	0.4	no	
5.0	2	yes	0.4	yes	5.4
6.0	0	no	0.1	no	
7.0	1	no	0.1	no	
8.0	2	yes	0.1	no	8.1
9.0	1	no	0.8	no	
10.0	2	yes	0.8	yes	10.8
11.0	0	no	0.5	no	
12.0	1	no	0.5	no	
13.0	2	yes	0.5	yes	13.5
...	

of the ratio, the logic of the reference frequency generator is reset at the beginning of each Lissajous frame, which happens every N count steps.

Table 4.1 shows an example of the counting process. The first column shows the absolute timestep in periods. The second column icnt shows the value of the integer counter and the fourth column shows the value of the fractional counter. The third and fifth columns show if a counter overflow occurs. In case a reference pulse is generated, the last column shows the interpolated time at which the pulse is generated. The example shows how a ratio of $\frac{27}{10}$ is correctly generated by pulses at times $[2.7 \ 5.4 \ 8.1 \ 10.8 \ 13.5 \ \dots]$. It is also possible to verify the overflow logic. For example, the floating counter does not overflow on timestep 8, therefore the the integer counter is incremented by two, instead of one.

4.4 Experimental Evaluation

The experimental setup is depicted in Figure 4.1. The master axis operates at an oscillation frequency of 13.46 kHz. For demonstration purposes a Lissajous pattern with a ratio of $\frac{137}{24}$ is chosen, resulting in a coarse grid, a high frame rate of 98.25 Hz, and a slave axis frequency of 2.35 Hz. The shaker applies a broadband vibration of an extended automotive standard [54], with a power spectral density of $0.14 \frac{(m/s^2)^2}{Hz}$ from 2 kHz to 3 kHz. The vibration is applied perpendicular to the MEMS mirror's rotational axis, not perpendicular to the surface, as the MEMS mirror shows the most excitement to vibration in that direction [32].

The controllers are evaluated by their ability to reject disturbances caused by external vibration. In general, higher controller gains achieve a better disturbance rejection,

4 Synchronization of two 1D MEMS Mirrors

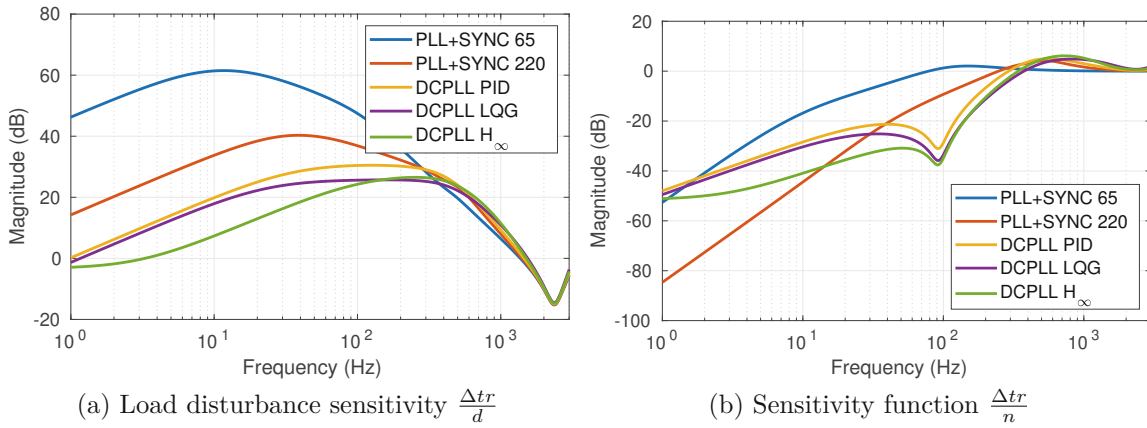


Figure 4.21: Comparison of the controllers by (a) load disturbance sensitivity function $\frac{\Delta tr}{d}$ and (b) sensitivity function $\frac{\Delta tr}{n}$.

but they also amplify the measurement noise. Therefore, the performance without external vibration must also be considered. Five different controllers are compared: two synchronization controllers implemented on top of the PLL PLL+SYNC with crossover frequencies of 65 Hz and 220 Hz, and three different DCPLLs: PID-based, LQG-based, and one designed by an H_∞ loop shaping approach.

Figure 4.21 (a) shows the frequency response from disturbance input d to synchronization error Δtr for all controllers, providing insights into achievable performance. In the low-frequency range all DCPLLs exhibit significantly lower magnitude, indicating better disturbance rejection. When comparing the LQG-based DCPLL and the H_∞ -based DCPLL, it is noteworthy that the H_∞ version performs much better at lower frequencies, while the behavior is inverted in the high-frequency range.

Figure 4.21 (b) shows the sensitivity function for all controllers. In the low-frequency range, all controllers achieve good noise rejection. Higher gains of the controllers imply increased amplification of noise, visible in the region above 400 Hz, with the H_∞ controller exhibiting the largest magnitude.

Figure 4.22 shows box plots of errors in the vibration-free and under-vibration cases. The measurement results align with the observation in Figure 4.21. Comparing the two synchronization controllers implemented on top of the PLL with different crossover frequency it is evident that the low-gain controller does not reject vibrations very effectively, but achieves a lower noise amplification. Additionally, the competition between the two controllers is noticeable. In the vibration case, the low-gain controller achieves a smaller phase error Δt , while the high-gain controller achieves a smaller synchronization error Δtr , even though the PLL remains unchanged. The high-gain synchronization controller offers a similar performance under external vibrations as the DCPLL designs. However, these gains result in a high amplification of the measurement noise, as visible in Figure 4.22 (b). In this regard, the DCPLLs perform better, allowing for higher controller gains without a drastic increase of the noise. The model-based DCPLLs outperform the PID-based DCPLL in terms of disturbance compensation but concurrently increase the amplification of the noise.

4 Synchronization of two 1D MEMS Mirrors

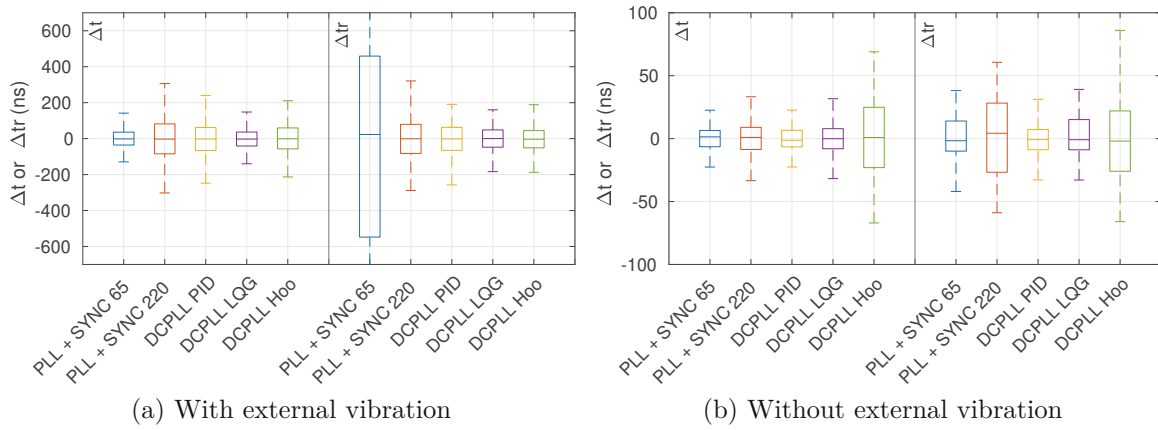


Figure 4.22: Evaluation of the synchronization controller under external vibration for different controllers under the influence of external vibration (a) and without external vibration (b). The controllers compared are a 65 Hz and a 220 Hz PID-based synchronization controller, a PID-based DCPLL as well as the LQG-based DCPLL and the H_∞ -based DCPLL.

Table 4.2: Standard deviation of different controllers with or without external vibration

	no vib Δt (ns)	no vib. Δtr (ns)	vib Δt (ns)	vib Δtr (ns)
PLL + SYNC 65	9.0	18.6	60.6	625.0
PLL + SYNC 220	12.9	28.3	113.6	118.2
DCPLL PID	8.3	13.9	94.0	86.6
DCPLL LQG	11.9	16.3	60.5	69.3
DCPLL H_∞	27.9	29.9	85.0	77.0

For completeness, Table 4.2 presents the standard deviation for the compared controllers in case of external vibration and without of the data used to plot Figure 4.22.

The PID-based DCPLL achieves a standard deviation of 86.6 ns under vibration, which is an improvement of a factor of 1.4 over the conventional design with high gains. At the same time, the performance without vibration is also reduced by a factor of 2. The improvement of the model-based DCPLLs compared to a PID-based DCPLL is a further reduction of the synchronization error by 19.9 % for the LQG controller and 11.0 % for the H_∞ controller. Since this is the slave axis, the phase error Δt is not critical, because the laser is triggered based on the slices of the master axis.

To further evaluate the performance videos of the projected Lissajous pattern have been captured while the system is under vibration influence. Figure 4.23 shows a subsection of the accumulation of 900 Lissajous scan video frames. Under external vibration, the synchronization error increases and the Lissajous pattern shows deformations as simulated in Figure 4.5, resulting in blurred lines when all frames of the video are summed up. In Figure 4.23 it is evident that the DCPLL outperforms the conventional design in all cases and by looking carefully the LQG-based DCPLL shows the sharpest lines, agreeing with the measurements in Table 4.2. Figure 4.24 plots the pixel brightness along the white line in Figure 4.23 for an objective analysis of the sharpness of lines.

4 Synchronization of two 1D MEMS Mirrors

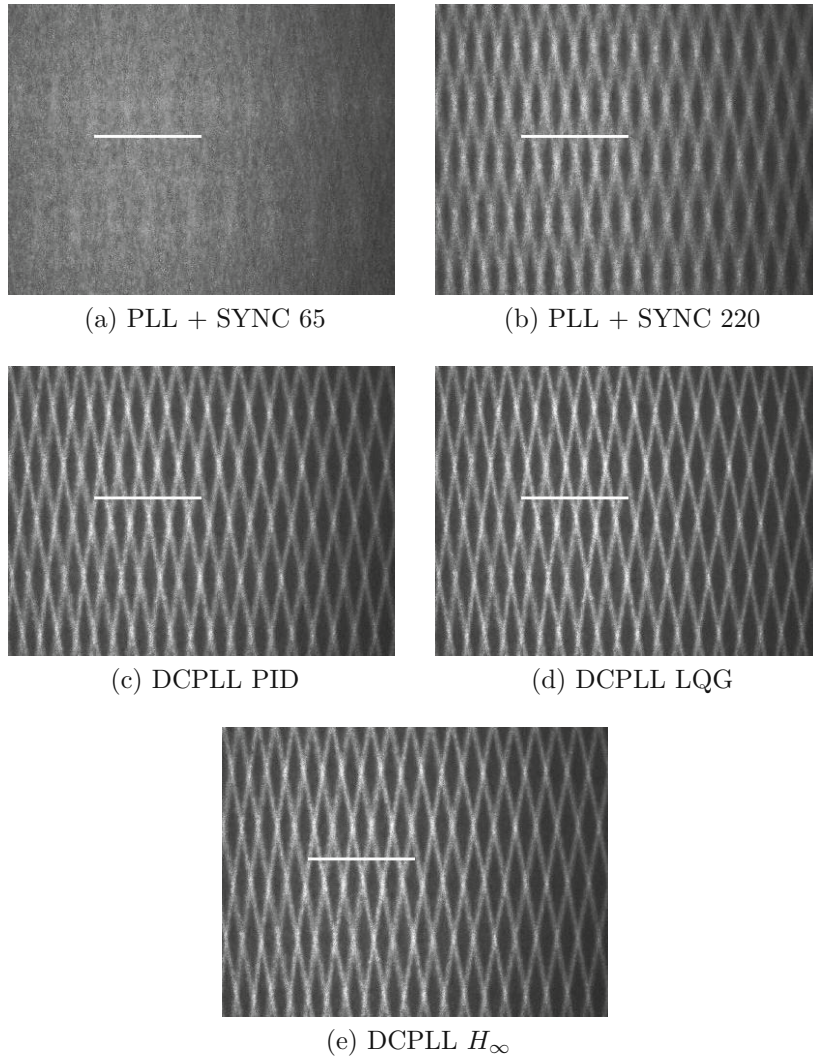


Figure 4.23: Evaluation of the uniformity of the Lissajous pattern of the controllers. The images show the sum of 900 single frames of a 30-seconds video for the same controller options presented in Figure 4.22. The white line is added to the image to signalize the coordinates used to evaluate the brightness shown in Figure 4.24.

This demonstrates that the proposed DCPLL achieves good stability under external vibrations while the design is even simpler than that of the PLL and synchronization control.

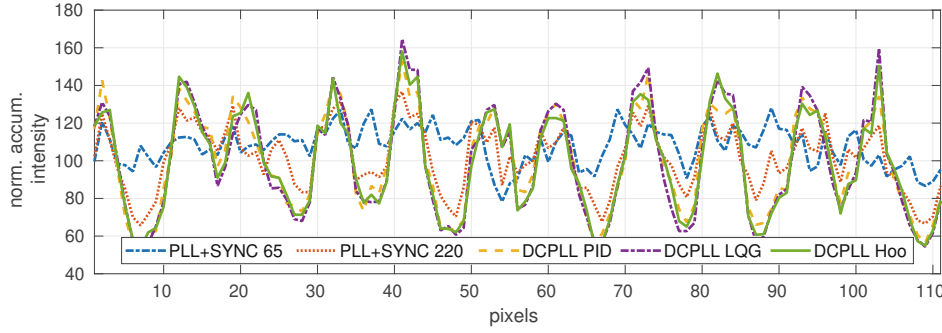


Figure 4.24: The brightness of the pixel along the white line of Figure 4.23 for the five controllers. The LQG-based and H_∞ -based version show the sharpest lines.

4.5 Summary

The synchronization of two MEMS mirrors requires an additional controller to maintain a constant phase between the master MEMS mirror and the slave MEMS mirror. In a conventional design both MEMS mirrors are operated with a PLL and an additional synchronization controller is added [43]. The synchronization controller changes the s_{off} value of the slave axis such that the slave MEMS mirror follows the frequency generated by the master MEMS mirror. This controller structure uses two different controllers to control a single MEMS mirror, and therefore introduces a competition between them, i.e. increasing the gains of the synchronization controller deteriorates the performance of the PLL. The proposed Direct Correction PLL solves this issue by running the slave MEMS mirror at the desired frequency and phase, and only using s_{off} to compensate for external disturbances. This not only simplifies the controller design but also improves the performance compared to the conventional design. The PID-based DCPLL achieves a standard deviation of 86.6 ns under the automotive vibration profile [54], which is an improvement of a factor of 1.4 over the conventional design with high gains. Even without disturbance, the PID-based DCPLL reduces the standard deviation by a factor of 2.0. Model-based DCPLLs are possible and the improvement compared to a PID-based DCPLL a further reduction of the disturbance influence by 19.9 % for the LQG controller and 11.0 % for the H_∞ controller. Even such a small improvement is reflected to the Lissajous pattern shown in Figure 4.23.

CHAPTER 5

Synchronization of a 2D Mirror

The 2D MEMS mirror consists of two nested MEMS mirror structures with a gimbal. The ratio of frequencies between the inner and the outer axis is approximately $\frac{39}{10}$. This chapter explores the global and local dynamics of the 2D MEMS mirror and designs a closed-loop controller to achieve a stable Lissajous pattern.

5.1 Dynamic Behavior

First of all the dynamic behavior of both MEMS mirror axes is investigated. Similar to the other MEMS mirror in Chapter 4 the 2D MEMS mirror has a nonlinear stiffness and therefore shows the bending oscillation frequency and the frequency jump at the resonance frequency. Figure 5.1(a) shows the response curve of the outer axis measured during startup with a position sensitive device. The MEMS mirror is operated at a duty cycle of 70.1 %, which maintains a sufficiently low mechanical angle. This results in a high duty cycle in closed-loop mode and a limit on the frequency in the open-loop mode. This is also the reason that the response curve is not drawn up to the highest amplitude. Figure 5.1(b) shows the response curve of the inner axis, with a duty cycle of 50.0 %.

5.2 Local Dynamic Behavior and Modeling

Figure 5.2 shows the local dynamics around the operating point for the outer axis. Both P_T and P_s are measured by a sine-sweep identification, and P_T is estimated with the MATLAB command `tfest`. Equation (3.17) is employed to calculate P_s , with a different scaling factor than on the previous MEMS mirror, as this setup required a Q20.12 format for the period input to set the period more precisely. Therefore, Equation (3.17) is altered to $P_s = 2^{12}(P_T(z - 1) - 1)$. The measured frequency domain data exhibits good agreement with the calculated data.

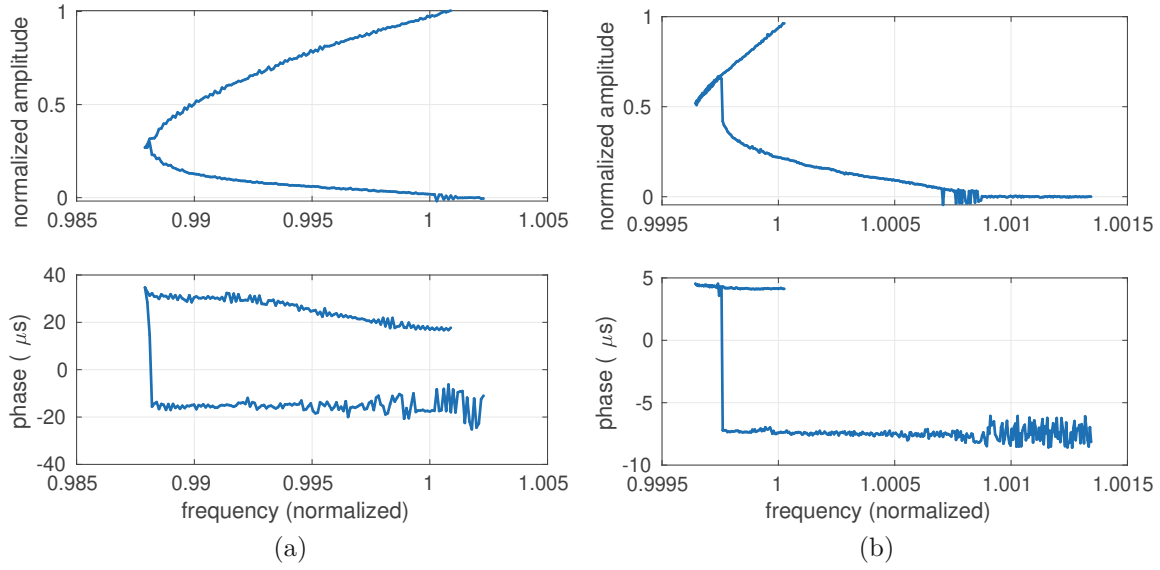


Figure 5.1: (a) Response curve of the outer axis and (b) the inner axis measured with a position sensitive device during startup.

In Section 3.1, the relation $P_s = P_T(z - 1) - 1$ was derived to show the relation between the transfer function P_s from phase offset s_{off} to Δt and T to Δt . In the case of the 1D MEMS mirror, and also for the outer axis of the 2D MEMS mirror, $P_s \approx P_{\text{sff}}$ holds because the changes in s_{off} are the significant contributors to the torque. Figure 5.3 shows the relation between the comb drive capacitance and MEMS mirror angle, and the comb drive current given by

$$I_c(t) = V \frac{dC(\theta(t))}{dt}, \quad (5.1)$$

where V is the driving voltage. The torque produced by the comb drive at time t is given by

$$\tau(t) = \frac{1}{2} \frac{dC(\theta(t))}{d\theta} V^2(t). \quad (5.2)$$

Since V is a square wave driving signal, the total torque of one MEMS mirror period is given by

$$\tau_{\text{tot}} = \frac{V^2}{2} \int_{t(s_{\text{on}})}^{t(s_{\text{off}})} \frac{dC(\theta(t))}{d\theta(t)} dt, \quad (5.3)$$

where $t(s_{\text{on}})$ is the switching on time and $t(s_{\text{off}})$ is the switching-off time. Figure 5.3 (a) shows that at the maximum angle, $\frac{dC}{d\theta}$ is small and therefore also the torque is small. This implies that local changes on s_{on} do not contribute to the total torque, compared to the torque caused by changes on s_{off} . This does not hold for the inner axis, shown in Figure 5.3 (b). The torque is non-zero at the maximum amplitude, therefore changes in s_{on} contribute to the torque too. This means that for the inner axis of the 2D MEMS mirror $s_{\text{on}} = s_{\text{off}}$ must hold. This also results in a constant duty cycle. One option to modify the local behavior of the system is to use different switching points. However,

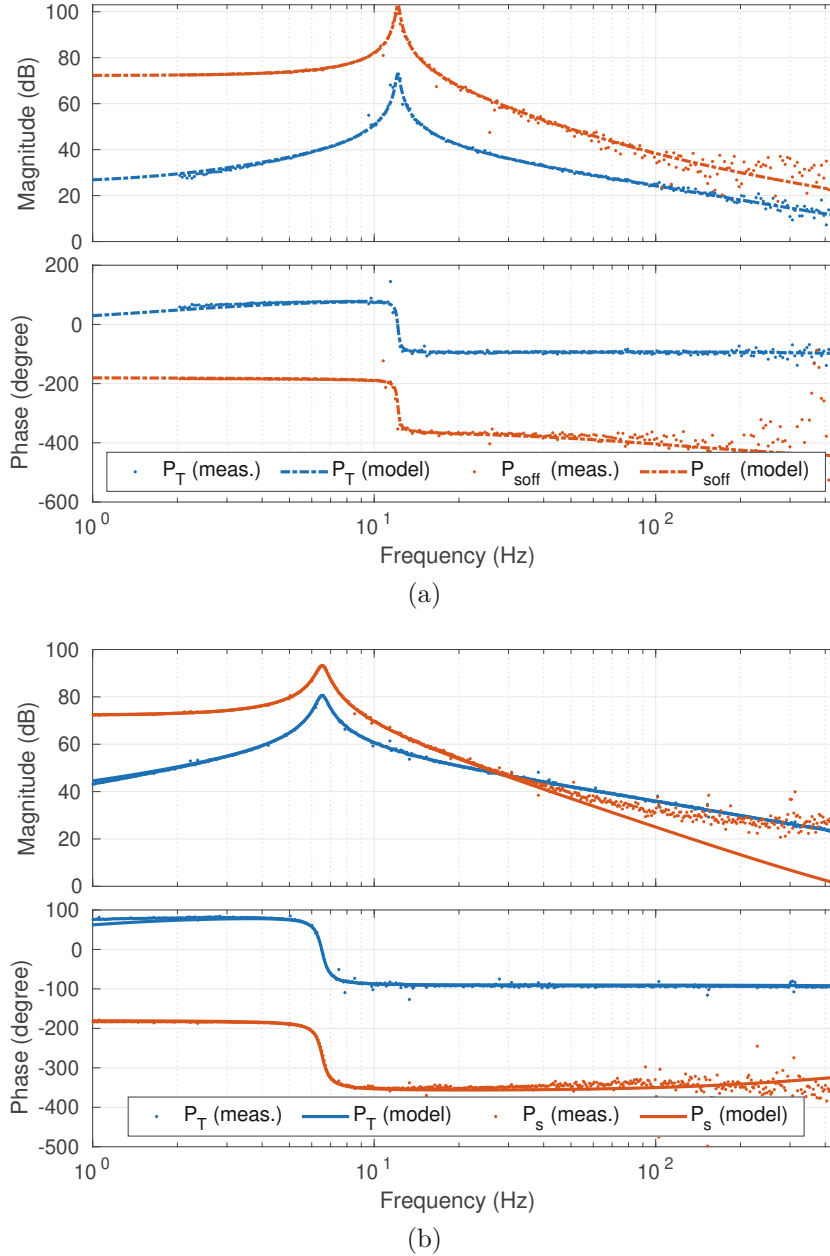


Figure 5.2: Local dynamics of the 2D MEMS mirror, showing the transfer function from DCO period T to phase error Δt and the transfer function from s_{off} to Δt for (a) the outer axis and (b) the inner axis.

this can lead to problems if the switching points are shifted to the detection window of the amplitude detection. Another option to change the transfer function P_s is to use a weighted superposition of P_{son} and P_{soff} . Figure 5.4 shows the identified transfer function P_{son} and P_{soff} , at a duty cycle of around 50 %. The transfer function P_{son} shows a zero on the left-hand side of the complex plane, while P_{soff} shows a zero on the right-hand side of the complex plane. In the proximity of the operating point, $gP_{son} + P_{soff} = P_s$ does hold. The constant gain g can be used to change the influence of P_{son} , which can be used to tune the local dynamics of the system. By selecting g appropriately, the zero

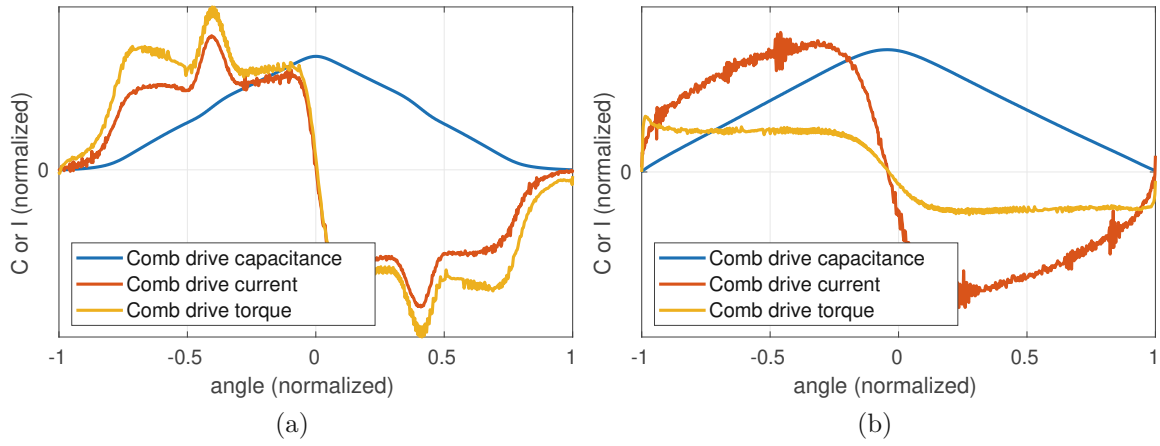


Figure 5.3: Relation between comb drive capacitance and the MEMS mirror angle for (a) the outer axis and (b) the inner axis of the 2D MEMS mirror.

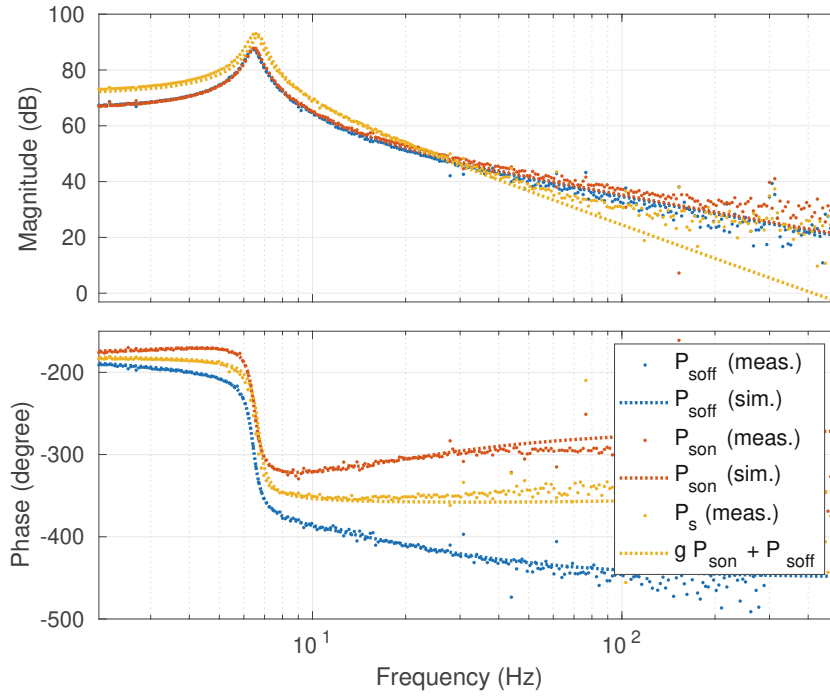


Figure 5.4: Measured transfer function P_{son} and P_{soff} and placement of the zero of $P_s = kP_{\text{son}} + P_{\text{soff}}$ by selecting $k = 0.95$ to obtain a transfer functions without a zero.

of the transfer function can be influenced. The weighted superposition can be written down as

$$P_s = gP_{\text{son}} + P_{\text{soff}}. \quad (5.4)$$

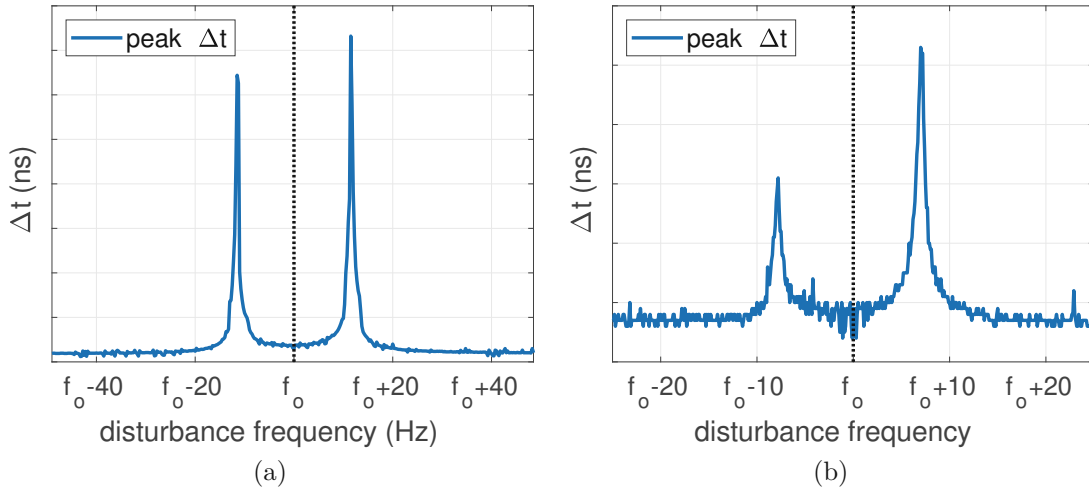


Figure 5.5: (a) Influence of the vibration on the outer axis (b) Influence of the vibration on the inner axis. In both cases, the vibration shows the largest influence on the phase error Δt slightly above or below the oscillating frequency f_o . The peak of the vibration influence aligns with the resonance peak of the local dynamics.

If P_s and P_T are written in continuous domain

$$\begin{aligned} P_{\text{son}} &= \frac{b_{\text{son},1}s + b_{\text{son},0}}{s^2 + a_1s + a_0}, \\ P_{\text{soff}} &= \frac{b_{\text{soff},1}s + b_{\text{soff},0}}{s^2 + a_1s + a_0}, \end{aligned} \quad (5.5)$$

then Equation (5.4) calculates to

$$P_s = \frac{(b_{\text{soff},1} + gb_{\text{son},1})s + b_{\text{soff},0} + gb_{\text{son},0}}{s^2 + a_1s + a_0}. \quad (5.6)$$

Trivially, g can be selected such that the non minimum phase of P_s is avoided, specifically even such that the zero disappears in transfer function P_s . Figure 5.4 shows how this was done for a duty cycle of approximately 50 % by selecting $g = 0.95$. This fact is useful for the design of the DCPLL, because a non minimum phase on the transfer function would result in a low limit on the bandwidth of the closed-loop controller.

5.3 Vibration Influence

To evaluate the influence of external vibrations on the MEMS mirror the MEMS mirror is mounted on a custom-built piezo actuated shaker. The shaker allows movement in both x and y directions with a frequency as high as the MEMS mirror oscillation frequency. Figure 5.5 shows the influence of external vibration on the MEMS mirror. To obtain this data, the MEMS mirror is operated in open-loop mode, and a sinusoidal voltage is applied to the piezo actuator of the shaker, generating a sinusoidal acceleration

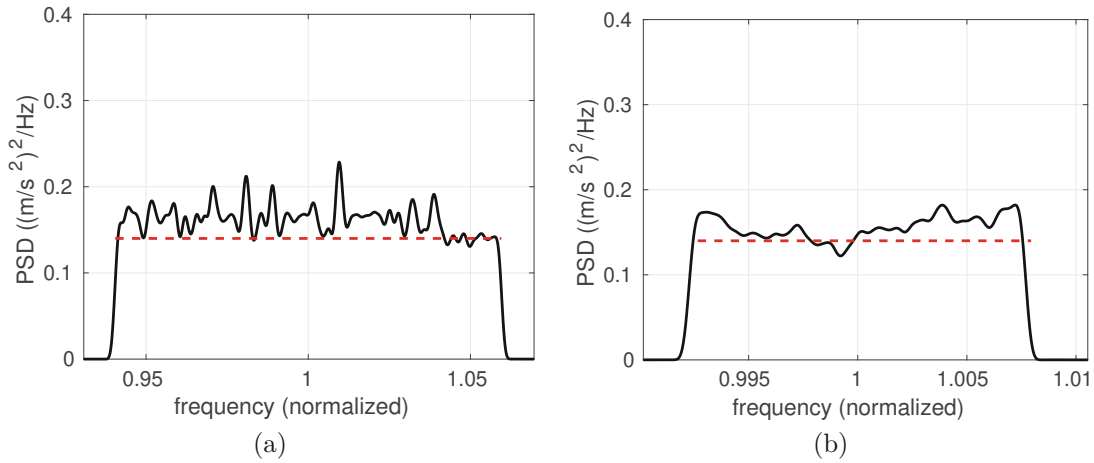


Figure 5.6: Vibration profile used to evaluate the controller of the 2D MEMS mirror for (a) the outer axis and (b) the inner axis

and the maximum value of the phase error Δt is measured. The strongest influence occurs slightly above and below the MEMS mirror oscillation frequency. The peak of the vibration influence aligns with the resonance frequency of the local dynamics.

To evaluate the performance of the controllers a broadband vibration is applied to the MEMS mirror. Figure 5.6 shows the broadband vibration profile used to evaluate the performance of the controller. Two different vibration profiles are used for x and y direction, because the MEMS mirror is only excited by vibrations close to its resonance frequency. The automotive standard [54] does not define any PSD at this frequency ratio, so the identical value as for the lower frequency is assumed.

5.4 Mechanical Coupling

5.4.1 Mechanical Coupling Effects on the Global Dynamics

In a simplified way the inner axis of the MEMS mirror can be viewed as a circular disk with mass m and radius r , whose inertia perpendicular to the surface is given by $I_z = \frac{mr^2}{2}$ and the moment of inertia parallel to the surface is $I_x = I_y = \frac{mr^2}{4}$. If the angle α of the inner axis increases, i.e. the MEMS mirror rotational axis changes from x to z , then the moment of inertia of the outer axis, given by the sum of the moment of inertia of the inner axis and the moment of inertia of the frame, increases as well. Figure 5.7 shows that the jump frequency of the outer axis changes if the inner axis is operational, because the moment of inertia of the inner axis, averaged over time, increases if the inner axis is oscillating. A higher inertia results in a lower resonance frequency of the system, which can be observed in the response curve of the outer axis. Due to the ratio of masses between the inner axis and the outer axis the difference is only marginal, but can be observed in the zoomed-in section in Figure 5.7 (b). Figure 5.8 shows the difference in jump frequency for the inner axis. This time the frequency shift is caused by the centrifugal moment.

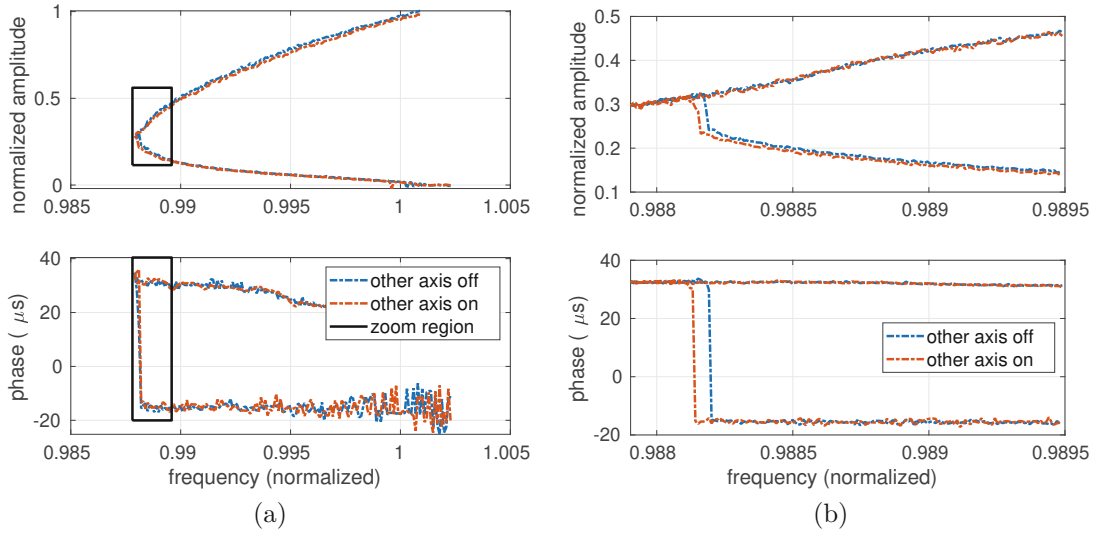


Figure 5.7: (a) Response curve of the outer axis of the 2D MEMS mirror measured with a position sensitive device during startup and (b) zoomed section of the frequency range where the amplitude jump occurs. If the inner axis is operational, the jump frequency of the outer axis is slightly shifted, showing that the moment of inertia changed.

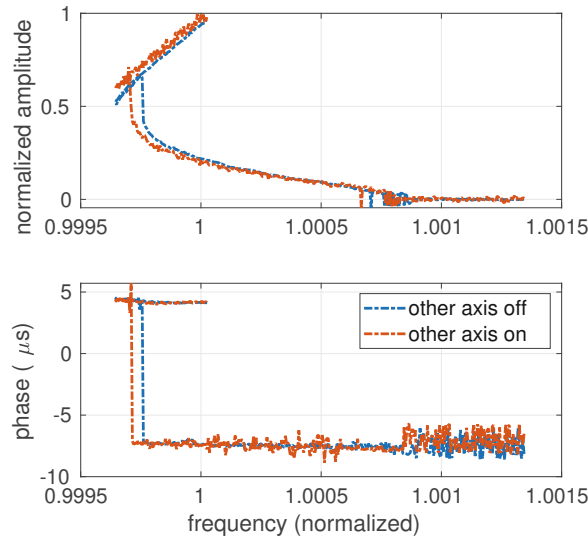


Figure 5.8: Response curve of the inner axis of the 2D MEMS mirror following the shape of the Duffing oscillator. If the outer axis is operational, the jump frequency is shifted due to the centrifugal force.

5.4.2 Mechanical Coupling Effects on the Local Dynamics

Figure 5.9 shows the influence of the operation of the other axis on the local dynamics. The measurements are taken with both axes running in open-loop mode, and a sine wave signal is applied to T or s_{off} of one axis, while the phase error is measured on the other axis. Figure 5.9 (a)+(b) demonstrates that there are nearly no coupling effects from the outer axis to the inner axis, and only small coupling effects from the inner axis to the outer axis shown in Figure 5.9 (c)+(d). Figure 5.10 shows the local dynamics of the fast and outer axis compared to the dynamics if the other axis is switched on. Figure 5.10 (a)+(b) shows that the local dynamics of the outer axis are not influenced by the operation of the inner axis. However, the resonance frequency of the inner axis changes slightly if the outer axis is switched on as shown in Figure 5.10 (c)+(d).

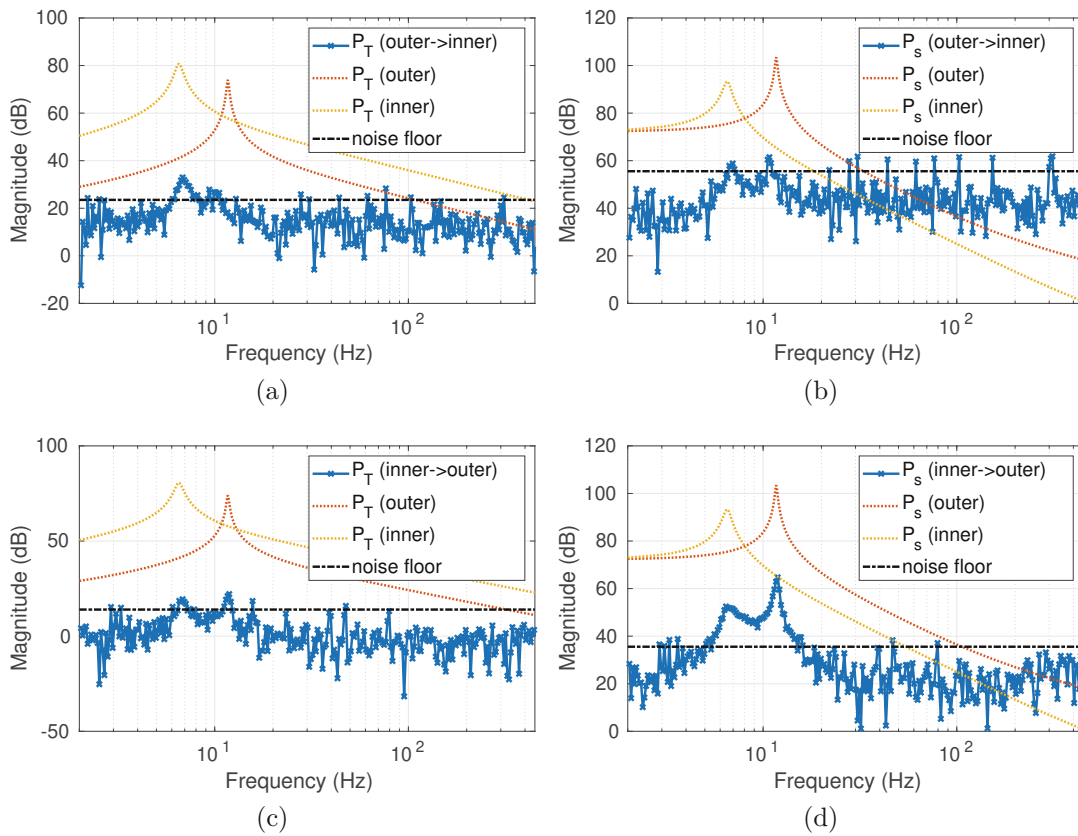


Figure 5.9: Coupling influence on the local dynamics. (a + b) Measured phase error of the inner axis when the outer axis is excited (c + d) Measured phase error of the outer axis when the inner axis is excited.

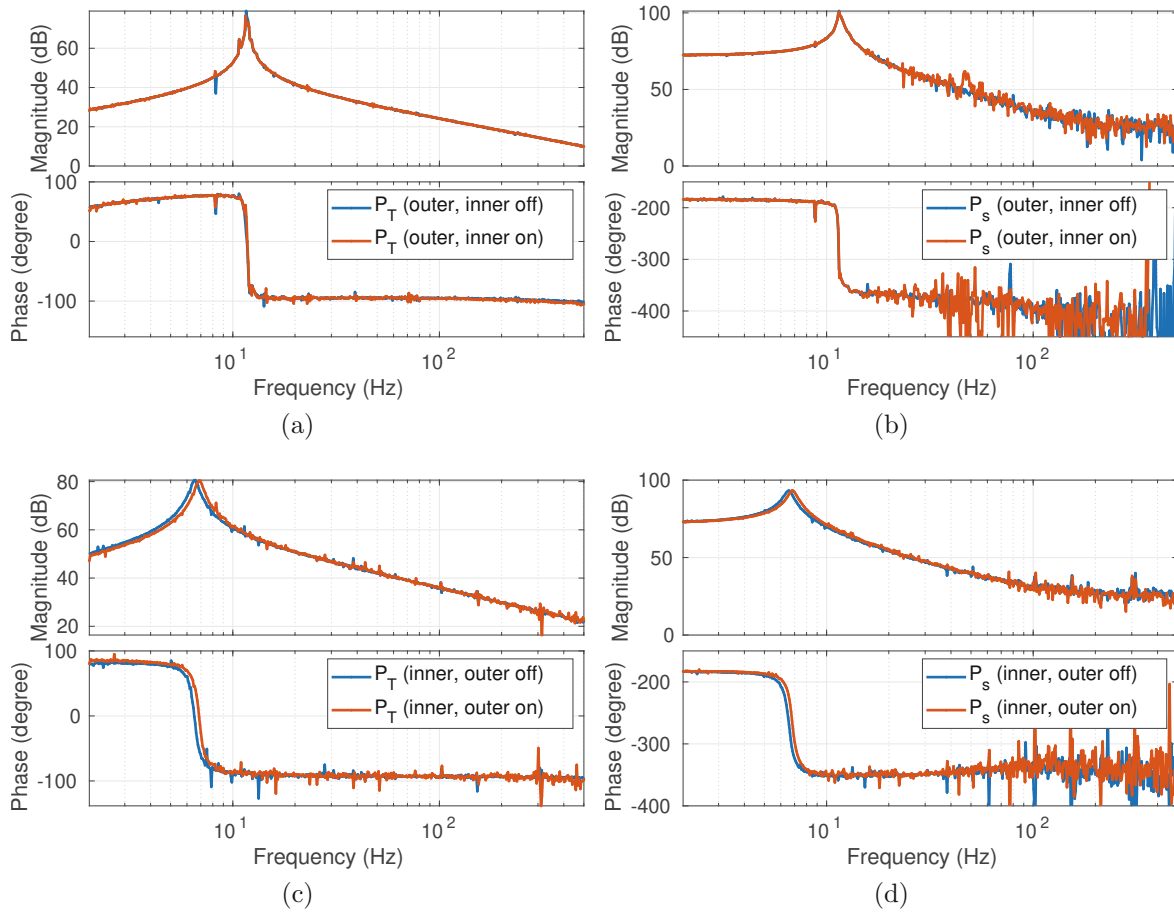


Figure 5.10: Influence of the oscillation of one axis on the local dynamics of the other axis. The transfer functions (a) P_T and (b) P_s of the outer axis are hardly influenced by the inner axis operation. (c) P_T and (d) P_s of the inner axis show a slight shift in resonance frequency if the outer axis is operational or not.

5.5 Electrical Crosstalk

A high-voltage switching process distorts the current on both sensing combs, making the measurement on either axis unreliable. Figure 5.11 depicts the normalized MEMS mirror angle and the normalized driving voltage for both the outer and inner axes. The red areas indicate a time region after the high voltage switching process during which no sensing is possible. The length of this time region is determined experimentally by observing the distortion via oscilloscope. Figure 5.12 displays the same graph, but both axes are combined in a Lissajous frame. Red paths are used to indicate that no measurement can be taken on this section. If the red paths cross the x-axis or the y-axis, which implies that a zero-crossing would be necessary to detect, then this zero-crossing cannot be measured. With this example ratio of $\frac{39}{10}$ this only happens a few times in the Lissajous frame, and those zero-crossings are marked with a black square. Figure 5.13 shows the experimental evaluation of the previous considerations. The phase detector observes the switching of the other axis and blocks the zero-crossings for a certain time period after a switching event, which removes zero-crossing edges if crosstalk occurred, leading to missing zero-crossings signals. Figure 5.13 indicates the simulation results with red and green bars for a full Lissajous frame. Green bars indicate that no crosstalk occurred when measuring this zero-crossing, and red bars indicate that crosstalk occurred. The black signal corresponds to the measured zero-crossing signal, showing good agreement with the measured data, i.e. the zero-crossing edge is removed in red-section due to the crosstalk.

Discarding the measurements removes measurements that are disturbed by crosstalk, therefore not causing any unexpected control actions. However, it is crucial to acknowledge that the underlying problem persists. There is a possibility that no measurements are available, implying that the MEMS mirror does not provide any feedback and therefore must be operated in open-loop mode. Fortunately, the ratio between the MEMS mirror axes is not precisely 4.0, but around 3.9, meaning that it cannot happen that all measurements are invalid, which guarantees at least some measurements to maintain observability.

5.6 Controller Design for the Outer Axis

This section adapts the controller designs to the 2D MEMS mirror. The PLL design and synchronization concepts are identical with the ones introduced in Chapter 3 and 4, respectively. First, the PLL is designed, and subsequently, to synchronize both axes, an additional synchronization controller is designed. Furthermore, a PID-based DCPLL and an LQG-based DCPLL are designed and compared by their capability to reject external vibrations.

5.6.1 PLL and Conventional Synchronization Controller Design

To run a single MEMS mirror axis in closed-loop a PLL can be used. The control loop for the PLL-controlled MEMS mirror is shown in Figure 3.4. Figure 5.14 (a) shows the transfer functions of the PLL's controller C_{PLL} , the plant transfer function P_T and

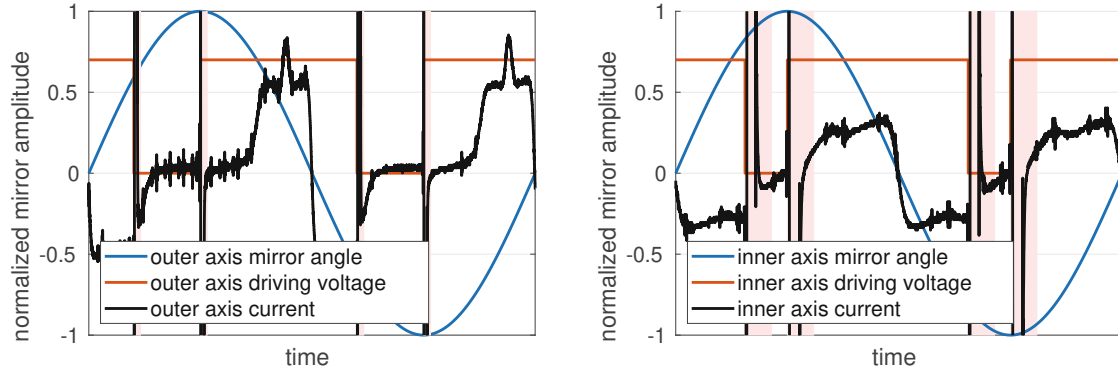


Figure 5.11: Illustration of the time regions after the switching of the driving signal where it is not possible to use the sensing signals of both axes due to crosstalk.

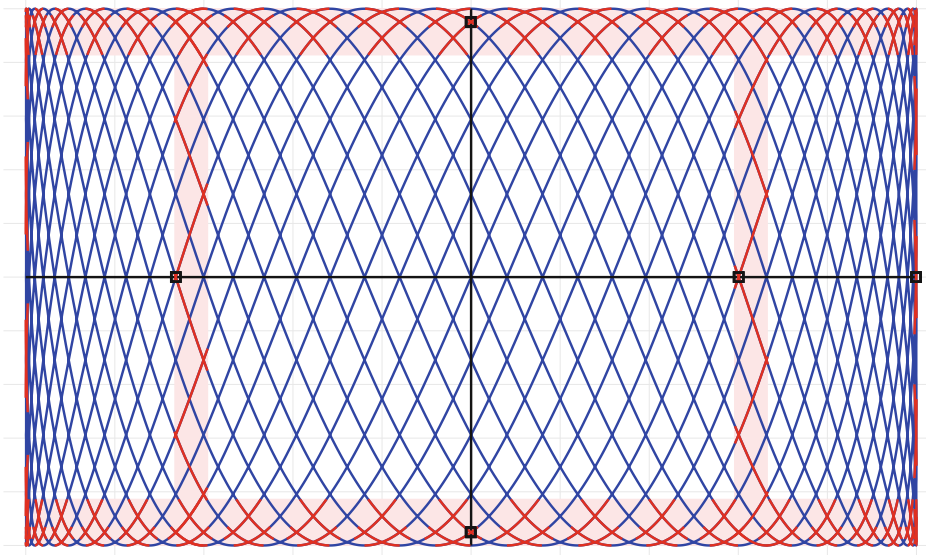


Figure 5.12: Invalid measurement regions depicted in the Lissajous frame. Red paths on the trajectory indicate position where the sensing signal is distorted. If such paths cross the axis, then the zero-crossing cannot be measured, which is denoted with a black square.

the open-loop function $L = C_{PLL}P_T$. Figure 5.14 (b) shows the closed-loop transfer function from the unused input s_{off} to Δt calculated by $T_{\Delta t} = \frac{P_s}{1+L}$. The PLL achieves a crossover frequency of 50 Hz and a phase margin of 43° .

Similar to Section 4.1 the PLL-operated MEMS mirror system is extended by a synchronization controller C_{SYNC} on the slave axis. The PID-based controller synchronization controller controls the s_{off} input of the PLL-driven MEMS mirror to achieve a constant frequency ratio between the master and the slave MEMS mirror. Figure 5.15 (a) shows the open-loop transfer functions $T_{\Delta t}$ and $T_{\Delta tr}$ from s_{off} to Δt and Δtr . The phase error Δt is already controlled by the PLL, but the synchronization error Δtr shows integrating behavior. Therefore an additional synchronization controller C_{SYNC} with transfer functions shown in Figure 5.15 (a) is added to the system. The resulting loop transfer

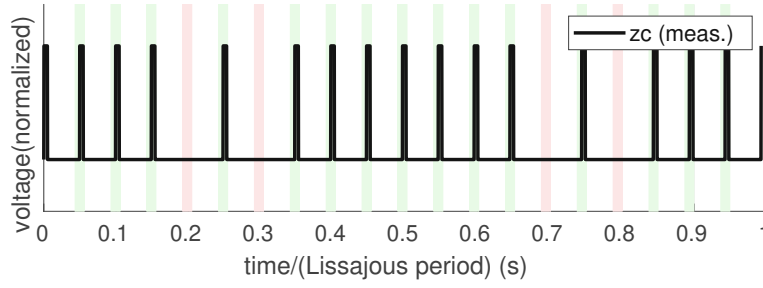


Figure 5.13: Experimental evaluation of invalid zero-crossings with the oscilloscope. Due to the switching of the inner axis some zero-crossing measurements of the outer axis are distorted and cannot be taken. The black signal corresponds to the measured zero-crossing signal. Sometimes, the signal is removed due to the fact that it is distorted by the switching of the fast axis. The red and green bars indicate the simulation results: Green bars indicate, that the measurement can be taken, and red bars indicate, that the measurement is distorted.

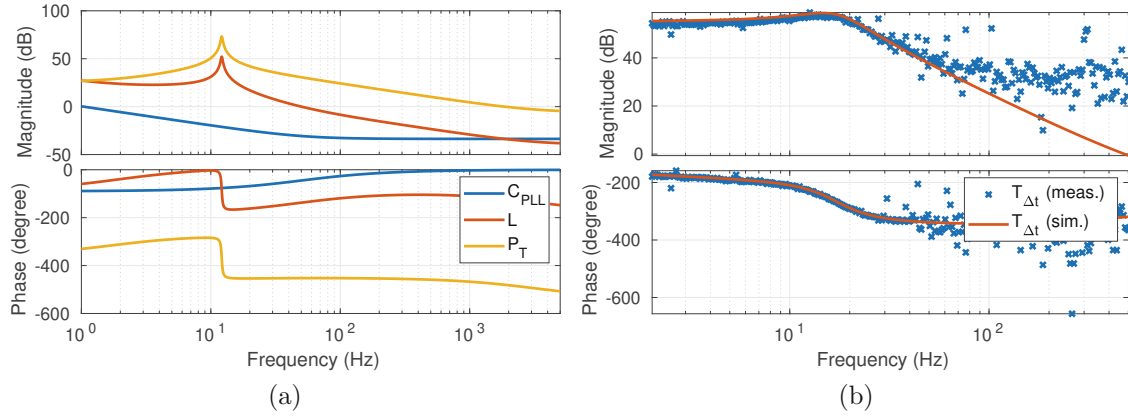


Figure 5.14: (a) Transfer functions of the PLL design for the outer axis. The PI controller C_{PLL} stabilizes the plant P_T . The open-loop transfer function has a crossover frequency of 50 Hz and a phase margin of 43° . (b) The measured closed-loop transfer function $P_{\Delta t}$ from s_{off} to Δt closely matches the resulting calculation up to the frequency where the measurement noise is to large.

function $L = C_{SYNC}T_{\Delta tr}$ has a crossover frequency of 47.7 Hz and a phase margin of 41.5° . Figure 5.15 (b) shows the load disturbance sensitivity function $T_{d,\Delta t}$ and $T_{d,\Delta tr}$ from a disturbance d acting additively on s_{off} to phase error Δt and synchronization error Δtr . The controller loop is identical to the one depicted in Figure 4.10 (a).

5.6.2 PID-based DCPLL

The conventional synchronization structure suffers from the competition between the phase error and synchronization error, analyzed in Section 4.1.3. The DCPLL proposed

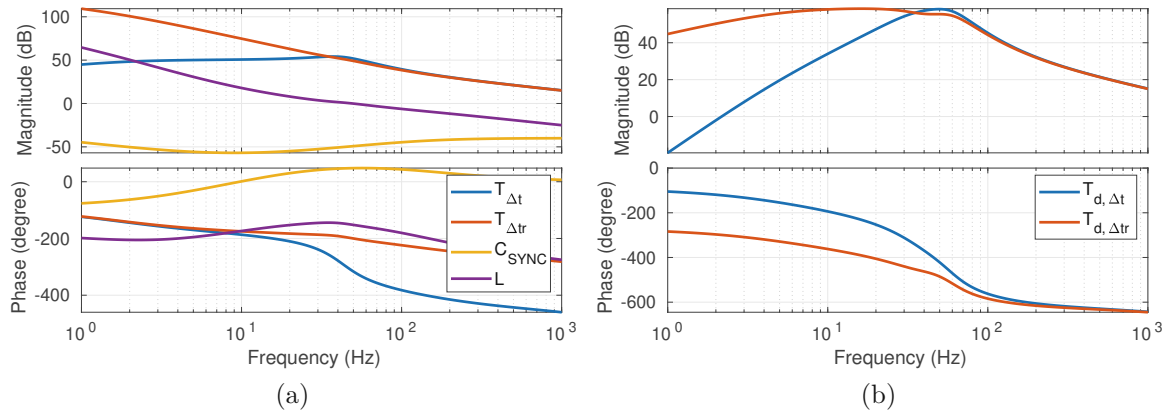


Figure 5.15: PID-based synchronization controller design for the outer axis of the 2D MEMS mirror. (a) open-loop transfer functions $T_{\Delta t}$ and $T_{\Delta tr}$ from s_{off} to Δt and Δtr of the PLL controlled MEMS mirror, as well as the transfer function of the synchronization controller C_{SYNC} and the resulting loop function $L = C_{sync}T_{\Delta tr}$. (b) Resulting transfer functions from a disturbance d acting additively on s_{off} to phase error Δt and synchronization error Δtr .

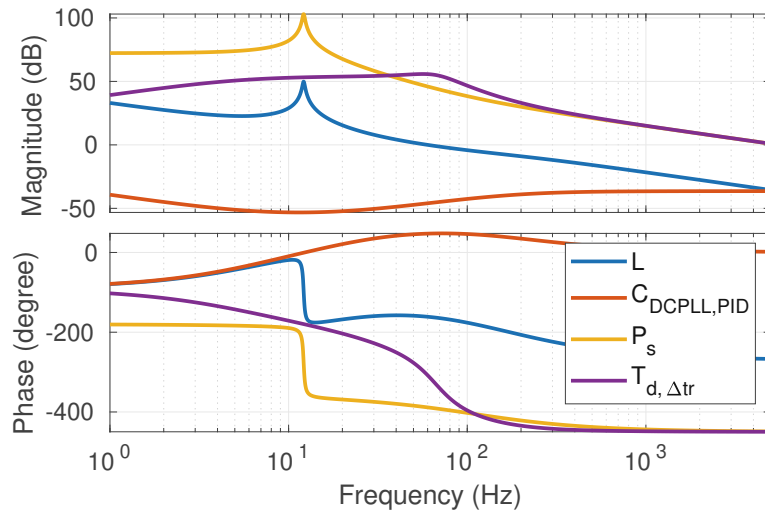


Figure 5.16: Transfer functions for the PID-based DCPLL design for the outer axis of the 2D MEMS mirror. The controller $C_{DCPLL,PID}$ controls the s_{off} input of the system P . The loop function $L = C_{DCPLL,PID}P_s$ has a crossover frequency of 50 Hz and a phase margin of 26.2° . The resulting load disturbance sensitivity function $T_{d, \Delta tr}$ is also shown.

tackles this issue and is also applied to the slave axis of the 2D MEMS mirror. Figure 5.16 shows transfer functions for the PID-based DCPLL design for the outer axis of the 2D MEMS mirror. The controller $C_{DCPLL,PID}$ controls the s_{off} input of the system P . The loop function $L = C_{DCPLL,PID}P_s$ has a crossover frequency of 50 Hz and a phase margin of 26.2° . The resulting transfer function $T_{d, \Delta tr}$ from disturbance to Δt reaches the highest magnitude at frequencies of around 90 Hz.

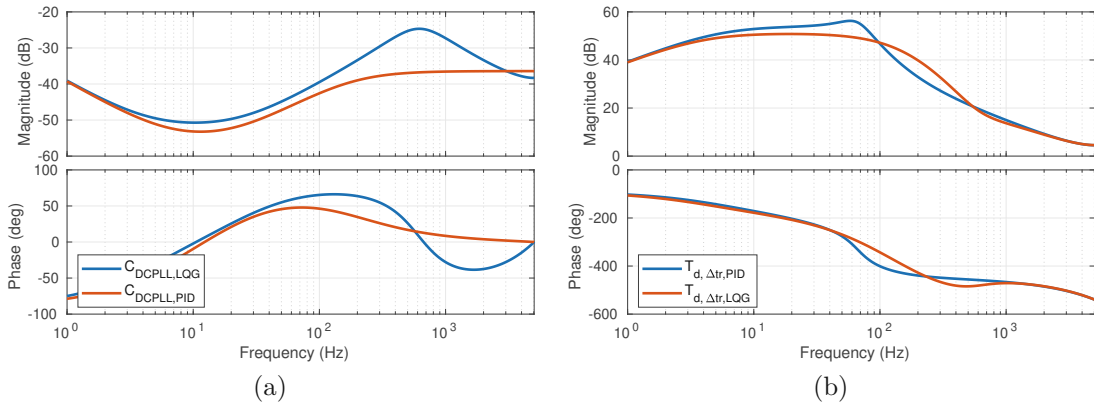


Figure 5.17: (a) Controller transfer function for the PID-based DCPLL $C_{DCPLL,PID}$ and the LQG DCPLL $C_{DCPLL,LQG}$ and (b) the resulting disturbance rejection transfer functions T

5.6.3 LQG-based DCPLL

The LQG-based DCPLL can be used for this MEMS mirror too. The approach is completely identical to the one described in detail in Section 4.2.2. For completeness, the tuning parameters for the LQR used for this MEMS mirror are

$$\begin{aligned} Q &= \text{diag} \left(\begin{bmatrix} 1 & 1 & 10^{-5} \end{bmatrix} \right), \\ R &= 1000 \end{aligned} \quad (5.7)$$

and for the Kalman filter

$$\begin{aligned} Q_n &= 7.3 \cdot 10^5, \\ R_n &= 4.1 \cdot 10^8, \end{aligned} \quad (5.8)$$

where Q_n and R_n have been obtained by measuring Δtr in open-loop mode with and without vibration and calculating the variance of the signals. Figure 5.17 shows the controller transfer function of the DCPLL $C_{DCPLL,LQG}$ compared to the PID-based DCPLL $C_{DCPLL,PID}$. The LQG controller allows for higher gains and therefore offers better disturbance rejection, which can be seen by comparing $T_{d,\Delta tr,PID}$ and $T_{d,\Delta tr,LQG}$. The LQG controller is able to suppress disturbances better in the low-frequency range up to 100 Hz, but performs slightly worse between 100 Hz and 400 Hz.

5.6.4 Evaluation

To assess the performance of the synchronization controllers the designed controllers are implemented on the FPGA and then applied to the experimental setup.

Figure 5.18 shows a block diagram overview of the experimental setup. The shaker can apply vibrations in both directions, but for evaluation of the controller of the outer axis, only vibrations along the x direction are applied. Previous experiments have shown that the main cause for the influence of vibration on the MEMS mirror is the

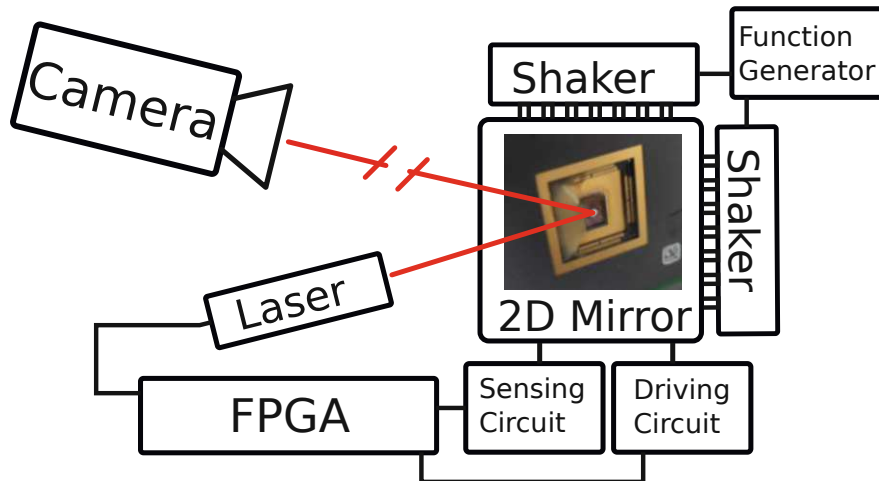


Figure 5.18: Experimental setup for the evaluation of the 2D MEMS mirror under vibration influence. The piezo-actuated shaker can move the MEMS mirror along x and y direction.

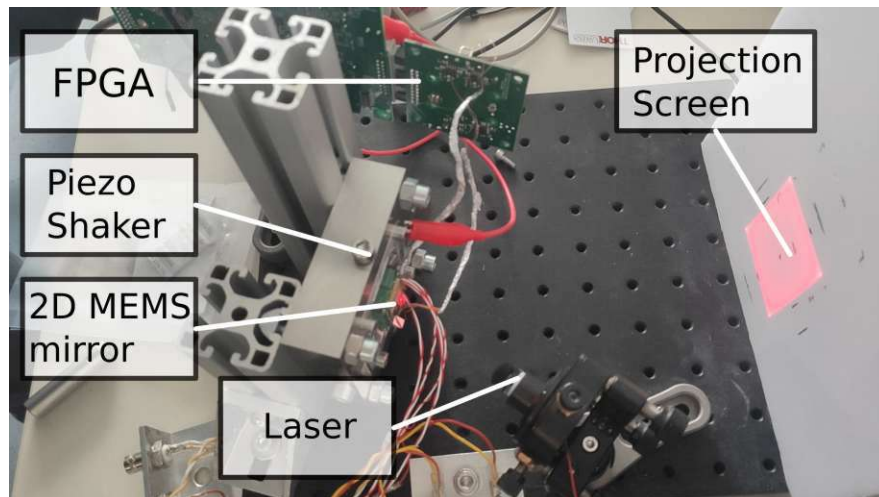


Figure 5.19: Photograph of the lab setup for the 2D MEMS mirror, mounted on the shaker.

misalignment between the center of mass and the rotational axis [32]. Figure 5.19 shows a photograph of the experimental setup. Figure 5.6 (a) shows the power spectral density of the vibration used to evaluate the controller robustness against external vibrations. The power spectral density is measured by an external vibrometer. To obtain the measurement data the system is run under external vibration, and time-domain samples of the synchronization Δtr are measured directly by the FPGA. As described in the Chapter 4, the synchronization error is a good performance criteria to evaluate the synchronization performance. Figure 5.20 shows the boxplots of 2560 time-domain samples obtained directly on the FPGA by running four different controllers.

- PLL+SYNC, LG is a low-gain reference implementation designed without considering external vibrations, and a controller structure with a PI-based synchronization

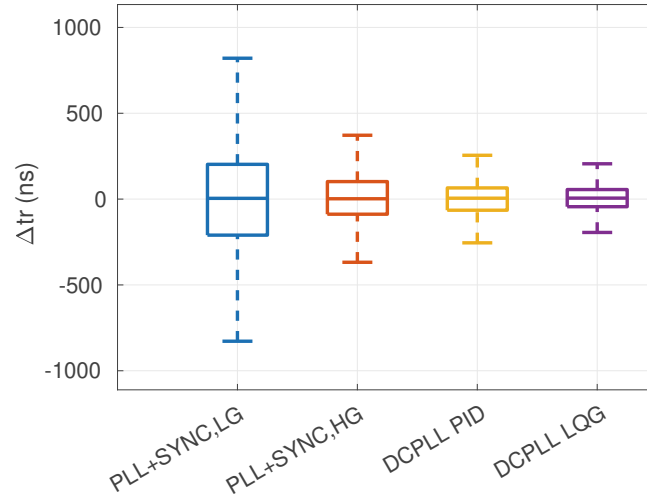


Figure 5.20: Evaluation results for the 2D MEMS mirror controllers under vibration influence. The time-domain data is measured and boxplots can be plotted showing the performance of the three proposed controllers.

Table 5.1: Standard deviation of different controllers with or without external vibration

	vib. Δtr (ns)	no vib. Δtr (ns)
PLL + SYNC LG	321.5	N.A.
PLL + SYNC HG	160.0	16.9
DCPLL PID	110.5	14
DCPLL LQG	86.3	14

controller on top of PLL-operated MEMS mirrors.

- PLL+SYNC, HG shows a reimplementation of the same controller with a PID-based synchronization controller, as described in Section 5.6.1 and analyzed in a detailed manner in Section 4.1.
- DCPLL PID is the PID-based controller design for the DCPLL, described in Section 5.6.2.
- DCPLL LQG is the LQG-based DCPLL design of Section 5.6.3.

The standard deviation under external vibration of the low-gain PLL+SYNC controller calculates to 196 ns, and the high-gain structure achieves 125 ns. The DCPLLs outperform the conventional structure, the PID-based DCPLL achieves 90 ns, and the LQG-based DCPLL achieves 51 ns. For further verification, videos of a section of the Lissajous pattern have been taken. The sum of all frames is computed, showing blurred lines if the Lissajous pattern is not stable.

Figure 5.21 shows the sum of the 20 s videos for the four controllers. The sharpness of the lines is related to the standard deviation of the synchronization error. The LQG-based DCPLL shows the lowest standard in Table 5.1, and also shows the sharpest lines in Figure 5.21. Figure 5.22 shows the evaluation of the pixel brightness along the white line in Figure 5.21. This provides a more objective criteria for line sharpness.

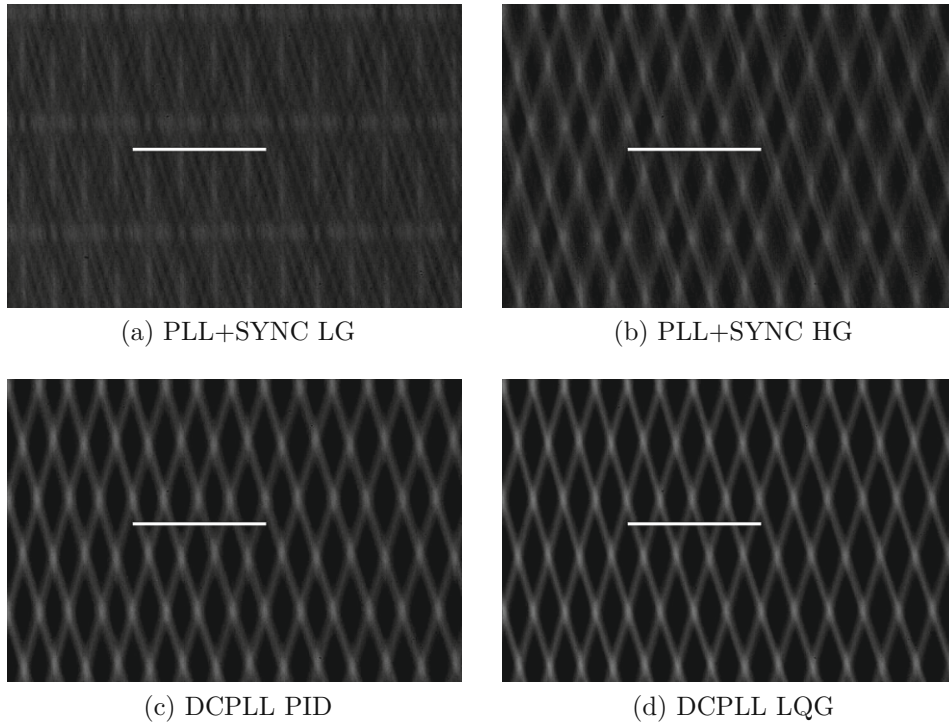


Figure 5.21: Evaluation of the uniformity of the Lissajous pattern of the controllers. The images show the sum of 600 single frames of a 20-seconds video for (a) the conventional design with a low gain, (b) the conventional design with higher gains, (c) the PID-based DCPLL, and (d) the LQG-based DCPLL. For illustration purposes, the contrast of the images has been increased. The white line signals the coordinates used for the evaluation of pixel brightness in Figure 5.22.

For completeness, Table 5.1 shows the standard deviation of the experiments in vibration case and without vibration. It is visible, that the DCPLL performs better under vibration, reducing the standard deviation from 160 ns to 110 ns for the PID-based version or 86 ns for the LQG-based version. Model-based control outperforms the conventional PID design. Even without external vibration, both DCPLLs reach a very small synchronization error. As the clock frequency is 100 MHz, without vibration, the measured values are already limited by the measurement resolution of the phase detector.

5.7 Controller Design for the Inner Axis

The inner axis represents the master axis, therefore a synchronization controller is not necessary. However, the inner axis is also strongly influenced by vibration. Even though a PLL is sufficient to keep the phase error Δt low, the amplitude changes due to vibrations, which degrades the image quality. This section develops the PLL and two controllers to improve the robustness of the MEMS mirror amplitude under vibration influence. First, the DCPLL is used to stabilize the amplitude of the inner axis by

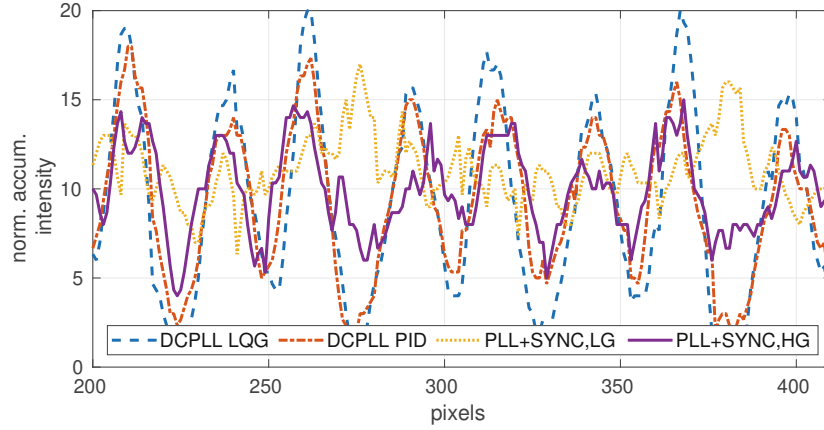


Figure 5.22: Evaluation results for the 2D MEMS mirror controllers under vibration influence by the intensity of the sum of all frames along the white line depicted in Figure 5.21

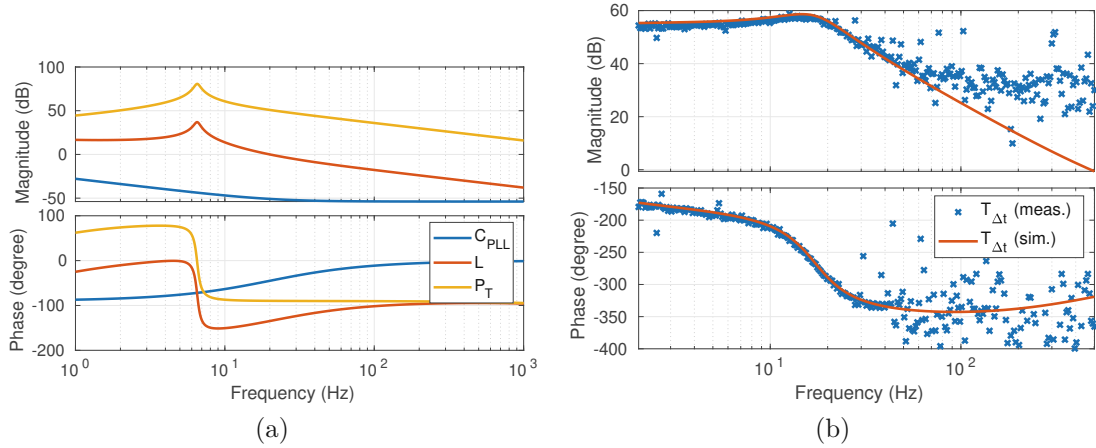


Figure 5.23: (a) Transfer functions of the PLL design for the inner axis. The PI controller C_{PLL} stabilizes the plant P_T . The open-loop transfer function has a crossover frequency of 20 Hz and a phase margin of 41° . (b) The measured closed-loop transfer function from $s_{off} = s_{on}$ to Δt shows similar trend to the calculation. However, because of the small period a phase error of one clock cycle is already large, therefore the errors are too small to detect by measuring Δt in clock cycles.

locking to an internally generated reference period. This forces the MEMS mirror to run at a certain frequency, and due to the response curve shown in Figure 5.1, it also stabilizes the amplitude. Second, a conventional amplitude controller is developed that uses the amplitude-crossing signal. The PI-based amplitude controller modifies the phase input of the PLL. Both controllers are then evaluated on the setup under vibration.

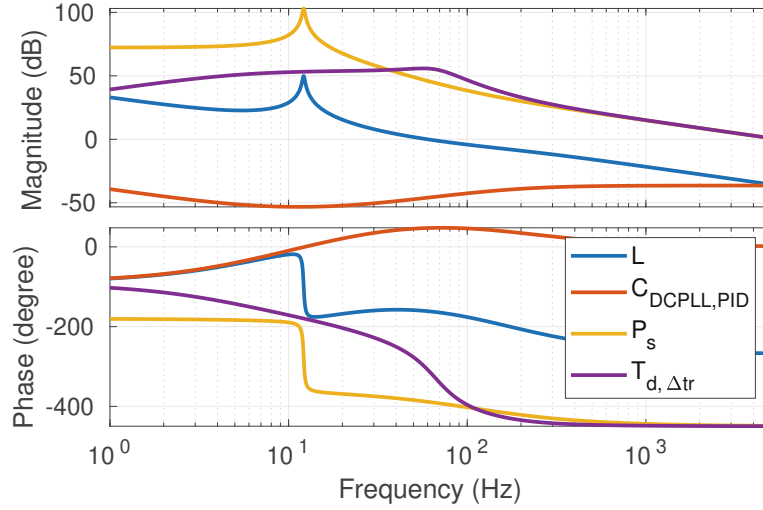


Figure 5.24: Transfer functions for the PID-based DCPLL design for the inner axis of the 2D MEMS mirror. The controller $C_{\text{DCPLL,PID}}$ controls the s_{off} input of the system P . The loop function $L = C_{\text{DCPLL,PID}}P_s$ has a crossover frequency of 20 Hz and a phase margin of 51.2° . The resulting transfer function $T_{d,\Delta tr}$ from disturbance d to Δtr is also shown.

5.7.1 PLL Design

Figure 5.23 (a) shows transfer functions relevant to the PLL design of the inner axis. The PI controller C_{PLL} stabilizes the plant P_T . The loop transfer function $L = C_{\text{PLL}}P_T$ has a crossover frequency of 20 Hz, and a phase margin of 45.5° . The crossover frequency of the PLL can be selected to 50 Hz and still has a phase margin of 44.8° , which offers better performance. However, this makes the influence of the disturbance too small to measure, therefore for the verification of the controller, the lower crossover frequency is chosen. Figure 5.23 (b) shows the closed-loop transfer function from target phase $s_{\text{off}} = s_{\text{on}}$ to Δt . Even though the measurement in clock cycles is not accurate enough to achieve a good agreement between calculation and measurement data, it is still possible to see that the implementation is successful.

5.7.2 DCPLL for Amplitude Control

The DCPLL introduced in Section 4.2 forces the MEMS mirror to run at a constant frequency. Due to the relation between frequency and amplitude shown in Figure 5.1 the DCPLL also can be used as an amplitude controller.

Furthermore, if the master axis is operated by a DCPLL, the slave axis does not need to follow the master axis. Therefore, the structure transforms into a slave-slave synchronization concept, where both axes lock to an FPGA-generated reference frequency.

Figure 5.16 shows transfer functions for the PID-based DCPLL design for the inner axis of the 2D MEMS mirror. The controller $C_{\text{DCPLL,PID}}$ controls the s_{off} input of the system P . The loop function $L = C_{\text{DCPLL,PID}}P_s$ has a crossover frequency of 20 Hz and

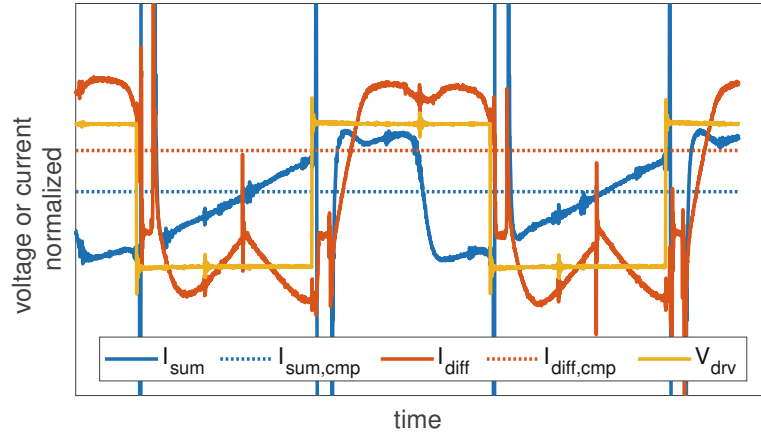


Figure 5.25: Sensing signals for the inner axis: I_{sum} is the sum signal of all sensing combs, comparing with $I_{\text{sum,cmp}}$ gives the zero-crossing pulses. I_{diff} is the difference signal between left and right sensing combs and comparing with $I_{\text{diff,cmp}}$ generates the amplitude crossing pulses. V_{drv} is the driving voltage.

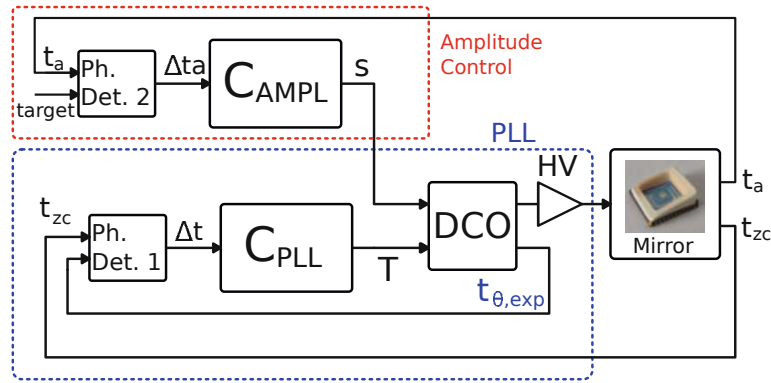


Figure 5.26: The amplitude controller loop is implemented on top of the PLL.

a phase margin of 51.2° . The resulting transfer function $T_{d,\Delta t_r}$ from disturbance to Δt is also shown.

5.7.3 Conventional Amplitude Control Design

Amplitude control can be achieved by an additional amplitude crossing signal generated by the shape of the comb drive at a certain angle [28]. This controller output regulates the s_{off} input of the scheduler. Therefore, the structure is similar to the conventional synchronization control, meaning the amplitude controller is implemented on top of the PLL-operated MEMS mirror.

Figure 5.25 shows the time-domain measurement of the sensing signals of the inner axis of the MEMS mirror. In addition to the sum current I_{sum} , generating the zero-crossing pulses, the difference current I_{diff} between the left and the right sensing comb is shown, generating the amplitude crossings by comparing to $I_{\text{diff,cmp}}$.

Figure 5.26 shows a schematic of the amplitude controller loop. The amplitude con-

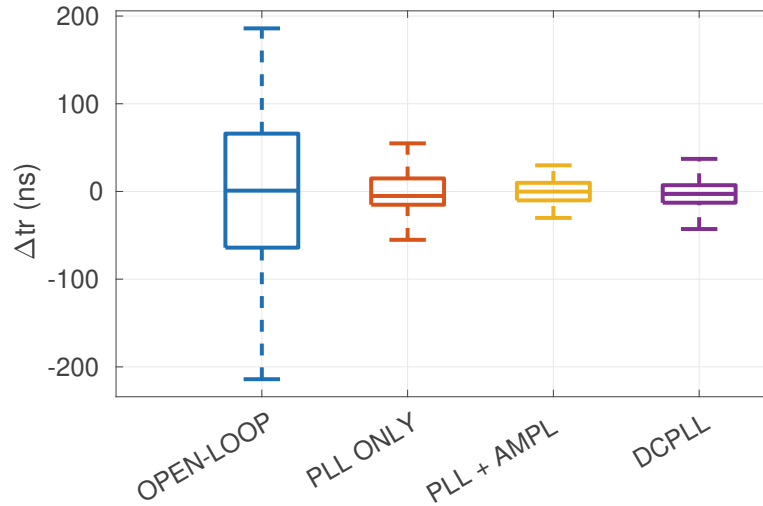


Figure 5.27: Boxplot for the amplitude control evaluation, showing a comparison of the RMS amplitude errors under vibration in the following cases: open-loop mode, PLL only, DCPLL and PLL + amplitude controller.

Table 5.2: Standard deviation of the amplitude error Δta of different controllers

	Δta (ns)
No vibration, open-loop	7.6
open-loop	84.9
PLL	27.4
Amplitude control	9.6
DCPLL	13.7

troller is implemented on top of the PLL similar to the synchronization controller in Section 5.6.1, and changes the switching-on timing s_{on} and switching-off timing s_{off} to drive the MEMS mirror to a different operating point if amplitude errors occur. The amplitude controller C_{AMPL} is hand-tuned, and consists of a high P gain and a very low I gain, to ensure convergence at the target amplitude.

5.7.4 Evaluation

To evaluate both the DCPLL as well as the amplitude controller the vibration profile shown in Figure 5.6 (b) is applied to the MEMS mirror by the piezo shaker.

Figure 5.27 displays boxplots of the amplitude error Δta under external influence. The boxplots are obtained by measuring time-domain samples of the amplitude error. It is possible to see that the PLL is not sufficient to suppress the amplitude changes due to vibrations. Table 5.2 lists the standard deviations of the amplitude error reached by the different controllers under vibration influence. The DCPLL reduces the influence of the vibration by a factor of 2.0 compared to the PLL case. However, the amplitude controller achieves better performance, even if it's only a hand-tuned PI controller. It reduces the amplitude error by a factor of 2.8 compared to the PLL case, reducing the amplitude timing error to 9.6 ns.

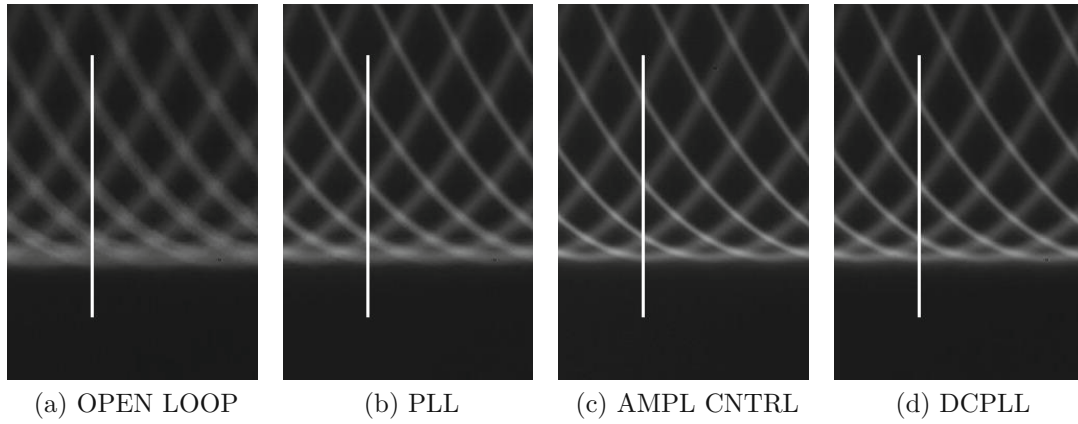


Figure 5.28: Evaluation of amplitude control by videos of the edge of the Lissajous pattern. The images show the sum of 600 single frames of a 15-seconds video for (a) open-loop mode without any controller, (b) only the PLL with $s_{\text{off}} = \text{const.}$, (c) the PI-based amplitude controller, (d) and the PID-based DCPLL. Careful observation of the images lead to the conclusion that amplitude control and DCPLL offer good amplitude stabilization.

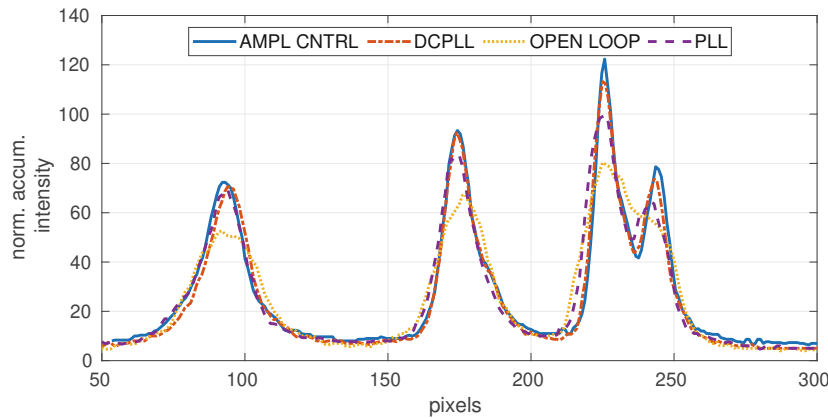


Figure 5.29: Evaluation results for the amplitude controllers under vibration influence by the intensity of the sum of all frames along the white line depicted in Figure 5.28. The DCPLL and the amplitude controller achieve good results, showing the sharpest lines.

The influence of an unstable amplitude is most visible at the edges of the Lissajous pattern. Therefore, Figure 5.28 shows the accumulated video of the bottom edge of the Lissajous frame under vibration influence in the direction of the inner axis. A careful observation leads to the conclusion that both the DCPLL and amplitude controller regulate the amplitude under external vibration, in agreement with the data presented in Figure 5.27. Figure 5.29 shows the evaluation of the amplitude controllers by the intensity of the pixels along the white line in Figure 5.28. The DCPLL and the amplitude controller achieve good results. Comparing the difference in error between the open-loop case and the amplitude controller it can be noticed that the difference in brightness increases at pixels further away from the center.

5.8 Summary

2D MEMS mirrors hold greater relevance than 1D MEMS mirrors for commercial applications because they offer possibilities to manufacture devices with a very small form factor, and minimal complexity aside from the MEMS mirror. This chapter aims to apply the knowledge gained in Chapter 4 to the 2D MEMS mirror. The 2D MEMS mirror offers additional challenges, such as coupling between the inner and outer axes and crosstalk between the axes. The FPGA implementation is adapted such that these issues could be avoided, which allows all control concepts to be applied to the 2D mirror.

The inner axis is selected as the master axis, for the outer axis to synchronize to. Vibrations in the direction of the outer axis cause a nonuniform Lissajous pattern. Therefore, closed-loop controllers are essential to enhance the Lissajous pattern. A conventional controller structure, incorporating an additional synchronization controller on top of the PLL-operated MEMS mirror, is designed and achieves a synchronization error of 160.0 ns under the influence of external vibration. The DCPLL outperforms the conventional synchronization structure also on the 2D MEMS mirror by 31 %, and the model-based LQG controller reduces the synchronization error by 46 %. This demonstrates, that the DCPLL also increases the achievable performance, in addition to its main benefit of removing the competition between the two controllers and allowing simple SISO controller design methods.

External vibrations can also influence the inner axis. As the inner axis is the master axis, running at a precise frequency is not necessary. However, the vibration affects the amplitude of the MEMS mirror, which is undesirable in projection systems. Therefore, an amplitude controller is implemented for the master axis. The amplitude controller, implemented on top of the PLL, improves the amplitude error by a factor of 2.8 compared to the MEMS mirror operated by a PLL only. Additionally, the DCPLL is designed for the master axis to investigate its ability in stabilizing the amplitude. The DCPLL improves the amplitude by a factor of 2.0 compared to the PLL, showing that the DCPLL also can be effectively used for amplitude regulation.

The proposed advanced model-based controllers and novel control concepts demonstrate highly robust operation under harsh environmental conditions, providing reliable MEMS optical scanning for automotive applications such as LIDAR and head-up displays.

CHAPTER 6

Conclusion

MEMS scanning systems represent a promising and versatile technology for industrial applications and entertainment, reaching from 3D scanning in automotive LIDAR to AR. A successful integration in daily use requires the devices to handle the harsh environmental conditions, foremost the external vibration. In this thesis, different controllers for MEMS mirrors have been developed and evaluated concerning their capability to maintain a Lissajous pattern. This chapter concludes the thesis by providing short answers to the research questions defined in Chapter 1 and proposes research questions that could be investigated in further studies.

Controlling MEMS mirrors by PLLs can be considered to be the current state of the art of driving resonant MEMS mirrors. Under the severe influence of external vibration, a PI-based PLL proves insufficient, leading to undesirable oscillations in the projected pixels. Therefore, the question that arises was:

Research Question 1 Can model-based control and systematic incorporation of the disturbance improve the closed-loop performance of the PLL for resonant MEMS mirrors?

In Chapter 3 two model-based PLL controllers are designed: a LQG-based PLL and an H_∞ -based PLL. Both of them are evaluated in an experimental setup where the MEMS mirror is mounted on a piezo-actuated shaker that applies vibrations according to an automotive standard to the MEMS mirror [54]. The PI controller achieves an RMS deviation of the pointing error of 23.1 millidegree, the LQG controller 11.8 millidegree, and the H_∞ controller 12.0 millidegree, demonstrating that model-based design techniques can improve the optical pointing uncertainty by a factor of two compared to simple PI control.

For a synchronization scenario, the relative phase between two MEMS mirrors has to be controlled. Conventionally, this is achieved by an additional synchronization controller, on top of the PLL-operated MEMS mirror [43]. This synchronization concept led to the second research question as follows:

Research Question 2 Does the synchronization concept with a synchronization controller on top of the PLL-operated MEMS mirror cause performance competition? And if so, how can this issue be avoided?

In Chapter 4.1.3 the synchronization structure is analyzed, showing a competition between the PLL and the synchronization controller. Increasing gains of the synchronization controller degrades the performance of the PLL, and vice versa. The DCPLL is proposed as a solution to the problem. The DCPLL not only solves the competition between the controllers but also provides a better performance. Additionally, the DCPLL is a single SISO controller, which significantly simplifies controller design.

The uniformity of the Lissajous pattern is impacted by strong external vibration. This led to the third research question as follows:

Research Question 3 Can model-based control methods such as LQG and H_∞ control improve the stability of the Lissajous pattern under external vibration influence?

In Chapter 4 a PID-based, LQG-based and H_∞ -based DCPLL is developed. The PID-based DCPLL improves the standard deviation of the synchronization error by 26.6 % compared conventional controller structure. The LQG-based controller and the H_∞ -based controller show an additional improvement of 19.9 % and 11 %, respectively, compared to the PID-based DCPLL.

The last research question was dedicated to a 2D MEMS mirror device, which offers additional challenges:

Research Question 4 Can the developed control concepts also be applied to a 2D MEMS mirror?

To do so, first, the 2D MEMS mirror is identified. The 2D MEMS mirror poses additional challenges, namely the mechanical coupling and the electrical crosstalk between the two axes. The coupling is identified and the resulting frequency responses show that at the selected operating point the coupling is very weak. Electrical crosstalk between the two axes makes it impossible to detect zero-crossings during the switching events of any axis. The solution to circumvent the electrical crosstalk is to discard measurements taken are taken during period where electrical crosstalk has occurred.

Having successfully confronted the challenges, the proposed controllers can also be deployed successfully on the 2D MEMS mirror. The DCPLL improves the RMS synchronization error of the outer axis of the 2D MEMS mirror by 30.9 % compared to a conventional synchronization controller on top of the PLL-operated MEMS mirror. The LQG-based controller shows an additional improvement, reducing the RMS synchronization by 46.1 %. External vibrations also influence the inner axis, showing fluctuations in the amplitude. An amplitude controller, implemented on top of the PLL, improves the amplitude error by a factor of 2.8 compared to the MEMS mirror operated by a PLL only. Additionally, the DCPLL is also able to stabilize the amplitude, by improving the amplitude error by a factor of 2.0 compared to the PLL.

This thesis demonstrates that innovative synchronization structures and model-based design approaches can effectively enhance the robustness against external vibrations. This allows the utilization of MEMS mirrors under harsh environmental conditions, enabling reliable MEMS-based optical scanning for both LIDAR applications and AR devices.

6.1 Outlook

For commercial applications, the 2D MEMS mirror is more promising than a system with two separated 1D MEMS mirrors because of the small form factor and a much simpler optical system. However, challenges like crosstalk and coupling have only been investigated very briefly in this thesis to make sure that they are not going to cause issues during the controller design. The controller performance can further be improved if the coupling effects between the inner and outer axes are considered during controller design. Model-based MIMO controllers could be investigated for the 2D MEMS mirror possibly improving the performance even further. Furthermore, model-based state estimation techniques can solve the issue of missing zero-crossing measurements, caused by the crosstalk from the switching of the other MEMS mirror axis.

When observing the transfer function of the local dynamics of the 2D mirror, it can be noticed that the resonance frequency is rather low compared to the sampling frequency. Additionally, the achieved bandwidth of the PLL is only 50 Hz, which is very low compared to the sampling frequency of the inner axis is in the range of 45 kHz. This results in very low controller gains, which leads to numerical difficulties when implemented in a fixed-point format. A proper separation between the mirror oscillation period and the controller sampling frequency could result in fewer numerical rounding errors, allowing a more resource-efficient implementation because a shorter fixed-point format can be used.

In all the proposed synchronization concepts, the frequency of the slave axis is determined by the frequency of the master axis and the Lissajous ratio. The amplitude of the slave axis is therefore determined by the frequency and cannot be modified. However, both the duty cycle of the driving signal and the driving signal influence the resulting amplitude. A MIMO controller that regulates both the amplitude and the frequency could be investigated.

Furthermore, the DCO as well as all phase error measurements are based on the synchronized time of the FPGA, which limits the resolution of the measurements and the precision of the driving signals for the laser and the MEMS mirror itself. With ever-increasing MEMS mirror frequency, these errors grow. Under vibration, the time errors are still significantly larger than a single clock period, therefore the benefit is limited. For applications without vibrations, however, the errors caused by the synchronous design gain significance. Analog designs or time-to-digital and digital-to-time converter modules provide a more accurate conversion between analog time and its digital representation and could improve the system's performance.

Finally, the applications of the MEMS mirrors are very versatile, while they have not been explored much in this thesis. A full real-time projection system requires moving

6 Conclusion

large amounts of data from a display interface to the Lissajous pattern, and its efficient implementation offers interesting challenges from a hardware design perspective. Real application of the knowledge gained through research put the developed technology to the test, and most likely open many new research questions to be solved by further research.

Bibliography

- [1] Infineon. (2021) Eine revolution bei augmented reality (ar): der neue mems-scanner von infineon für brillen und head-up-displays. [Online]. Available: <https://www.infineon.com/cms/de/about-infineon/press/press-releases/2021/INFXX202108-091.html>
- [2] Airbus. Airbus technical magazine, 56.
- [3] B. Ballard, V. Bhakta, M. Douglass, P. Gelabert, J. Kempf, W. McDonald, G. Pettitt, P. Rancuret, A. Rankin, J. Thompson, and P. I. Oden, “5-1: Invited paper: ‘steering’ light with texas instruments digital micromirror device (dmd) - past, present & future,” *SID Symposium Digest of Technical Papers*, vol. 47, no. 1, pp. 28–31, 2016. [Online]. Available: <https://sid.onlinelibrary.wiley.com/doi/abs/10.1002/sdtp.10590>
- [4] J. Zou, E.-L. Hsiang, T. Zhan, K. Yin, Z. He, and S.-T. Wu, “High dynamic range head-up displays,” *Opt. Express*, vol. 28, no. 16, pp. 24 298–24 307, Aug 2020. [Online]. Available: <https://opg.optica.org/oe/abstract.cfm?URI=oe-28-16-24298>
- [5] A. Choorakuzhiyil and N. Tiwari, “Promising candidature of oleds, mini leds micro leds in the realm of ar/vr applications,” in *2022 International Conference on Smart Generation Computing, Communication and Networking (SMART GENCON)*, 2022, pp. 1–7.
- [6] T. Raj, F. Hashim, A. Huddin, M. F. Ibrahim, and A. Hussain, “A survey on lidar scanning mechanisms,” *Electronics*, vol. 9, p. 741, 04 2020.
- [7] V.-F. Duma and M.-A. Duma, “Optomechanical analysis and design of polygon mirror-based laser scanners,” *Applied Sciences*, vol. 12, no. 11, 2022. [Online]. Available: <https://www.mdpi.com/2076-3417/12/11/5592>
- [8] A. Yaacobi, “Integrated optical phased arrays for lidar applications,” Ph.D. dissertation, Massachusetts Institute of Technology, 2015.
- [9] C.-P. Hsu, B. Li, B. Solano-Rivas, A. R. Gohil, P. H. Chan, A. D. Moore, and V. Donzella, “A review and perspective on optical phased array for automotive

Bibliography

- lidar,” *IEEE Journal of Selected Topics in Quantum Electronics*, vol. 27, no. 1, pp. 1–16, 2021.
- [10] J. Notaros, “Integrated optical phased arrays for augmented reality, lidar, and beyond,” in *2022 Optical Fiber Communications Conference and Exhibition (OFC)*, 2022, pp. 1–2.
- [11] K. Petersen, “Silicon as a mechanical material,” *Proceedings of the IEEE*, vol. 70, no. 5, pp. 420–457, 1982.
- [12] J. B. Angell, P. W. Barth, and S. C. Terry, “Silicon micromechanical devices,” *Scientific American*, vol. 248, pp. 44–55, Apr. 1983.
- [13] A. Yalcinkaya, H. Urey, D. Brown, T. Montague, and R. Sprague, “Two-axis electromagnetic microscanner for high resolution displays,” *Journal of Microelectromechanical Systems*, vol. 15, no. 4, pp. 786–794, 2006.
- [14] D. Raboud, T. Barras, F. Lo Conte, L. Fabre, L. Kilcher, F. Kechana, N. Abelé, and M. Kayal, “Mems based color-vga micro-projector system,” *Procedia Engineering*, vol. 5, pp. 260–263, 2010, eurosensor XXIV Conference. [Online]. Available: <https://www.sciencedirect.com/science/article/pii/S1877705810006442>
- [15] W. Ma, H.-Y. Chan, C. C. Wong, Y. C. Chan, C.-J. Tsai, and F. C. S. Lee, “Design optimization of mems 2d scanning mirrors with high resonant frequencies,” in *2010 IEEE 23rd International Conference on Micro Electro Mechanical Systems (MEMS)*, 2010, pp. 823–826.
- [16] I. Aoyagi, K. Hamaguchi, Y. Nonomura, and T. Akashi, “A raster-output 2d mems scanner with an 8×4 mm mirror for an automotive time-of-flight image sensor,” in *2013 Transducers Eurosensors XXVII: The 17th International Conference on Solid-State Sensors, Actuators and Microsystems (TRANSDUCERS EUROSENSORS XXVII)*, 2013, pp. 2321–2324.
- [17] S. T. S. Holmström, U. Baran, and H. Urey, “Mems laser scanners: A review,” *Journal of Microelectromechanical Systems*, vol. 23, no. 2, pp. 259–275, 2014.
- [18] H. Urey, “MEMS scanners for display and imaging applications,” in *Optomechatronic Micro/Nano Components, Devices, and Systems*, Y. Katagiri, Ed., vol. 5604, International Society for Optics and Photonics. SPIE, 2004, pp. 218 – 229. [Online]. Available: <https://doi.org/10.1117/12.580450>
- [19] D. Brunner, H. Yoo, and G. Schitter, “Digital asynchronous phase locked loop for precision control of moems scanning mirror,” vol. 52, pp. 43–48, 01 2019.
- [20] M. Tani, M. Akamatsu, Y. Yasuda, H. Fujita, and H. Toshiyoshi, “A combination of fast resonant mode and slow static deflection of soi-pzt actuators for mems image projection display,” 09 2006, pp. 25 – 26.
- [21] A. M. Elshurafa, K. Khirallah, H. H. Tawfik, A. Emira, A. K. S. Abdel Aziz, and S. M. Sedky, “Nonlinear dynamics of spring softening and hardening in folded-mems comb drive resonators,” *Journal of Microelectromechanical Systems*, vol. 20, no. 4, pp. 943–958, 2011.

- [22] H. Yu, P. Zhou, K. Wang, Y. Huang, and W. Shen, "Optimization of moems projection module performance with enhanced piezoresistive sensitivity," *Micromachines*, vol. 11, p. 651, 06 2020.
- [23] J. Grahmann, A. Dreyhaupt, C. Drabe, R. Schroedter, J. Kamenz, and T. Sandner, "Mems-mirror based trajectory resolution and precision enabled by two different piezoresistive sensor technologies," 03 2016, p. 976006.
- [24] R. Schroedter, H. W. Yoo, D. Brunner, and G. Schitter, "Charge-based capacitive self-sensing with continuous state observation for resonant electrostatic mems mirrors," *Journal of Microelectromechanical Systems*, vol. 30, no. 6, pp. 897–906, 2021.
- [25] B. Cagdaser and B. E. Boser, "Low-voltage electrostatic actuation with inherent position feedback," *Journal of Microelectromechanical Systems*, vol. 21, no. 5, pp. 1187–1196, 2012.
- [26] N. Wongkomet and B. Boser, "Correlated double sampling in capacitive position sensing circuits for micromachined applications," in *IEEE. APCCAS 1998. 1998 IEEE Asia-Pacific Conference on Circuits and Systems. Microelectronics and Integrating Systems. Proceedings (Cat. No.98EX242)*, 1998, pp. 723–726.
- [27] D. Brunner, H. W. Yoo, and G. Schitter, "Precise phase control of resonant moems mirrors by comb-drive current feedback," *Mechatronics*, vol. 71, p. 102420, 2020. [Online]. Available: <https://www.sciencedirect.com/science/article/pii/S0957415820300969>
- [28] D. Brunner, S. Albert, M. Hennecke, F. Darrer, and G. Schitter, "Self-sensing control of resonant mems scanner by comb-drive current feedback," *Mechatronics*, vol. 78, p. 102631, 2021. [Online]. Available: <https://www.sciencedirect.com/science/article/pii/S0957415821001094>
- [29] H. W. Yoo, S. Albert, and G. Schitter, "Fourier series-based analytic model of a resonant mems mirror for general voltage inputs," *Journal of Microelectromechanical Systems*, vol. 30, no. 3, pp. 343–359, 2021.
- [30] D. Brunner, H. Yoo, T. Thurner, and G. Schitter, "Data based modelling and identification of nonlinear sdof moems mirror," 03 2019, p. 43.
- [31] D. Brunner, H. W. Yoo, and G. Schitter, "Linear modeling and control of comb-actuated resonant mems mirror with nonlinear dynamics," *IEEE Transactions on Industrial Electronics*, vol. 68, no. 4, pp. 3315–3323, 2021.
- [32] H. W. Yoo, R. Riegler, D. Brunner, S. Albert, T. Thurner, and G. Schitter, "Experimental evaluation of vibration influence on a resonant mems scanning system for automotive lidars," *IEEE Transactions on Industrial Electronics*, vol. 69, no. 3, pp. 3099–3108, 2022.
- [33] G.-C. Hsieh and J. Hung, "Phase-locked loop techniques. a survey," *IEEE Transactions on Industrial Electronics*, vol. 43, no. 6, pp. 609–615, 1996.
- [34] A. Singhal, C. Madhu, and V. Kumar, "Designs of all digital phase locked loop," in *2014 Recent Advances in Engineering and Computational Sciences (RAECS)*, 2014, pp. 1–5.

Bibliography

- [35] —, “Designs of all digital phase locked loop,” 03 2014, pp. 1–5.
- [36] R. Staszewski and P. Balsara, “All-digital pll with ultra fast settling,” *Circuits and Systems II: Express Briefs, IEEE Transactions on*, vol. 54, pp. 181 – 185, 03 2007.
- [37] V. Denis, M. Jossic, A. Renault, C. giraud audine, and B. Chomette, “Identification of nonlinear modes using phase-locked-loop experimental continuation and normal form,” *Mechanical Systems and Signal Processing*, vol. 106, 02 2018.
- [38] S. Peter and R. Leine, “Excitation power quantities in phase resonance testing of nonlinear systems with phase-locked-loop excitation,” *Mechanical Systems and Signal Processing*, vol. 96, pp. 139 – 158, 04 2017.
- [39] A. C.-L. Hung, H. Y.-H. Lai, T.-W. Lin, S.-G. Fu, and M. S.-C. Lu, “An electrostatically driven 2d micro-scanning mirror with capacitive sensing for projection display,” *Sensors and Actuators A: Physical*, vol. 222, pp. 122–129, 2015. [Online]. Available: <https://www.sciencedirect.com/science/article/pii/S0924424714004427>
- [40] C. Wang, H.-H. Yu, M. Wu, and W. Fang, “Implementation of phase-locked loop control for mems scanning mirror using dsp,” *Sensors and Actuators A: Physical*, vol. 133, no. 1, pp. 243–249, 2007. [Online]. Available: <https://www.sciencedirect.com/science/article/pii/S0924424706002408>
- [41] C. Wang, H.-H. Yu, C. Tsou, and W. Fang, “Application of phase locking loop control for mems resonant devices,” in *IEEE/LEOS International Conference on Optical MEMS and Their Applications Conference, 2005.*, 2005, pp. 165–166.
- [42] W. Shahid, Z. Qiu, X. Duan, H. Li, T. D. Wang, and K. R. Oldham, “Modeling and simulation of a parametrically resonant micromirror with duty-cycled excitation,” *Journal of Microelectromechanical Systems*, vol. 23, no. 6, pp. 1440–1453, 2014.
- [43] A. Strasser, P. Stelzer, C. Steger, and N. Druml, “Towards synchronous mode of multiple independently controlled mems mirrors,” *IFAC-PapersOnLine*, vol. 52, no. 15, pp. 31–36, 2019, 8th IFAC Symposium on Mechatronic Systems MECHATRONICS 2019. [Online]. Available: <https://www.sciencedirect.com/science/article/pii/S2405896319316349>
- [44] P. Stelzer, A. Strasser, C. Steger, H. Plank, and N. Druml, “Towards synchronisation of multiple independent mems-based micro-scanning lidar systems,” in *2020 IEEE Intelligent Vehicles Symposium (IV)*, 2020, pp. 1080–1085.
- [45] P. Frigerio, R. Tarsi, L. Molinari, G. Maiocchi, A. Barbieri, and G. Langfelder, “A novel closed-loop architecture for accurate micromirror trajectory control in linear scanning mems-based projectors,” 03 2021, p. 4.
- [46] A. Nayfeh, *Introduction to Perturbation Techniques*. Wiley, 1981. [Online]. Available: <https://books.google.at/books?id=kzbvAAAAMAAJ>
- [47] J. F. Rhoads, S. W. Shaw, K. L. Turner, J. Moehlis, B. E. DeMartini, and W. Zhang, “Generalized parametric resonance in electrostatically actuated microelectromechanical oscillators,” *Journal of Sound and Vibration*, vol. 296, no. 4, pp. 797–829, 2006. [Online]. Available: <https://www.sciencedirect.com/science/article/pii/S0022460X06002355>

Bibliography

- [48] R. Schmidt, G. Schitter, and A. Rankers, *The Design of High Performance Mechatronics - 3rd Revised Edition: High-Tech Functionality by Multidisciplinary System Integration*. IOS Press, Incorporated, 2020. [Online]. Available: <https://books.google.at/books?id=VnxczQEACAAJ>
- [49] R. Stengel, *Optimal Control and Estimation*, ser. Dover books on advanced mathematics. Dover Publications, 1994. [Online]. Available: <https://books.google.at/books?id=jDjPxqm7Lw0C>
- [50] D. P. Joseph and T. J. Tou, “On linear control theory,” *Transactions of the American Institute of Electrical Engineers, Part II: Applications and Industry*, vol. 80, pp. 193–196, 1961. [Online]. Available: <https://api.semanticscholar.org/CorpusID:51655913>
- [51] K. Åström and B. Wittenmark, *Computer-Controlled Systems: Theory and Design, Third Edition*, ser. Dover Books on Electrical Engineering. Dover Publications, 2011. [Online]. Available: <https://books.google.at/books?id=9Y6D5vviqMgC>
- [52] W. Levine and R. Reichert, “An introduction to h/sub infinity / control system design,” in *29th IEEE Conference on Decision and Control*, 1990, pp. 2966–2974 vol.6.
- [53] J. O. Smith, *Introduction to Digital Filters with Audio Applications*. <http://ccrma.stanford.edu/~jos/filters/>, accessed 14.11.2023, online book.
- [54] “Lv 124: electric and electronic components in motor vehicles up to 3.5 t - general requirements, test conditions and tests (vw 80000),” in *Volkswagen AG, Tech. Rep. 8MA00*, 2013.
- [55] R. Munnig Schmidt, G. Schitter, and J. van Eijk, *High Performance Mechatronics*. Delft University Press, 2011.

Appendix A

In [31] a linear local model for the MEMS mirror running at a operating point derived by a period-to-period energy conservation approach is introduced. This section shows that the relation

$$P_s = P_T(z - 1) - 1 \quad (1)$$

can be derived from the localized model. P_s is the transfer function from s_{off} to Δt and P_T is the transfer function from T to Δt . As described in Section 3.1 there is a scaling between P_s and P_T . In the case of the implementation presented in this thesis this is 256, in case of [31] the scaling is given by $\kappa_{t/s}$, so (1) becomes

$$P_s = \kappa_{k/s} (P_T(z - 1) - 1). \quad (2)$$

In the authors disseration the model is extended to include the s_{off} input

$$\begin{aligned}
 x_{k+1} &= \overbrace{\frac{1}{\kappa_{sp} + \kappa_d} \begin{bmatrix} (\kappa_{sp} + \kappa_d)(\kappa_c + 1) - 1 & -\kappa_{sp} \\ 1 & \kappa_{sp} \end{bmatrix}}^A x_k + \overbrace{\begin{bmatrix} \kappa_{t/s}(\kappa_c - \frac{1}{\kappa_{sp} + \kappa_d}) & 1 \\ \kappa_{t/s} \frac{1}{\kappa_{sp} + \kappa_d} & 0 \end{bmatrix}}^B \begin{bmatrix} s_{\text{off},k} \\ T_k \end{bmatrix} \\
 \Delta t_k &= \underbrace{\begin{bmatrix} 1 & 0 \end{bmatrix}}_C x_k.
 \end{aligned} \quad (3)$$

Equation (2) is now be derived from (3). First of all the transfer function P_T can be derived from the state-space representation with

$$P_T = C(zI - A)^{-1}B_2 = \frac{C \text{adj}(zI - A)B_2}{\det(zI - A)}, \quad (4)$$

where B_2 is the part of B corresponding to the T input, i.e. $B = \begin{bmatrix} B_1 & B_2 \end{bmatrix}$ and $\text{adj}(\cdot)$ denotes the adjoint matrix. P_T calculates to

$$P_T = \frac{1}{\det(zI - A)} \left(z - \frac{\kappa_{sp}}{\kappa_{sp} + \kappa_d} \right). \quad (5)$$

Appendix A

The calculation of P_s involves more steps, but after some algebraic simplifications

$$P_s = \frac{\kappa_{t/s}}{\det(zI - A)} \left(z \left(\kappa_c - \frac{1}{\kappa_{sp} + \kappa_d} \right) - \frac{\kappa_{sp}\kappa_c}{\kappa_{sp} + \kappa_d} \right) \quad (6)$$

can be obtained. Substituting Equation (5) into (2) results in

$$\begin{aligned} P_s &= \kappa_{t/s} (P_T(z - 1) - 1) \\ &= \frac{\kappa_{t/s}}{\det(zI - A)} \left(\left(z - \frac{\kappa_{sp}}{\kappa_{sp} + \kappa_d} \right) (z - 1) - \det(zI - A) \right). \end{aligned} \quad (7)$$

The determinant $\det(zI - A)$ calculates to

$$\begin{aligned} \det(zI - A) &= \left(z - (\kappa_c + 1) + \frac{1}{\kappa_{sp} + \kappa_d} \right) \left(z - \frac{\kappa_{sp}}{\kappa_{sp} + \kappa_d} \right) - \left(\frac{-\kappa_{sp}}{\kappa_{sp} + \kappa_d} \frac{1}{\kappa_{sp} + \kappa_d} \right) \\ &= z^2 + z \left(-\kappa_c - 1 + \frac{1 - \kappa_{sp}}{\kappa_{sp} + \kappa_d} \right) + \frac{(\kappa_c + 1)\kappa_{sp}}{\kappa_{sp} + \kappa_d} - \frac{\kappa_{sp}}{(\kappa_{sp} + \kappa_d)^2} + \frac{\kappa_{sp}}{(\kappa_{sp} + \kappa_d)^2} \\ &= z^2 + z \left(-\kappa_c - 1 + \frac{1 - \kappa_{sp}}{\kappa_{sp} + \kappa_d} \right) + \frac{(\kappa_c + 1)\kappa_{sp}}{\kappa_{sp} + \kappa_d}. \end{aligned} \quad (8)$$

With this knowledge the calculation of (7) can be continued:

$$\begin{aligned} P_s &= \frac{\kappa_{t/s}}{\det(zI - A)} \left(\left(z - \frac{\kappa_{sp}}{\kappa_{sp} + \kappa_d} \right) (z - 1) + \det(zI - A) \right) \\ &= \frac{\kappa_{t/s}}{\det(zI - A)} \left(\left(z - \frac{\kappa_{sp}}{\kappa_{sp} + \kappa_d} \right) (z - 1) - z^2 - z \left(-\kappa_c - 1 + \frac{1 - \kappa_{sp}}{\kappa_{sp} + \kappa_d} \right) - \frac{(\kappa_c + 1)\kappa_{sp}}{\kappa_{sp} + \kappa_d} \right) \\ &= \frac{\kappa_{t/s}}{\det(zI - A)} \left(z^2 + z \left(-1 - \frac{\kappa_{sp}}{\kappa_{sp} + \kappa_d} \right) + \frac{\kappa_{sp}}{\kappa_{sp} + \kappa_d} - z^2 \right. \\ &\quad \left. - z \left(-\kappa_c - 1 + \frac{1 - \kappa_{sp}}{\kappa_{sp} + \kappa_d} \right) - \frac{(\kappa_c + 1)\kappa_{sp}}{\kappa_{sp} + \kappa_d} \right). \end{aligned} \quad (9)$$

Collecting equal terms and simplifying further yields

$$\begin{aligned} P_s &= \frac{\kappa_{t/s}}{\det(zI - A)} \left(z \left(-1 - \frac{\kappa_{sp}}{\kappa_{sp} + \kappa_d} + \kappa_c + 1 - \frac{1 - \kappa_{sp}}{\kappa_{sp} + \kappa_d} \right) + \frac{\kappa_{sp}}{\kappa_{sp} + \kappa_d} - \frac{(\kappa_c + 1)\kappa_{sp}}{\kappa_{sp} + \kappa_d} \right) \\ &= \frac{\kappa_{t/s}}{\det(zI - A)} \left(z \left(\kappa_c - \frac{1}{\kappa_{sp} + \kappa_d} \right) - \frac{\kappa_c\kappa_{sp}}{\kappa_{sp} + \kappa_d} \right). \end{aligned} \quad (10)$$

Comparing Equation (10) with Equation (6) proves that indeed P_s can be calculated with the formula given in (2).